Title
Shock Wave Acceleration of Monoenergetic Protons using a Multi-Terawatt CO_2 Laser

Author
Haberberger, Dan

Publication Date
2012

Peer reviewed|Thesis/dissertation

UNIVERSITY OF CALIFORNIA
Los Angeles

Shock Wave Acceleration of Monoenergetic Protons using a Multi-Terawatt CO_2 Laser

A dissertation submitted in partial satisfaction
of the requirements for the degree
Doctor of Philosophy in Electrical Engineering

by

Daniel Joseph Haberberger

2012

ABSTRACT OF THE DISSERTATION

Shock Wave Acceleration of Monoenergetic Protons using a Multi-Terawatt CO_2 Laser

by

Daniel Joseph Haberberger
Doctor of Philosophy in Electrical Engineering
University of California, Los Angeles, 2012
Professor Chandrashekhar Joshi, Chair

Compact and affordable ion accelerators based on laser-produced plasmas have potential applications in many fields of science and medicine. However, the requirement of producing focusable, narrow-energy-spread, energetic beams has proved to be challenging. In this thesis, an experimental demonstration of the generation of monoenergetic ions via collisionless electrostatic shock waves driven in a laser produced plasma is presented.

The physical processes behind shock wave formation, propagation, and their potential to produce monoenergetic ion beams is explored using 1D OSIRIS simulations. It is observed that a shock wave can be formed from the interpenetration of two plasmas via the expansion from a density discontinuity or an initial relative drift velocity. These processes can be instigated in the laser driven case where the laser can produce a moving sharp density spike and strong electron heating as it bores a hole through an overdense plasma. Under appropriate conditions, an electrostatic shock is formed that detaches from he laser and propagates in the plasma even after the laser is turned off. This shock can then overtake and reflect ions from the upstream plasma and accelerate them to yield a relatively narrow energy spread.

A multi-terawatt CO_2 laser system was developed at the UCLA Neptune Laboratory for exploring laser-driven shock wave acceleration of ions. The theory behind CO_2 am-

plification of picosecond pulses where the bandwidth is provided by the pressure of the CO_2 gas and the field of the laser pulse itself is developed. These ideas are applied for the production of 3 ps CO_2 laser pulses with peak powers of up to 15 TW, currently the most powerful CO_2 laser pulses ever produced.

These laser pulses were used for laser-driven shock wave acceleration of protons in a hydrogen gas jet where the peak plasma density is in the range of 3-5 n_{cr}, where n_{cr} is the critical plasma density for 10 μm radiation. Interferometry using a picosecond 532 nm laser pulse showed that the plasma has a dynamically formed profile with a sharp (10λ) rise to overcritical densities and a long exponential fall (30λ). Protons accelerated from this interaction reach energies of 22 MeV, are contained within a narrow energy spread of $\sim$1%, and have geometrical emittances as low as a mm·mrad. 2D OSIRIS simulations show that the laser-driven shock overtakes and reflects the protons in the slowly expanding hydrogen plasma resulting in a narrow energy spectrum. Scaling of this mechanism to higher laser powers through simulations predict the production of $\sim$200 MeV protons needed for radiotherapy by using current laser technology.

The dissertation of Daniel Joseph Haberberger is approved.

Oscar Stafsudd

Pietro Musumeci

Warren Mori

Chandrashekhar Joshi, Committee Chair

University of California, Los Angeles

2012

To my wife, Lusnail, without whose neverending patience, support, sacrifice, and love this would not be possible. To my parents whose lifelong support and guidance have allowed my pursuit of higher education.

Table of Contents

List of Figures

Acknowledgments

First and foremost, I would like to acknowledge the help and guidance of Sergei Tochitsky. Day in and day out he worked with me throughout my career at UCLA and helped me to develop the experimental skills I now possess. Without his pragmatic and optimistic approach, this experiment would certainly have not come to fruition. I would also like to thank Art Pak and Ken Marsh for their contributions in the areas of gas jets and interferometry (both experimental and computational). Many thanks to Chao Gong who spent countless hours in developing and performing the analysis of the CR-39 proton detection system. I would like to thank Frederico Fiuza and Luis Silva for their simulational support of the experiment and theoretical contributions to the project. Thanks also to Ben Winjum and Frank Tsung for helping me run the OSIRIS code. I would also like to thank Maria Guerrero and Deeona Columbia for their assistance with student related issues. Last, but certainly not least, I would like to thank my advisor, Professor Chan Joshi, not only for the opportunity to work in a state-of-the-art laboratory, but for continual support and feedback at all stages of my PhD be it experimental, computational, or theoretical.

Vita

2005	B.S. in Electrical Engineering, University of Texas at Austin, Austin, Texas
2007	M.S. in Electrical Engineering, Plasma Electronics, University of California Los Angeles, Los Angeles, California
2005-2012	Graduate Student Researcher at UCLA, Department of Electrical Engineering.

Publications

Collisionless shocks in laser-produced plasma generate monoenergetic high-energy proton beams,
Dan Haberberger, Sergei Tochitsky, Frederico Fiuza, Chao Gong, Ricardo Fonseca, Luis Silva, Warren Mori, Chan Joshi
Nature Physics, **8**, 95 (2012)

CO_2 Laser acceleration of forward directed MeV proton beams in a gas target at critical plasma density,
F. Tsung, S. Ya. Tochitsky, D. J. Haberberger, W. B. Mori, C. Joshi
Journal of Plasma Physics, Published Online (2012)

Fifteen Terawatt Picosecond CO_2 Laser System,
D. Haberberger, S. Tochitsky, C. Joshi
Optics Express, **18**, 17865 (2010)

Efficient Harmonic Microbunching in a 7th-Order Inverse-Free-Electron Laser Interaction,

S. Ya. Tochitsky, O. B. Williams, P. Musumeci, C. Sung, D. J. Haberberger, A. M. Cook, J. B. Rosenzweig, C. Joshi

Physical Review Special Topics - Accelerators and Beams, **12**, 050703 (2009)

Laser-driven shock acceleration of mono-energetic ion beams,

F. Fiuza, A. Stockem, E. Boella, R. A. Fonseca, L. O. Silva, D. Haberberger, S. Tochitsky, C. Gong, W. B. Mori, C. Joshi

Physical Review Letters - Submitted (2012)

CHAPTER 1

Introduction

Charged particle acceleration using the intense electric field of a relativistic laser pulse has the potential to generate relatively compact sources of high-quality energetic electron and ion beams, as well as sources of directional and often coherent radiation at exotic wavelengths unreachable by conventional laser systems. The field associated with a high-power laser pulse can directly accelerate electrons in a plasma [1, 2], can drive electron-plasma waves which accelerate electrons as in laser wakefield acceleration [3], or can produce space charge separation in plasmas that accelerate ions as in target normal sheath acceleration [4, 5] and radiation pressure acceleration [6, 7]. Coherent radiation sources based on laser-particle interactions have produced pulses in the attosecond range and with wavelengths spanning from extreme ultraviolet to the x-ray. Examples include high harmonic generation (HHG) [8], betatron x-ray emission [9], x-ray plasma lasers [10], and laser-based free electron lasers [11].

The wavelength of the drive laser pulse in the aforementioned interactions can play an important role in the acceleration processes. The movement of a charged particle in the field of a laser is characterized by an oscillation along the electric field as well as acceleration in the direction opposite to the laser intensity gradients. The maximum energy transferred from the laser to the particle is determined by the ponderomotive potential which scales as $I\lambda_o^2$, where I is the intensity of the laser pulse and λ_o is the wavelength. This relationship implies certain advantages of longer wavelength sources for some particle acceleration schemes and short wavelength radiation sources. For example, the highest energy photons produced in HHG scales with the ponderomotive potential, or

λ^2 [8]. Recently, an exciting phenomena of laser acceleration of neutral atoms has been explored where the acceleration is also proportional to the ponderomotive potential [12]. Long-wavelength, high-power sources are also of interest in the area of nonlinear optics where, for example, one can generate a supercontinuum source spanning from 3 μm to 14 μm [13].

High power, mid-infrared laser pulses are also very useful for the study of overdense laser-plasma interactions. Here a laser of wavelength λ_o is incident upon a plasma whose density, n, is greater than the critical plasma density, $n_{cr} = 1.1\text{x}10^{21}/\lambda_o^2[\mu\text{m}]\ \text{cm}^{-3}$, where the plasma acts as a mirror for wavelengths $\geq \lambda_o$. The understanding of the coupling and transport of laser energy to the plasma electrons and ions in overdense regions of the plasma is of fundamental interest in plasma physics and is of the utmost importance for inertial confinement fusion [14]. For near-infrared pulses from Ti:Sapph (0.8 μm) or neodymium-glass (Nd:Glass, 1 μm) laser systems, $n_{cr} \approx 10^{21}$ cm^{-3} necessitating EUV to x-ray wavelengths for probing the plasma dynamics. However, for infrared pulses at 10 μm, the critical plasma density is 10^{19} cm^{-3} thus making overdense laser-plasma dynamics accessible to probing at visible wavelengths. All of the above listed phenomena provide a strong motivation to develop terawatt-class lasers in the mid-infrared range.

1.1 High Power CO_2 Laser Systems

The CO_2 gas laser was first realized in 1964 by Kumar Patel [15] only a few years after the invention of the ruby laser. The CO_2 laser is a versatile technology capable of producing 150 kW of power in continuous wave mode [16] and 10's of kJ of energy in a single nanosecond laser pulse [17]. Also known for its high wall plug efficiency and excellent transverse beam mode quality, the CO_2 laser accounts for the vast majority of all industrial laser applications including cuttting, welding, engraving, etc [18]. Due to its strong absorption in water (which comprises 60% of human tissue), CO_2 lasers are also used in the medical field for skin grafting, skin resurfacing [19], and minor dental surgery [20].

Finally, its broad spectral range of tunability from 9-11 μm has made it a perfect tool for spectrocopic measurements. CO_2 lasers operating around the 9-11 μm wavelengths are the only viable option for the generation of high-power laser pulses in the mid-infrared wavelength region.

Chirped pulse amplification (CPA) [21] in large bandwidth media such as Ti-Sapph and Nd:Glass allows for the production of terawatt (TW)- petawatt (PW) powers in sub-picosecond pulses around the 1 μm wavelength [22]. As opposed to solid-state lasers, a CO_2 laser has a very high damage threshold (gas ionization $\geq 10^{12}$W/cm^2), and therefore can be used without a CPA arrangement. However, progress on the amplification of picosecond 10 μm laser pulses has been modest due to complications caused by the narrow bandwidth of the CO_2 gain medium [23–26]. One method to circumvent this limitation is to operate the laser at multi-atmospheric gas pressures which increases the bandwidth of the individual rotational lines ($\sim$3.7 GHz/atm) via particle collisions. Even at high pressures, though, incomplete overlap of the rovibrational lines results in a residual modulation of the gain spectrum. For example, lasing on a single line at a gas pressure of 2.5 atm limits the the pulsewidth to $\sim$1 nanosecond thus necessitating kilojoule levels of energy to reach TW powers [17]. Operation at higher pressures allowed for the production of TW CO_2 laser pulses with 170 J in 160 ps at UCLA in the Neptune Laboratory [25]. Paul Corkum at NRC demonstrated the application of this principle in a 10 atm laser with multi-line amplification to produce the first ever picosecond CO_2 laser pulses at the milijoule level [27]. Recently this technique has been used to reach a terawatt of power with 6 J in 6 ps in the 10 atm CO_2 laser at BNL [24]. However, high pressure imposes a limitation on the discharge stability in a large aperture module, therefore naturally limiting the total energy extracted. Due to this limitation, CO_2 laser systems have never achieved more than about a TW of peak power in a single beam.

Recently, this TW barrier has been surpassed at UCLA by the use of an alternative broadening mechanism allowing for the amplification of picosecond pulses known as field broadening [28]. Here, the resonant interaction of the strong electric field of the laser pulse with the CO_2 molecule causes an increase in the bandwidth due to the ac Stark Effect [29]. In this so-called 'coherent amplification' regime, picosecond pulses may be amplified efficiently at lower pressures allowing for the use of large-aperture lasers capable of producing a copious amount of energy.

Chapter 3 presents a description of the pressure and field broadening mechanisms, and their effect on the amplification of picosecond pulses in a CO_2 laser. The analysis of these mechanisms and their scalings led to a strategy for designing the multi-terawatt CO_2 laser system at the UCLA Neptune laboratory. Chapter 4 presents a description of this CO_2 laser system and reports on the experimental results where world record 15 TW CO_2 laser pulses have been obtained using the field broadening mechanism in the final amplifier. Future prospects of producing CO_2 lasers with a TW at high-repetition-rate or a PW in a single-shot are also presented. In this thesis, we have used the relativistic 10 μm pulses for proton acceleration in a H_2 gas jet using collisionless electrostatic shockwaves.

1.2 Laser Driven Ion Acceleration

Laser driven ion acceleration (LDIA) is a relatively old field in laser-plasma physics that has exploded over the past decade with the availability of multi-TW laser pulses. Although fast ions emitting from intense laser-plasma interactions have been observed since the late 1970's [30], the scientific community did not focus on laser accelerated ions until the early 2000's where the interaction of the first 100 TW to PW-scale laser systems with solid foils produced a copious amount of forward directed ions in the 10's of MeV/u energy range [31,32]. These experiments, performed at the Rutherford Appleton Laboratory [31] and the Lawrence Livermore National Laboratory [32], involved a 1 μm picosecond laser focused to intensites of 10^{19}-10^{20} W/cm^2 on a thin solid target producing up to 10^{13} protons and peak energies of up to $\sim$60 MeV. The high quality beam properties of these laser driven ions were studied in 2004 by T. Cowan et. al. [33] revealing kA currents, 0.004 mm·mrad transverse emittances, and 10^{-4} eV·s longitudinal emittances. The latter two values are 10^2 to 10^4 times better than that achieved in conventional RF accelerators, and at a fraction of the cost and size.

Scientists were quick to project applications of these newly created laser-driven ion beams. The first to be demonstrated was proton radiography as a diagnostic tool for probing strong electric fields in laser plasma interactions. This tool has been used to image electric fields down to the 1 μm scale length with a picosecond temporal resolution on a single shot [34]. A host of other proposed applications for LDIA beams, though not yet accomplished, include radiotherapy of cancerous tumors [35, 36], generation of short lived isotopes needed in positron emission tomography [37], high-brightness injectors for conventional accelerators [38], and as a fast ignitor in inertial confinement fusion [39]. Application driven requirements set for these laser-driven ion beams are high energies: 200-250 MeV/u [35, 36]; and narrow energy spreads: $\sim$1-5% for cancer therapy [35, 36] and $\sim$1% for an injector source to conventional accelerators [40].

Currently, the two most studied mechanisms for LDIA are target normal sheath acceleration (TNSA) [4, 5] and radiation pressure acceleration (RPA) [6, 7]. These are known to produce a copious amount of energetic ions in a very short distance [41]. In TNSA, a high-power, linearly-polarized laser pulse is incident upon the front side of a thin ($\sim\mu$m scale) solid target where electrons are efficiently heated to high energies. These heated electrons traverse through the target and set up a sheath field on the back side which accelerates ions from the rear surface [42]. Though this mechanism has been used to produce 60 MeV protons, the accelerated ions typically have a characteristic exponential spectrum. Additionally, the ions with the largest charge-to-mass ratio, protons - present in contaminants of all targets, absorb the majority of the energy in the acceleration fields unless the contaminants are removed with laser ablation [43] or resistive heating [44]. Recently two groups have had limited success in obtaining a peak in the TNSA generated spectrum with a full width at half maximum energy spread $\Delta E/E_{FWHM} \sim 20\%$ by engineering the target geometry or composition, but the ion energies were limited to a few MeV [45, 46]. Spectral selection through external focusing [47, 48] as well as RF phase rotation [49] has also been applied to generate a narrow peak from a TNSA exponential spectrum.

When the target thickness is decreased down to the laser skin depth, the RPA regime comes into play [6, 7]. Here, a circularly-polarized laser pulse is able to accelerate all the target electrons within the focal volume to modest energies (compared to a linearly polarized pulse) which then pulls all the ions forward through the space-charge force. The co-propagating electron-ion-laser structure allows for an efficient energy transfer from the laser to the electrons and then to ions producing, in simulations [50], ions in the GeV range with narrow energy spreads. Though the RPA mechanism seems promising, the data is scant with the only result reported to date yielding C^{6+} ions with an energy of ∼30 MeV and a $\Delta E/E_{FWHM} \sim 50\%$ [51]. This is mainly due to few nanometer thick targets (needed for this mechanism) being ionized by the laser prepulse and expanding before the main pulse arrives. Additionally, this mechanism is very susceptible to transverse laser plasma instabilities, such as the Rayleigh-Taylor instability [52], which break up the ultra thin target preventing acceleration of all the target ions. A thicker target RPA regime, called hole boring, has been studied recently with a circularly-polarized, 8 ps CO_2 laser pulse interacting with a gaseous target producing 1 MeV protons with a $\Delta E/E_{FWHM} \sim 10\%$ [53, 54].

Though the initial results produced in 2000 are exciting, the progress in the LDIA field over the past decade has been slow despite the ever increasing intensity and sophistication of laser systems as well as complex target geometries. The results of LDIA experiments are summarized in Fig. 1.1 showing a plot of peak proton energies obtained versus peak power of the incident laser pulses [55]. The various colors represent different laser pulsewidths in femptoseconds as indicated in the legend. All are results using the TNSA mechanism except for the two black boxes (narrow energy spread TNSA [45, 46]) and the orange box (RPA [51]). Peak proton energies are still below 100 MeV and seem to plateau for PW-scale laser systems. Furthermore, the vast majority of the results shown here have a continuous energy spread.

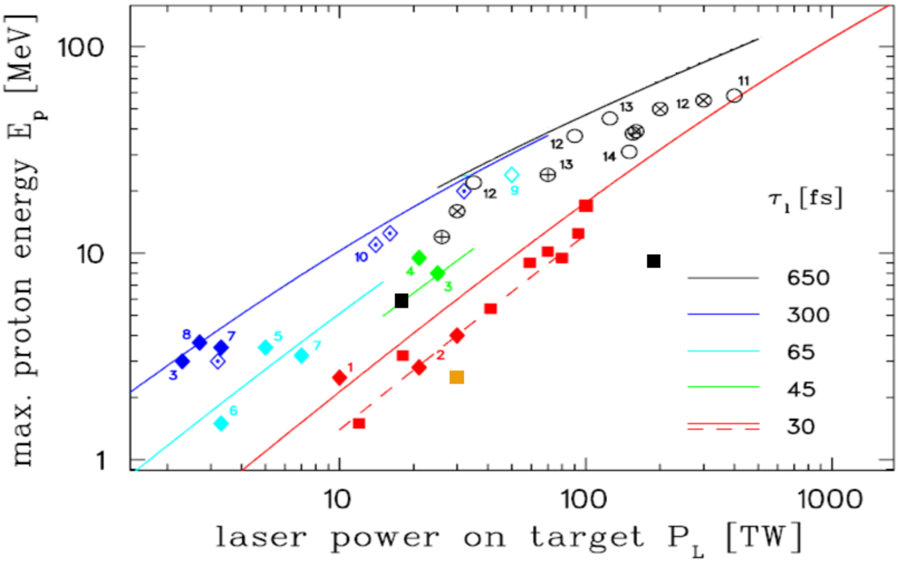

Figure 1.1: A summary of LDIA results with peak proton energy versus laser power on target [55]. The various colors represent different laser pulsewidths in femptoseconds as indicated in the legend. All are results report a continuous energy spread using the TNSA mechanism except for the two black boxes which represent narrow energy spread TNSA results [45, 46] and the orange box representing the RPA result [51]. The latter involve the acceleration of heavier ions and are plotted as E_{ion}/a.m.u.

Here we report on the discovery of a new LDIA mechanism with a promising outlook: collisionless electrostatic shocks. A shock wave can occur in a gas or plasma medium where a discontinuity in the pressure exists that travels faster than the speed of sound in the medium. Though historically associated with space plasmas involving large magnetic fields, conditions suitable for creating shock waves in the laboratory can be obtained with high intensity laser-plasma interactions [56]. Shocks have a characteristic sharp electric field in the pressure transition region that is oriented in the direction of propagation and is able to reflect, under certain conditions, ions to a maximum of twice the shock velocity [57]. For this reason astrophysical shocks that repeatedly reflect ions are proposed as the origin of high energy cosmic rays observed here on earth [58, 59].

At the UCLA Neptune Laboratory we have demonstrated shock wave acceleration

(SWA) of ions in a laser-produced plasma for the first time [60]. We show through experiment and simulations that a train of multiterawatt CO_2 laser pulses incident upon an overdense ($n_p > n_{cr}$) hydrogen gas jet can ionize the gas creating an electron-proton plasma and launch a shock wave at the point of reflection of the incident laser pulse. This shock is observed to propagate through the expanding plasma at a constant speed and reflect protons to high velocities forming a monoenergetic proton beam. Proton energies as high as 22 MeV with an energy spread of down to 1% are obtained. These results show a marked improvement in the peak energy (at a comparable laser power of 4 TW - see Fig. 1.1) and an order-of-magnitude improvement in the energy spread of proton beams obtained in both TNSA and RPA experiments.

A basic understanding of shock wave physics in relativistic plasmas relevant to the current experiment (~MeV electron temperature) is developed in Chapter 2. Here the conditions under which colliding plasmas can form a shock wave propagating at high speeds and reflect ions is investigated. The experimental setup for the proton acceleration experiment and the laser pulse diagnostics are described in Chapter 5. Chapter 6 then discusses how interferometry was used as the main plasma diagnostic to gain information on the plasma density profile during the interactions. Chapter 7 outlines the main results of the experiment, simulations elucidating the SWA mechanism, and discussion of the relevance of these results. Finally, Chapter 8 contains the conclusion.

CHAPTER 2

Simulations of Shock Wave Acceleration of Protons

2.1 Introduction

A shock wave is a disturbance that propagates through a medium faster than the velocity of a pressure wave, or sound wave. Shock waves can propagate through solid, liquid, gas, or plasma and are characterized by an abrupt change in the pressure of the medium. One of the most classic examples of a shock wave is that formed in air at the front of a jet flying at supersonic speeds. At subsonic speeds, the pressure disturbance caused by the jet's displacement of air is propagated away in the form of sound waves. At supersonic speeds, however, sound waves cannot propagate and the air particles simply pile up in density and pressure (aside from lateral transport away from the plane). The transition between the ambient air to the high pressure air in front of the plane occurs over a short distance known as the shock region. As the upstream air particles encounter the shock, they are piled up and heated through collisions with other air particles within the shock. This dissipation of energy through the shock via collisions is a key aspect differentiating a shock from another nonlinear wave called a soliton where the upstream and downstream media have the same characteristics [61]. A similar picture can be drawn for collisional shocks in a solid or a liquid.

Shock waves can also exist in a plasma where the collisional structure of the transition is complicated by the presence of electric and magnetic fields. In a plasma with a strong background magnetic field, there are multiple types of shocks based on disturbances that travel faster than the characteristic ion waves : Alfven waves for shocks propagating parallel to the magnetic field and magnetosonic waves for shocks propagating perpendicular to the magnetic field. These shocks are very prevalent in astrophysics where they are thought to be responsible for various observed phenomena including the acceleration of high energy gamma rays [58, 59]. In the purely electrostatic case, only one characteristic plasma mode exists, called the ion acoustic wave, which is analogous to the sound wave in air. In all of these cases, a shock is formed by the collision of two plasmas where a strong gradient in pressure can be created under certain conditions. The shock which forms at this pressure discontinuity then travels from the high pressure, or downstream, plasma towards the low pressure, or upstream, plasma. Due to the collective nature of the particles within a plasma, shocks can exist where collisions are not prominent, a feature unique to plasma shocks. A shock is defined as collisionless if the mean free path between particle collisions is larger than the shock width. Here, the dissipation mechanism across the shock is often acceleration of upstream ions to high energies (as in the case of the gamma ray production [58, 59]).

The ability of collisionless shocks to reflect upstream ions has been discussed in shock literature since the 1960's [57, 62–66]. Only as of recently though, has the possibility of producing these shocks by the interaction of a high power laser pulse with an overdense target been studied [67, 68]. As of yet, a full theoretical analysis of shocks predicting the reflection of ions (as opposed to ad hoc addition) has proven to be difficult ([69]), though the conditions for the onset of reflection for widely varying plasma conditions (temperatures and densities) has been recently found [70, 71]. Motivated by recent experimental results [60], these studies show theoretically the conditions under which upstream ions will be reflected from a shock and show through 2D simulations the possibility of producing monoenergetic proton beams from the interaction of an intense picosecond laser pulse with a mildly overcritical plasma.

In order to understand the basic physics behind the formation of collisionless shocks in plasmas, shocks formed from the collision of two plasmas are studied via 1D OSIRIS simulations [72]. The process by which a shock is formed is studied for the case of the expansion of a dense plasma into a rarefied one [73], as well as the case where there is an initial bulk drift between the two plasma populations. Conditions under which an ion acoustic wave forms in lieu of a shock wave are also presented. The various dissipation mechanisms of proton reflection, proton heating, and electron heating are studied in detail. Finally, a relation is made between the driven shocks in the 1D simulations and the laser driven shock case.

2.2 The Formation of Collisionless Shocks

To investigate the characteristics of a collisionless electrostatic shock such as formation, structure, and speed, a number of simulations were run using a "halfplane" geometry. Here, two semi-infinite plasmas are placed next to one another and initialized with their respective density, temperature, and bulk flow velocity. The ensuing interpenetration of these plasmas due to either expansion and/or initial bulk flow creates a propagating wave response traveling from plasma 1 (left or downstream side) towards plasma 2 (right or upstream side). The simulations have the following parameters : box size of 1500 (c/ω_p) or 8004 cells, initial border between the plasmas at 600 (c/ω_p), 256 particles per cell, and a time step of dt = 0.1874 (1/ω_p). The simulations use an electron-proton plasma representing ionized hydrogen.

The simplest case to examine is where plasma 1 is initialized with a higher density and therefore expands into plasma 2 with no initial drift velocity. In the absence of plasma 2, the process of ambipolar diffusion occurs causing expansion of plasma 1 into vacuum with the characteristic velocity C_s [74], the sound speed. This expansion is driven by an electric field set up at the plasma-vacuum interface by the electrons in the tail of the Maxwellian velocity distribution function. These electrons create a space charge separation as they leave the slower ions behind. This 'expansion field' holds back the bulk of the electrons to a sheath that extends beyond the ion density with a characteristic scale length of the Debye length, λ_{De}. The introduction of plasma 2 does two things. First, electrons in plasma 2 are able to stream into plasma 1 partially compensating for the space charge separation set up by the ambipolar diffusion of plasma 1, therefore decreasing the electric field and speed at which it propagates. Second, the remaining expansion field due to the density drop that propagates into plasma 2 can drive an IAW or shock wave depending on the speed at which it propagates. Alternatively, one can initialize the plasmas with a bulk flow velocity such that they are set to collide at t = 0 with a relative velocity, V_d. Here, a shock will form in the same manner as described above but now the expansion field is driven into plasma 2 at a higher velocity. These 'driven shocks' can be formed with equal densities in both plasmas because the plasmas will overlap due to the relative velocity forming a density step.

These concepts are displayed in Fig 2.1 which displays a snapshot of the proton density (a,c : blue lines), longitudial electric field (a,c : solid green lines), and proton longitudinal phase space (b,d) for an initial density ratio of $n_1/n_2 = \Gamma = 2$ (a,b), and similarly for $\Gamma = 40$ (c,d). The snapshots are taken at a time of 4,722 ($1/\omega_p$), where ω_p is the plasma frequency at $n/n_{cr} = 1$). There is no relative drift between the plasmas, $V_d = 0$, the protons are initialized as being almost cold (T_i = 10 eV), and the initial electron temperature is T_e = 770 keV (C_s = 0.0286c). The proton densities in Fig. 2.1a and b shown in blue lines are compared to that for expansion in vacuum ($n_2 = 0$) shown in the black lines. The red vertical line at $c/\omega_p = 600$ shows where the initial boundary between plasma 1 and 2 was at t = 0. In both cases, the characteristic rarefaction wave associated with plasma expansion into vacuum can be seen at x = 470 (c/ω_p) traveling in the negative x direction at 0.0275c ($\sim C_s$), in good agreement with theory [75]. In the case of $\Gamma = 2$ where the plasmas have similar densities, plasma 2 has impeded the expansion of plasma 1 into vacuum at a high density ($n \sim 0.75 n_{cr}$) where the expansion velocity is ~0.009c ($0.31C_s$). This can be seen from Fig. 2.1b in the range from $c/\omega_p \sim$ 500-550 where pure expansion is taking place achieving a maximum velocity of ~0.009c before a plateau is created due to the presence of plasma 2. Such a sub-sonic disturbance is seen to launch an IAW into plasma 2 traveling at an observed velocity of 0.031c ($1.08C_s$), slightly above the sound

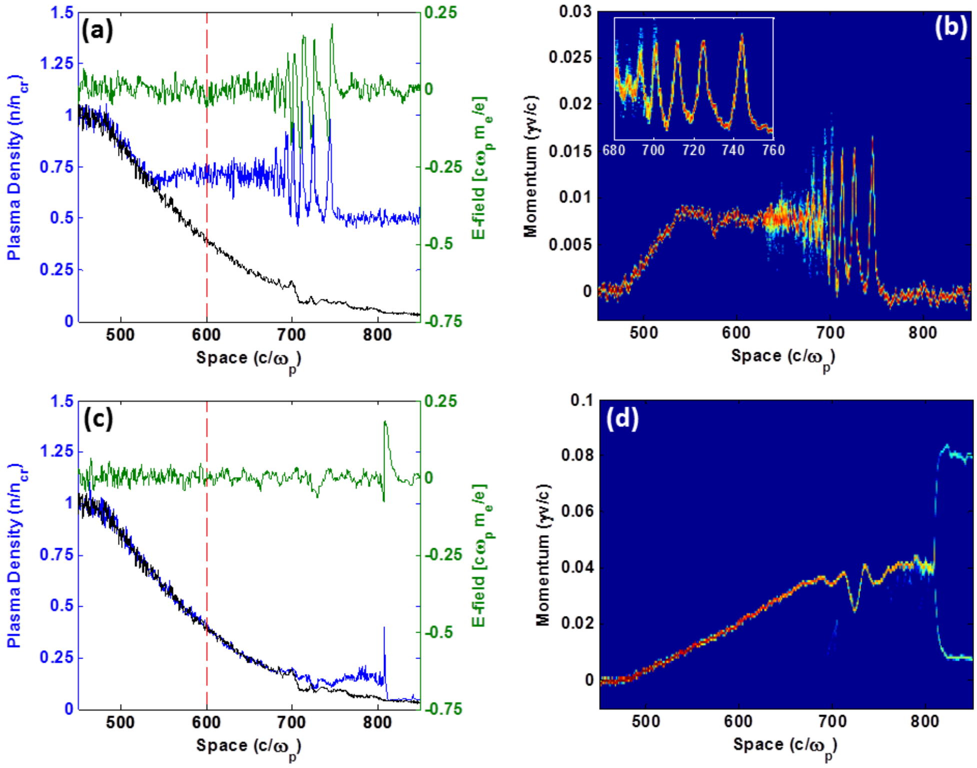

Figure 2.1: The results at a time of t = 4,722 ($1/\omega_p$) of the expansion of a dense plasma initialized at $x/\omega_p < 600$ into a less dense plasma initialized at $x/\omega_p > 600$. The density ratios are $\Gamma = 2$ (a,b) and $\Gamma = 40$ (c,d). The proton density (blue lines) and the longitudinal electric field (solid green lines) are plotted versus space for $\Gamma = 2$ (a) and $\Gamma = 40$ (c) where the dashed red line represents the initial boundary between the two plasmas. The proton density is compared to that without plasma 2 where plasma 1 simply expands into vacuum (black lines). The proton longitudinal phase space is plotted for $\Gamma = 2$ (b) and $\Gamma = 40$ (d). There is no relative drift between the plasmas, $V_d = 0$, the protons are initialized cold ($T_i = 10$ eV), and the initial electron temperature is $T_e = 770$ keV ($C_s = 0.0286c$).

speed. The IAW is characterized by a bunching of the ions seen in the density (Fig. 2.1a), an oscillatory electric field (Fig. 2.1a), and an oscillatory modulation of the momentum seen in the proton phase space (Fig. 2.1b).

In contrast, the case of $\Gamma = 40$ presented in Fig. 2.1c and d shows very different results. Here, plasma 2 impedes the expansion of plasma 1 at a density of $\sim 0.2 n_{cr}$ where the expansion velocity is far above the sound speed, $\sim 0.04c = 1.4C_s$ (see Fig. 2.1d). At this speed, a shock has been launched traveling at a supersonic speed of 0.044c ($1.54C_s$). The shock is characterized by a single spike in the proton density and electric field (Fig. 2.1c), and full reflection of the upstream protons (Fig. 2.1d). Reflection of protons from the moving potential associated with the spike in the electric field results in proton velocities of :

$$V_{refl} = 2V_{sh} - V_{up} \tag{2.1}$$

where V_{refl}, V_{sh}, and V_{up} are the velocities of the reflected protons, the shock, and the upstream protons, respectively. This equation is easily understood by comparison to a ball bouncing off a moving wall. As seen in Fig. 2.1d, for the observed $V_{sh} = 0.044c$ and $V_{up} = 0.008c$, the reflected protons travel at a velocity of $V_{refl} = 0.08c$ in full agreement with Eq. 2.1. These two examples of $\Gamma = 2$ and $\Gamma = 40$ represent two extreme cases of launching an IAW and a pure shock wave with full reflection. For the cases with Γ that lie in between 2 and 40, many interesting, yet complicated, phenomena occur such as partial proton reflection, proton heating though the shock, and proton trapping behind the shock. The resulting structure appears as a shock followed by a decaying wave structure similar to an IAW.

Many of these phenomena, and the transition between them, can be observed in the proton longitudinal phase space by varying Γ for the expansion shocks or varying V_d for the driven shocks. Fig. 2.2 displays the resulting proton phase spaces in the driven case at t = 3,972 ($1/\omega_p$) for an initial V_d equal to 0.02c (a), 0.03c (b), 0.04c (c), 0.06c (d), 0.10c (e), and 0.16c (f). For all cases, the electron temperature is T_e = 511 keV (C_s = 0.0233c). The color scale is logarithmic to highlight the trapped and reflected proton populations. Though $\Gamma = 1$ in all these cases, the overlap of the two plasmas caused by their initial relative drift velocity causes the formation of a sheath field similar to that in the expansion case. At a small V_d = 0.02c (Fig. 2.2a), an IAW has formed similar to that in Fig. 2.1b in the expansion case. As V_d increases, the potential within the wave increases and begins to trap protons as seen for V_d = 0.03c (Fig. 2.2b). Further increase of V_d to 0.04c (Fig. 2.2c) shows the onset of proton reflection from the leading edge of the wave. Also seen here is the clear separation of longer wavelength (smaller k, where k is the wavenumber) modes of the wave due to dispersion. From this point when reflection begins, increasing V_d (Fig. 2.2d,e) increases the proton reflection and the trailing waves begin to be strongly damped due to trapping which heats the transmitted protons. Finally, if V_d is increased enough, the plasmas simply pass through one another with very little interaction as shown in Fig. 2.2f for V_d = 0.16c.

To summarize, the response of a plasma due to a propagating sheath field, or potential, involves the formation of a wave-like structure. This moving potential can be the result of the expansion from an initial density discontinuity between two plasmas or from an initial relative drift velocity. For small values of Γ ($\sim$2) in the expansion case or a small initial drift velocity ($V_d \leq C_s$) in the driven case, an ion acoustic wavetrain is formed. By increasing Γ or V_d the onset of proton trapping and eventually proton reflection from the leading peak of the wave is observed. These processes will be examined in more detail in the following section.

2.3 Dissipation of Shock Energy

By definition, there must exist a pressure difference between the upstream and downstream plasmas across a shock which is characterized by a change in the density and/or temperature. As a shock propagates, the change in the state of the plasma represents a

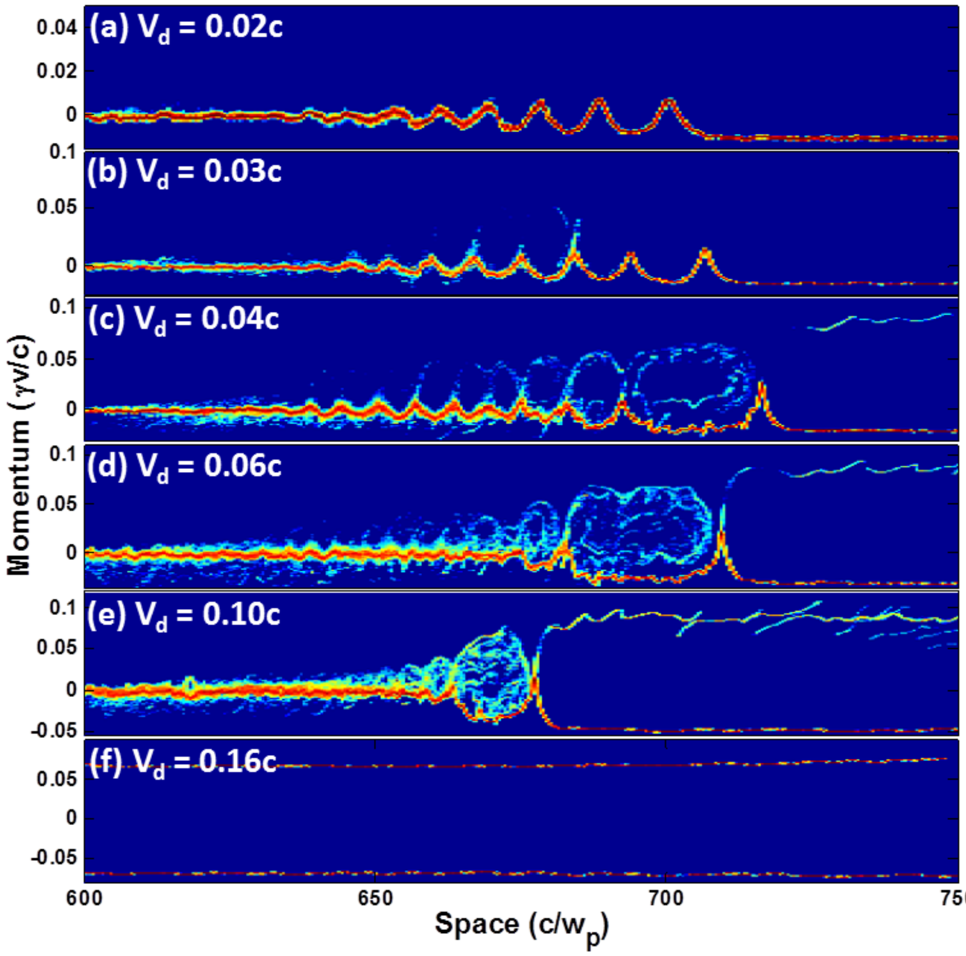

Figure 2.2: Proton longitudinal phase spaces plotted in the driven case at t = 3,972 ($1/\omega_p$) for an initial V_d equal to 0.02c (a), 0.03c (b), 0.04c (c), 0.06c (d), 0.10c (e), and 0.16c (f). The simulations are run in the center-of-mass frame, therefore plasmas 1 and 2 have an initial velocities of $V_d/2$ and -$V_d/2$, respectively. The protons are initialized cold (T_i = 10 eV) and the electron temperature is T_e = 511 keV and the initial boundary between plasmas 1 and 2 is at c/ω_p = 600.

form of energy dissipation. This can be easily accomplished by collisions within the shock, though this will be shown to be not the case in the parameter space analyzed here.

2.3.1 Particle Collisions in Hot Plasmas

The three possible binary collisions are electron-electron, electron-ion, and ion-ion. For these to play a part in the shock dynamics, the mean free path of a particle in between collisions (λ_{e-e}, λ_{e-i}, λ_{i-i}) must be on the order of or smaller than the shock thickness. For the collision calculations, we choose a plasma density $n_p = 10^{19}$ cm^{-3} which is typical for a gas jet target in laser produced plasmas. Using this density, the thickness of the shock shown in Fig. 2.1c and d can be estimated by the width of its associated electric field. This yields a shock thickness of approximately $10(c/\omega_p)$, or 16 μm for $n_p = 10^{19}$ cm^{-3}. The collision frequencies for the three binary collisions and their corresponding mean free paths can be calculated according to the following engineering formulas [76, 77] :

$$\nu_{e-e} = 5 \cdot 10^{-6} \frac{n_p ln(\Lambda)}{T_{e,eV}^{3/2}} \qquad \lambda_{e-e} = \frac{v_{th,e}}{\nu_{e-e}} \tag{2.2}$$

$$\nu_{e-i} = 2 \cdot 10^{-6} \frac{Z n_p ln(\Lambda)}{T_{e,eV}^{3/2}} \qquad \lambda_{e-i} = \frac{v_{th,e}}{\nu_{e-i}} \tag{2.3}$$

$$\nu_{i-i} = 5 \cdot 10^{-8} Z^4 \sqrt{\frac{M_p}{M_i}} \frac{n_p ln(\Lambda)}{T_{i,eV}^{3/2}} \qquad \lambda_{i-i} = \frac{v_{th,i}}{\nu_{i-i}} \tag{2.4}$$

where Z is the ionization state, M_p is the mass of a proton, M_i is the mass of the ion, and ln(Λ) is the Coulomb logarithm assumed to be 10. For collisions including electrons, their highly relativistic temperature of 1.5 MeV combined with gas jet densities of $n_p = 10^{19}$ cm^{-3} results in a λ_{e-e} and λ_{e-i} ($\propto T_e^2/n_e$ per Eq. 2.2 and 2.3) on the order of 100's of meters, therefore electron collisions play no part in the shock dynamics. On the other hand, the ions are very cold and for an initialized $T_i = 10$ eV, $\lambda_{i-i} \sim 0.2$ μm. Therefore the ions in plasma 1 and 2 are initially highly collisional within their respective populations. However, what is important in terms of the shock dynamics is if the upstream ions are collisional with the downstream ions across the shock. This is a different calculation that is based not on the temperature of the ions but on their relative bulk flow velocity. An analysis of this situation has been performed by Spitzer [78] yielding the equation $\lambda_{i-i} = 2\pi\epsilon_o^2 M_i^2 V_i^4 \ / \ n_p Z^4 e^4 ln(\Lambda)$, where ϵ_o is the permitivity of free space, V_i is the relative bulk flow velocity of the ions, and e is the charge of an electron. The strong quartic dependence on V_i results in a λ_{i-i} of 100's of meters for the shock shown in Fig. 2.1d where $V_i \sim 0.04c$. These calculations show the clear collisionless nature of the shock.

2.3.2 Proton Reflection

One of the main dissipation mechanisms of collisionless shocks is the acceleration, or reflection, of upstream ions. As the ions stream into the shock region, if their initial kinetic energy in the frame of the shock, KE = $(1/2)M_i v_i^2$, is less than the shock potential, PE = $e\phi$, then the ion will be turned around due to acceleration and leave the shock region with a velocity according to Eq. 2.1. In this manner, the shock exchanges energy with the surrounding plasma which can decrease it's potential and result in a slower shock velocity.

Fig. 2.3 displays the percent of protons reflected for expansion shocks versus Γ and for driven shocks versus V_d. As shown in the blue data points in Fig. 2.3a, the percent of protons of plasma 2 that are reflected increases from 0 at a $\Gamma = 1.3$ to 100% at a $\Gamma = 100$. However, due to the strong increase in Γ, if one normalizes the reflected particles to the density of the drive plasma (plasma 1), the peak reflection only reaches 2% indicating that the shock is not dissipating much energy. The dynamics are quite different in Fig. 2.3b for the case of driven shocks. For all these cases, $n_1 = n_2$ ($\Gamma = 1$) and $T_e = 511$ keV ($C_s = 0.0233c$). Here we can see the reflection begins to rise at $V_d = 0.04c$ and reaches a peak of ~28% at $V_d = 0.12c$, representing a strong dissipation of energy. Also plotted in blue is the shock velocity measured in the center-of-mass frame, $V_{sh,cen} = V_s h - V_d/2$, to isolate it from the driving speed, V_d. In this frame of reference, $V_{sh,cen}$ increases with V_d to a maximum of 0.033c then begins to fall. This peak correlates precisely to the point at which the reflection of protons becomes significant ($V_d = 0.05c$) indicating that the shock

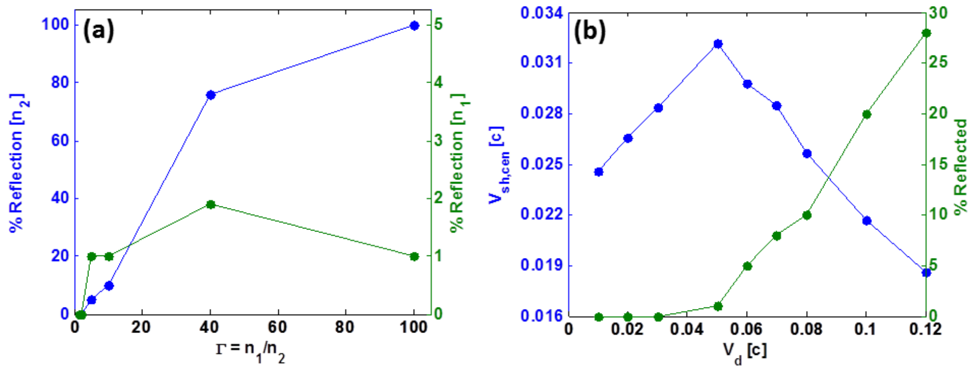

Figure 2.3: (a) The percent of reflected protons plotted versus $\Gamma = \mathrm{n}_1/\mathrm{n}_2$ for the expansion shock case ($\mathrm{V}_d = 0$). The reflection is normalized to n_1 and n_2 on blue and green axes, respectively. (b) The shock velocity in the center of mass frame, $\mathrm{V}_{sh,cen}$ (blue), and the percent of reflected protons (green) for the driven shock cases plotted versus drive velocity, V_d. The electron temperature for the expansion shock cases is $\mathrm{T}_e = 770$ keV and for the driven shock cases is $\mathrm{T}_e = 511$ keV. $\Gamma = 1$ for all the driven shock cases.

is losing energy to the accelerated protons.

A useful figure of merit for analyzing the speed of a shock (and ultimately the speed of reflected ions) for a given electron temperature, or sound speed, is the Mach number. It is defined as $\mathrm{M} = \mathrm{V}_{sh}/\mathrm{C}_s$ in the frame of the upstream plasma. As displayed in Fig. 2.4a, the Mach number for expansion shocks is seen to increase with increasing Γ up to a maximum of $\sim$1.6 for $\Gamma = 100$. Simulations with an increased Γ up to 500 show only a fractional increase in M up to 1.66 showing a clear saturation of the Mach number. Achieving higher Mach numbers is possible in the driven cases as seen in Fig. 2.4b displaying the Mach number and center-of-mass shock velocity versus V_d. Calculating the Mach number in the driven cases involves a shift to the upstream frame of reference, therefore $\mathrm{M} = (\mathrm{V}_{sh,cen} + \mathrm{V}_d/2)/\mathrm{C}_s$. It is clear from this plot the peak Mach number of 3.37 is much higher than in the expansion shock case. Due to their higher Mach numbers, driven shocks are more attractive from an ion acceleration point of view since the shock is able to reflect ions to higher energies for a given temperature of electrons.

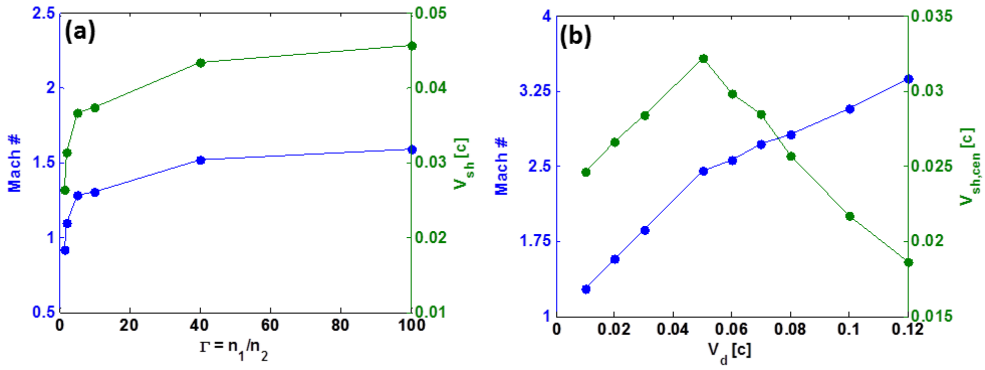

Figure 2.4: (a) The mach number and shock velocity versus Γ for the expansion shock cases (T_e = 770 keV, C_s = 0.0286c). (b) The mach number and the center-of-mass shock velocity versus V_d for the driven shock cases (T_e = 511 keV, C_s = 0.0233c).

2.3.3 Plasma Heating

A shock wave also has the capability to dissipate energy through heating of the electrons and ions of the plasma. This is possible through streaming instabilities inside the shock transition layer where there is strong mixing of the upstream and downstream plasmas. For the conditions of $v_{the} > v_{sh} > C_s$ and $T_e >> T_i$ which are clearly satisfied here, the turbulent modes created within the shock layer that ultimately transfer energy from waves to particles are related to a broad spectrum of ion waves [69]. A detailed description of these microturbulent plasma processes is quite complex and beyond the focus of the current study. However, the macroscopic result of proton and electron heating due to this turbulence as well as proton trapping in subsequent waves behind the shock is an observable in the simulations and is summarized for the driven shock case in Fig. 2.5. A zoomed in view of the proton and electron phase spaces for the case of V_d = 0.12c is shown in Fig. 2.5a and b respectively. The downstream side of the shock (~640 (c/ω_p)) in both the proton and electron phase spaces show a clear broadening of the distribution function with respect to that in the upstream. Though neither of the distributions are Maxwellian, an approximate temperature has been extracted by measuring the V_{FWHM} of the distributions and relating it to the V_{th} of a Maxwellian distribution.

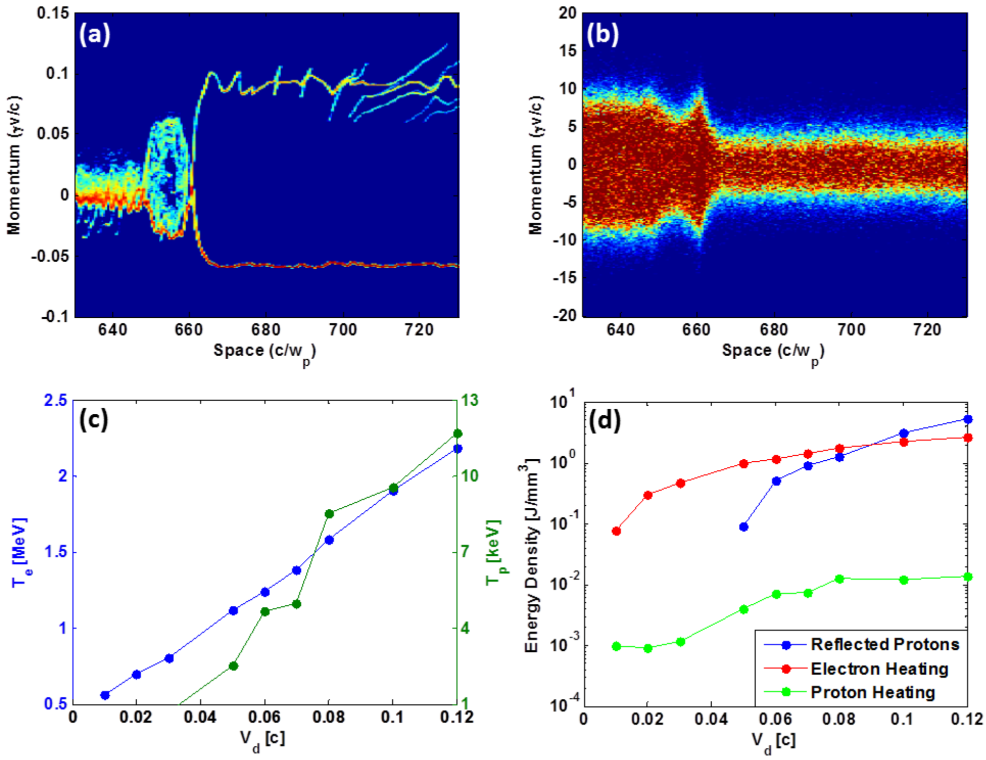

Figure 2.5: Proton (a) and electron (b) longitudinal phase spaces for $V_d = 0.12c$. Approximate downstream temperatures of the protons (green line) and electrons (blue line) versus drive velocity, V_d (c). Energy density in J/mm^3 contained in the heated protons (green line), the reflected protons (blue line), and the heated electrons (red line - compared to initial energy density) (d).

The heated proton and electron temperatures for the driven shock case (initial T_e = 511 keV, T_i = 10 eV) is plotted versus V_d in Fig. 2.5c. The heated electron temperature is seen to increase linearly from its initial 511 MeV to a peak of 2.2 MeV as V_d increases to 0.12c. On the other hand, the protons do not show any appreciable heating until V_d reaches 0.05c, the onset of reflection. This seems to be consistent with the idea that proton heating and proton reflection both have their origin in interaction with a moving potential. In the proton reflection case, the moving potential is simply the front of the shock which is fairly monotonic. For protons that traverse through the shock, they experience the accelerating fields from a broad spectrum of excited ion waves that exist in the previously mentioned turbulence.

Fig. 2.5d is a logarithmic plot of the partition of energy density dissipated through the mechanisms mentioned : proton heating (green line), electron heating (red line), and proton reflection (blue line). Since the protons are only heated to keV levels, the amount of energy they contain is on the order of mJ/mm^2 which is very small compared to the other two mechanisms. However, the energy contained in the protons that are reflected from the shock (calculated as the number of reflected particles times their mean energy) is significant and reaches $\sim$5 J/mm^3 for a V$_d$ of 0.12c corresponding to a reflection efficiency of 28% and a reflected energy of 11.6 MeV. Last, the energy increase in the electrons due to heating is also very significant having values on the J/mm^3 level. As opposed to the reflected protons which represent a true dissipation of energy from the shock, energy transferred to heat within the electrons or protons works to support the pressure difference across the shock, and therefore the potential. In this manner, the energy contained within the heated particle populations can work to support the shock structure as opposed to dissipating energy from it.

2.4 Ion Acceleration and Laser Driven Shocks

From the point of view of SWA of ions, it is of great interest to decipher what parameters affect the final velocity of protons reflected from the shock wave. According to Eq. 2.1, this depends strongly on the shock velocity. Here, the interaction considered is a high power laser pulse incident upon an overcritical plasma surface. At the critical plasma density, n$_{cr}$, the plasma frequency (ω_p), or the natural frequency of oscillation of the plasma electrons, is equal to the frequency of the incoming radiation (ω_o). For any light having a frequency $\leq \omega_o$, the plasma electrons are able to respond fast enough to the oscillating electric field of the laser to absorb and re-emit the light. Therefore the incident laser light is absorbed and reflected at this density and exerts a radiation pressure pushing the plasma backwards [79]. Therefore, the laser pulse not only heats up the plasma electrons, both at the critical surface and through the underdense plasma leading to the critical density, but also drives the surface back at the hole boring velocity. This speed at which this ion front moves can be calculated by equating the momentum flux of the protons with the pressure of the laser resulting in [42] :

$$\frac{V_{hb}}{c} = \sqrt{\frac{n_{cr}}{n_p}\frac{Zm_e}{M_i}a_o^2} \tag{2.5}$$

where n_{cr} is the critical plasma density for the incoming radiation, c is the speed of light, and a_o is the normalized vector potential of the laser. This velocity at which the plasma is moving near the front of the laser can be compared to the V_d of the halfplane simulations which has been shown to lead to the formation of a shock wave. From the halfplane simulations we know $V_{sh} = V_{sh,cen} + V_d/2$, therefore it is expected that the shock velocity will scale favorably with the a_o of the laser.

In addition to the dependence on the drive velocity, the shock velocity will depend on the specifics of the interacting plasmas such as density, temperature, and scale length. From the very simplified interactions modeled by the halfplane simulations for the driven cases, some of these dependencies have been observed. In Fig. 2.6 the velocity of the shock in the center-of-mass frame, $V_{sh,cen}$, is tracked versus V_d for three different temperatures of electrons : T_e = 511 keV (red dots), T_e = 1 MeV (blue dots), and T_e = 1.5 MeV (green dots). Also shown on the plot are the sound speeds for each electron temperature represented by the dashed line in their respective color. One can see that the cases of T_e = 1 MeV and 1.5 MeV have the same functional dependence of 511 keV as previously shown. V_{sh} is seen to increase with V_d up to a maximum which corresponds to the onset of significant (∼1-2 percent) reflection of protons and then decreases. These dynamics are closely related to the sound speed in each case. First, the drive velocity at which $V_{sh,cen}$ is a maximum, $V_{d,peak}$, roughly increases proportionally with the sound speed ($V_{d,peak}/C_s$ ∼ 2.15 for each case). Second, for the vast majority of the data, $V_{sh,cen}$ is always faster than C_s and has a maximum value in each case of approximately $1.37C_s$. These results show that the dynamics of the of shock waves are strongly dependent on the temperature

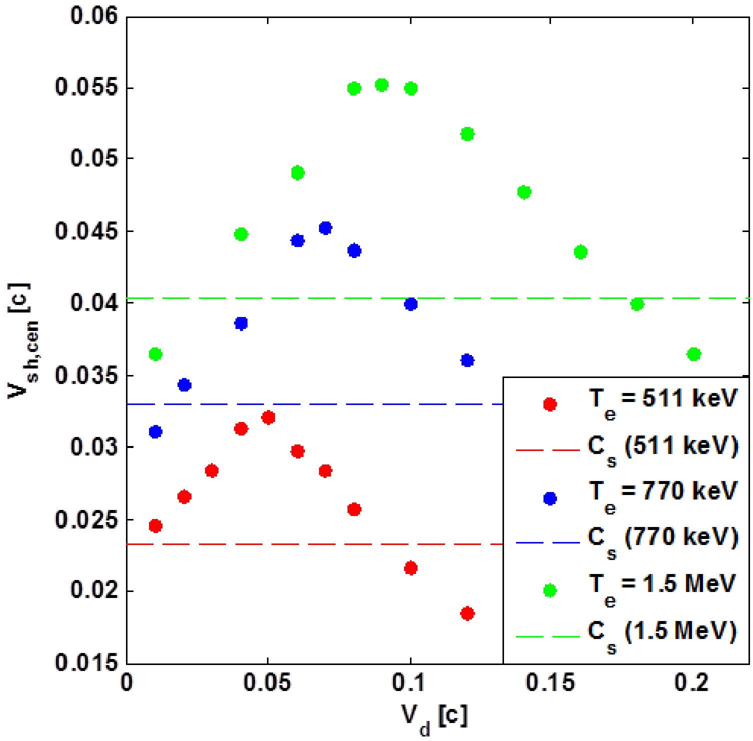

Figure 2.6: The shock velocity in the center-of-mass frame, $V_{sh,cen}$, plotted versus drive velocity, V_d, for the three electron temperatures : T_e = 511 keV (red dots), T_e = 1 MeV (blue dots), and T_e = 1.5 MeV (green dots). These values are compared to the sound speed, C_s, for each temperature which is shown by the dashed line in its respective color.

of the electrons of the plasma in which it is propagating and the velocity scales favorably with the acoustic sound speed. The temperature of the electrons in turn will depend in a complicated manner on the laser pulse duration, peak intensity, polarization, and plasma density profile. In this wide variety of conditions, the electron temperature can have a number of different dependencies on the peak a_o of the laser depending on the specific heating mechanism [42, 79, 80].

2.5 Conclusion

The basic physics of shock wave formation and propagation, and dissipation through plasma heating and ion reflection has been studied via 1D OSIRIS simulations for the interaction of two semi-infinite plasmas. For the cases of initially stationary plasmas (labeled "expansion shocks"), it is observed that the expansion of one dense plasma into a more rarefied one can cause the formation of an ion acoustic wave at smaller density ratios and a shock wave at larger density ratios. Associated with the shock wave is a spike in the proton density as well as the longitudinal electric field which is capable of reflecting up to 100% of the upstream ions, though this value never reaches above ~2% of the downstream density. If the plasmas are collided with an initial velocity, V_d (called "driven shocks"), similar dynamics are observed even with equal initial densities in the two plasmas. In this case, the velocity of the shock in the center-of-mass frame, $V_{sh,cen}$, is lower bounded by the sound speed, C_s, and is seen to increase with V_d up to the point where significant ion reflection begins. Further increase in V_d increases the amount of reflected ions thus dissipating energy from the shock and lowering $V_{sh,cen}$.

From a particle acceleration standpoint, driven shocks are advantageous in two ways as compared to expansion shocks. First, driven shocks have the capability of reflecting up to ~40% of the upstream ions as compared to ~2% in the expansion case. Second, the maximum Mach number achievable for driven shocks (3.7) is much higher than that for expansion shocks (1.9); therefore, one is able to achieve higher energy reflected ions for a given electron temperature in the plasma. For achieving these high energy reflected ions in the driven case, two parameters are highlighted which are shown to increase the speed of the shock : electron temperature and initial drift velocity.

To zeroth order, the driven shock case is compared with laser driven shocks due to the pushing on the overcritical surface by the laser pulse at the hole boring velocity. The main conclusions from this simple comparison are to optimize the laser pulse and plasma density profile to achieve efficient heating of the electrons and maximum hole boring velocity. There are many refinements of halfplane simulations that could more closely model the shock wave dynamics in the laser driven case : plasmas with finite longitudinal extent, plasmas driven with V_d and a $\Gamma \neq 1$, the study of shock propagation up and/or down a density gradient, etc. Finally, the true applicability of these ideas to the laser driven case can only be tested using 2D or 3D simulations where the interaction of the high power laser with varying plasma density profiles provides a more realistic electron distribution and plasma profile. In the ensuing chapters, an experiment is described aimed at proving the possibility of accelerating high energy protons using laser driven shocks in plasmas. First, a novel high power CO_2 laser system built at the UCLA Neptune Laboratory is presented, followed by a description of the experiment and diagnostics, and finally the results.

CHAPTER 3

Theory of CO_2 Laser Amplification of Picosecond Pulses

3.1 CO_2 Laser Amplification and Pressure Broadening

The lasing transitions in the CO_2 gain medium occur between the vibrational-rotational states of the molecule. These states are typically excited in an electrical discharge by inelastic collisions with energetic electrons. To obtain strong population inversion on the lasing transitions, the CO_2 gas is mixed with N_2 and He. Regarding the former, the first molecular vibrational excitation level of N_2 is easily excited through electron collisions, is metastable, and coincides with the upper laser level of CO_2 (00^o1); therefore, it can efficiently transfer its energy to this level through collisions. For the latter, He through its high thermal conductivity effectively cools the CO_2 gas which prevents the lower CO_2 lasing levels from becoming thermally populated since they are close to the ground state. The combination of these three gases under an electrical discharge provides a strong population inversion in the CO_2 molecule suitable for laser amplification. [81]

The vibrational levels (seen in Fig. 3.1 [82]) are described by three numbers representing the number of quanta in each mode of vibration of the molecule : $\nu_1\nu_2^l\nu_3$, where ν_1 is the symmetric stretching mode, ν_2 is the doubly degenerate (l) bending mode, and ν_3 is the asymmetric stretching mode. Each of these vibrational states consists of discrete rotational energy states (denoted by their rotational quantum number, J) which have a Boltzmann distribution of population across the vibrational branch. The peak lasing transitions in the CO_2 molecule occur between the 00^o1-10^o0 and 00^o1-02^o0 vibrational

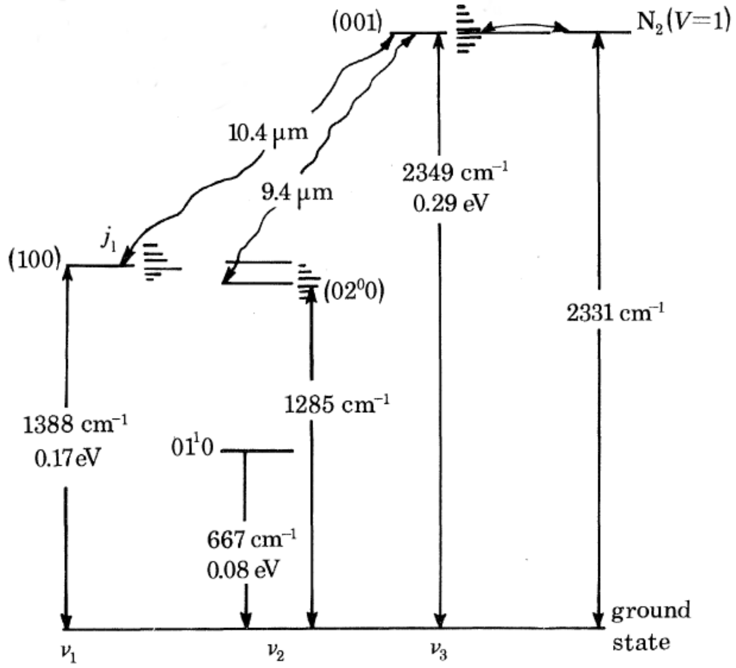

Figure 3.1: Simplified schematic of the vibrational energy levels of the CO_2 molecule (symmetric stretching mode ν_1, bending mode ν_2, and the asymmetric stretching mode ν_3) and the N_2 molecule. [82]

bands which are centered around the wavelengths of 10.4 and 9.4 μm respectively. Each band contains R-branch transitions (ΔJ = -1) and P-branch transitions (ΔJ = +1). [81]

Conventional CO_2 lasers operating on a single vibrational-rotational transition at atmospheric pressure lack sufficient bandwidth to amplify picosecond pulses. For example, on the 10P vibrational-rotational manifold centered around 10.6 μm, the gain spectrum at 1 atm of pressure consists of discrete rotational transitions separated by 55 GHz each having a bandwidth of ~3.7 GHz (gas mix of 1:1:14 CO_2:N_2:He). Therefore, the bandwidth limited pulse length that can be amplified is ~3 ns. The amplification of sub-ns pulses is made possible by the linear increase in rotational line bandwidth with the pressure of the CO_2 laser medium. The collisional bandwidth of the rotational line is related to the pressure of the gain medium according to the following equation [83]:

$$\Delta\nu_{pressure} = P \cdot (5.79\Psi_{CO_2} + 4.25\Psi_{N_2} + 3.55\Psi_{He}) \tag{3.1}$$

where $\Delta\nu_{pressure}$ is the pressure broadened rotational line bandwidth in GHz, P is the pressure of the gas mixture in atm, and Ψ_x is the fraction of x gas in the mixture. In Fig. 3.2 we show the calculated gain spectrum for the 10P branch of the 001-100 vibrational band of the CO_2 molecule. These calculations have been done for three pressures: 1, 10, and 25 atm.

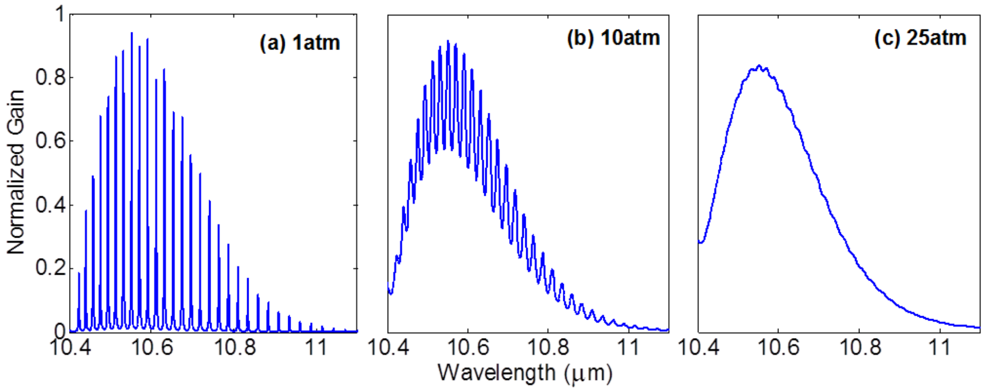

Figure 3.2: CO_2 gain spectrum vs. wavelength with a gas mixture of 1:1:14 (CO_2:N_2:He) at a pressure of 1 atm (a), 10 atm (b), and 25 atm (c).

Pressure broadening at 10 atm (Fig. 3.2b) results in a 37 GHz linewidth causing an overlap between neighboring rotational lines. Ideally, one would increase the pressure until a continuous spectrum is obtained across the entire vibrational branch spanning 1.2 THz, which happens at ∼25 atm (Fig. 3.2c). Although with such a bandwidth ∼3 ps pulses can be amplified in a straightforward manner, these pressures are not achievable in a discharge pumped system.

At realistic pressures (≤10 atm), picosecond pulses can still be amplified by seeding a pulse with a spectrum that covers multiple rotational lines. In this case, the seed spectrum (assumed to be a smooth Gaussian) is filtered through amplification by the gain spectrum which has a modulation at 55 GHz (Fig. 3.2b). The resultant temporal structure of the pulse can be found through a Fourier transform of the gain filtered pulse spectrum that results in a pulse train of picosecond pulses separated by 1/55 GHz = 18 ps. This process is similar to mode locking. In mode locking of an oscillator, many longitudinal modes locked in phase constructively interfere at a temporal separation of 1/(free spectral range), thus producing a pulse train output. Similarly in a CO_2 amplifier, the equidistant rotational lines are locked in phase by stimulation from the seed pulse and therefore their radiation will interfere to form a pulse train with a temporal separation equal to 1/(line separation). Hereafter, the resulting pulse train is referred to as a 'macropulse' and an individual pulse within the pulse train a 'micropulse'.

The relationships between the spectral and temporal properties of the resultant macropulse are illustrated in Fig. 3.3 which shows the interaction between the spectra of a 3 ps pulse and a 5 atm CO_2 medium with a gas mix of 1:1:14 (CO_2:N_2:He). Fig 3.3a shows the CO_2 gain spectrum (red), the 3 ps input pulse spectrum (green), and the pulse spectrum filtered by the CO_2 gain spectrum obtained via multiplication of the red and green traces (blue). The Fourier transform of the latter produces the expected temporal structure of the pulse after spectral filtering from the gain medium, shown in Fig. 3.3b. Three conclusions can be made by analyzing the data in Fig. 3.3. First, a macropulse is produced and has an expected micropulse separation of 18 ps. Second, the micropulse duration of 3 ps is preserved because the minimum micropulse pulsewidth is limited by the bandwidth of the whole 10P vibrational branch (1.2 THz). Third, the width of the macropulse envelope (54 ps) is estimated by the inverse of the spectral width of the individual line (18.5 GHz). Note that similar macropulses of 3 ps CO_2 laser pulses were observed in autocorrelation measurements performed by P. Corkum [27].

Although macropulses with 3 ps micropulses can be produced and amplified in a pressure broadened CO_2 medium, there are two drawbacks in terms of high-power production. First, energy extraction in a high-pressure CO_2 laser is limited because of the restriction on the gas discharge aperture size. Second, even at the highest pressures achievable, the gain spectrum still exhibits an undesirably strong modulation at 55 GHz that results in the distribution of the extracted energy over a 50-100 ps macropulse instead of a single 3

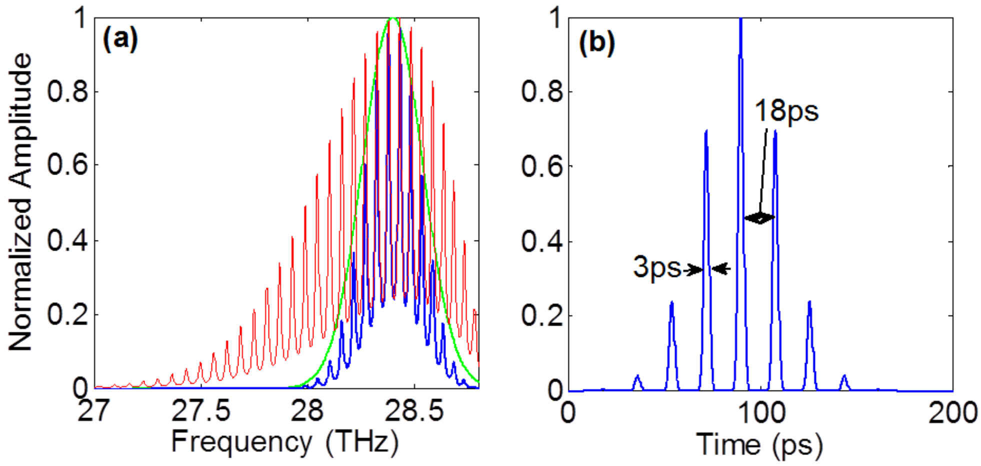

Figure 3.3: (a) CO_2 gain spectrum at 1 atm (red), 3 ps input pulse spectrum (green), and the pulse spectrum filtered by the CO_2 gain spectrum obtained via multiplication of the red and green traces (blue). (b) Fourier transform of the pulse spectrum filtered by the CO_2 gain medium.

ps pulse.

3.2 Field Broadening and Pulse Train Evolution

In addition to pressure broadening, the electric field of the laser pulse itself will broaden the bandwidth of the rotational lines due to the ac Stark Effect [29], a process commonly known as 'field broadening'. The amount of spectral broadening is only limited by the intensity of the laser pulse and the ionization threshold of the gas ($\sim 10^{13}$ W/cm^2, which is at least 3 orders of magnitude larger than the breakdown threshold of dielectrics), therefore it could potentially produce a continuous bandwidth across the entire vibrational branch.

The effect of field broadening on the rotational line bandwidth can be estimated by the following equation [84]:

$$\Delta\nu_{rot} = \Delta\nu_{pressure} + \Delta\nu_{field}$$

$$= \Delta\nu_{pressure} + 2 \cdot \Omega$$

$$= \Delta\nu_{pressure} + 2 \cdot (6.91 \cdot 10^6 \mu \sqrt{I}) \quad (3.2)$$

where $\Delta\nu_{rot}$ is the total bandwidth of the rotational line, $\Delta\nu_{pressure}$ and $\Delta\nu_{field}$ are the contributions from pressure (Eq. 3.1) and field broadening respectively, Ω is the Rabi frequency in Hz, μ is the dipole moment in Debye, and I is the laser pulse intensity in W/cm^2. For the 10.6 μm lasing transition, the dipole moment is equal to 0.0371 Debye [85]. Calculations using Eq. 3.2 show that at an intensity of 5 GW/cm^2 for a 1 atm amplifier, the resultant bandwidth of 37 GHz is comparable to that of a 10 atm amplifier (see Fig. 3.2b). Therefore, for the amplification of a sufficiently intense 10 μm pulse, field broadening can compensate for the lack of bandwidth in low pressure amplifiers.

The production of a macropulse in the early stages of amplification is inevitable because of the residual 55 GHz modulation in the gain spectrum at practical operating pressures. Therefore, it is important to study the effect of field broadening on the amplification of a macropulse where the bandwidth is continually increasing due to increasing intensity as the pulse is amplified. For this purpose, we have used a simulation code written by V. Platonenko [86] to model the amplification of a macropulse in the presence of field broadening. The results of the simulation are presented in Fig. 3.4 which displays the intensity distribution of the macropulse at various stages of the amplification defined by the g_oL product, where g_o is the small signal gain of the amplifier and L is the length.

In this simulation, a 3 atm gain medium is used to amplify a 3 ps pulse with an input intensity of 100 MW/cm^2. At this level of intensity, lack of field broadening in a low-pressure amplifier leads to the production of a macropulse as seen in Fig. 3.4a. However, as the intensity increases from 6-125 GW/cm^2 (Fig 3.4a-c), a significant shortening of the macropulse is observed. As the field broadened bandwidth increases, the extracted energy is distributed over a proportionally decreasing number of micropulses. Further amplification to 900 GW/cm^2 (Fig 3.4d - note the change in the scale of the x-axis) results

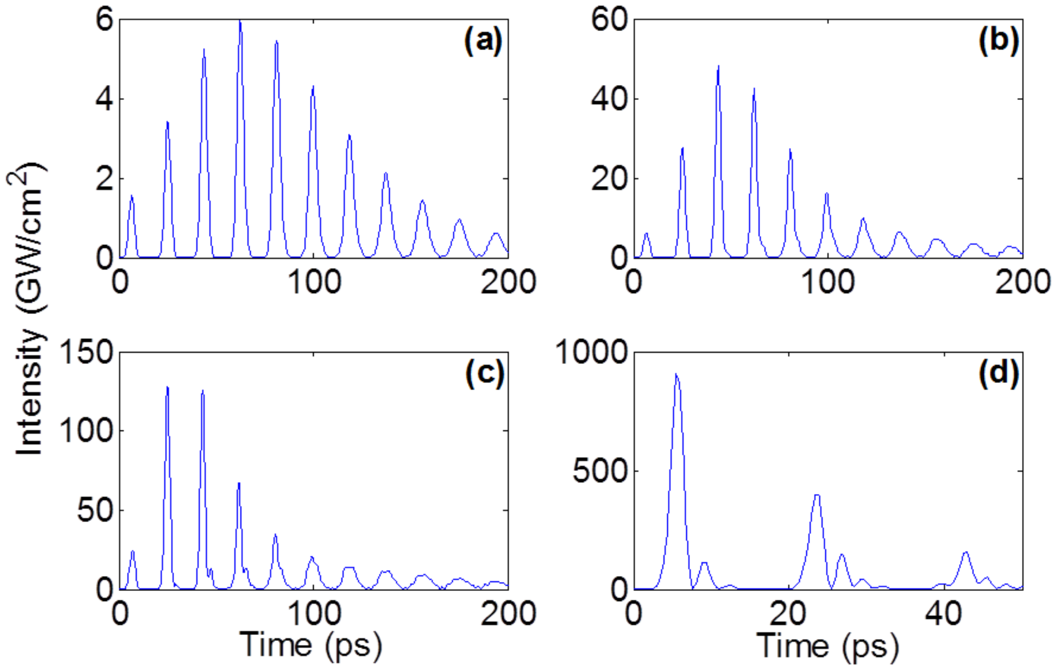

Figure 3.4: Macropulse evolution shown through consecutive plots of intensity vs. time as the pulses travel through a CO_2 amplifier at a pressure of 3 atm with a small signal gain of g_o = 3 %/cm. (a), (b), (c), and (d) are taken at g_oL products of 6.4, 9.6, 12.8, and 25.6 respectively.

in ~60% of the extracted energy in the first pulse. Ultimately, at even higher intensities amplification in a relatively low-pressure CO_2 amplifier will evolve a macropulse into a single pulse.

In addition to the macropulse evolution to a single picosecond pulse, at intensities near 1 TW/cm^2 and above, Rabi Flopping of the lasing transition begins to occur. Here, the molecular transition's response to such a large signal involves an oscillation of the population between the upper lasing state (amplification) and the lower lasing state (absorption). This oscillation occurs at the Rabi frequency (Eq. 3.2) [87] and results in the modulation and shortening of the 3 ps micropulse as seen in Fig. 3.4d. These shorter pulses then necessarily have a broader bandwidth and can ultimately (at a pulsewidth of 1 ps) access the full 1.2 THz bandwidth of the 10P branch which significantly increases the energy extraction (see discussion of saturation energy in Chapter 4). The evolution of the macropulse to a single picosecond pulse due to field broadening, combined with the shortening of the pulse along with enhanced energy extraction due to Rabi Flopping, paves the way towards the production of ultra-high power 10 μm pulse generation in CO_2 amplification. Certainly though one must analyze the potential of the gas medium and amplifier windows to withstand such high laser intensities.

3.3 Limitations and Future Prospects of Picosecond CO_2 Lasers

The principle limitations to the peak power achievable in CO_2 amplification are ionization of the gain medium and/or damage to NaCl windows housing the gas caused by the very high intensities reached in the final amplifier. As previously discussed, amplification at intensities above 10^{12} W/cm^2 can lead to the production of a single picosecond 10 μm pulse, however if the gas mix begins to ionize it will lead to multiple detrimental effects. First, ionization of the CO_2 molecule will clearly disrupt the CO_2 lasing transitions and cease amplification. Second, if the plasma density reaches values comparable to the critical plasma density for 10 μm radiation (i.e. 40% ionization of 1 atm gas mix is 10^{19} cm^{-3}), part of the laser pulse will undergo strong defocusing, absorption, and even reflection.

The first ionization process to occur as the laser intensity increases is avalanche breakdown. Here the laser field accelerates free electrons which collide with and potentially ionize other neutral molecules producing additional free electrons. This multiplication process leads to an exponential growth in plasma density starting from the partially ionized laser mix in the electrical discharge estimated at 10^{12}-10^{13} cm^{-3} [27]. The avalanche multiplication, or plasma growth rate, increases with the pressure of the laser mix due to the increased collisional cross-section. However, even at a pressure of 10 atm the maximum plasma growth rate is estimated to be $\sim$1/(300 fs) [27]; therefore, the initial plasma density is not expected to increase more than an order of magnitude for a 3 picosecond pulse (3 ps * 1/(300 fs) = 10), therefore the peak plasma density inside the amplifier will be far from 10^{19} cm^{-3}, or n_{cr} for 10μm light. This effect is even weaker at realistic pressures (1-3 atm) for a final amplifier, therefore avalanche breakdown is not a limiting factor for high power CO_2 amplification. Eventually though, the field of the laser pulse will directly ionize the gas particles. Of the gasses in the laser mix, CO_2 has the smallest ionization potential of 13.8 eV [88] corresponding to an 10.6 μm radiation intensity of $\sim$1.5x10^{14} W/cm^2, which represents a fundamental limitation on the achievable intensities in a CO_2 amplifier.

In addition to the ionization of the gas medium, the production of high power 10 μm pulses necessarily involves the NaCl windows withstanding high fluences. Corkum et. al. [27] reported on a single-shot damage threshold of NaCl for picosecond CO_2 pulses to be 500 mJ/cm^2. In the UCLA Neptune Laboratory, fluences of $\sim$1 J/cm^2 are routinely reached on the output NaCl window of the final amplifier with picosecond pulses where only multishot damage has been observed over 100's of shots. Therefore, in the speculation of high power production in a single shot laser system, 1 J/cm^2 is an acceptable fluence for any NaCl window in the final amplifier.

Under these restrictions, one can evaluate the potential of CO_2 amplifiers to produce a petawatt of laser power. Ultimately, the 1.2 THz bandwidth of the 10P vibrational branch can support the amplification of a 1 ps pulse, though intensities near 5x10^{12} W/cm^2 are needed (per Eq. 3.2) to achieve this shortening through Rabi Flopping. Producing a petawatt then involves the extraction of 1 kJ of energy. At this high level of energy, keeping safe fluences on the NaCl windows necessitates a 35 cm diameter beam which limits the intensity to 10^{12} W/cm^2. Achieving the intensity in the gain medium to satisfy Rabi Flopping while keeping the output widows safe must then involve a beam expansion by a factor of $\sim$2. It should be noted that the CO_2 amplifier used in the UCLA Neptune Laboratory, which was built at the Los Alamos National Laboratory, has been used to extract 1.1 kJ in a 35 x 35 cm aperture [17]. Therefore, a petawatt of laser power at the 10 μm wavelength is achievable using existing CO_2 amplifiers, however at a very low pulse repetition rate of one shot per 5 minutes.

Picosecond pulse amplification in CO_2 lasers can be also promising for applications where a high-repetition rate source is needed. Current CO_2 laser technology allows for the generation of 1-100J of energy at 1 - 1000Hz repetition rate in atmospheric pressure modules, though in nanosecond long pulses with low peak power. However, implementation of field broadening in a final TEA amplifier can result in rather short macropulses which provide peak powers in the GW to TW range. An example of the effect of field broadening in an atmospheric amplifier is shown in Fig. 3.5 which displays simulation results [89] of the amplification of a macropulse in a 1 atm amplifier through a $g_oL \sim 7$ and laser mix of 1:1:8 (CO_2:N_2:He). Fig. 3.5a displays the seed macropulse which has an envelope of 70 ps. Fig. 3.5b shows the result of amplifying this macropulse with an input intensity of 10 MW/cm^2 which results in a gross broadening of the macropulse envelope due to the lack of bandwidth (3.7 GHz) in an atmospheric amplifier. However, when the input intensity is increased to 10 GW/cm^2, the field broadening bandwidth per Eq. 3.2 is $\sim$50 GHz which is sufficient to sustain the 70 ps macropulse envelope as shown in the amplified macropulse in Fig. 3.5c. Therefore, field broadening allows for short picosecond macropulses to be amplified at repetition rates up to 1 kHz in atmospheric amplifiers producing high peak powers. The production of MW pulses in the 3-14 m range via supercontinuum generation [13], high harmonic generation in gasses [90], and development of a CO_2 laser driven ion source in a gas jet [60] are just a few of many potential applications for a compact picosecond CO_2 laser system run at high repetition rates.

3.4 Conclusions

Here we have shown through simulations that the amplification of 10 μm picosecond pulses is possible in CO_2 amplifiers. This amplification results in the production of a pulse train, or macropulse, of 3 ps pulses separated by 18 ps, a time characteristic to the separation between the CO_2 molecule rotational lines. The formation and temporal dynamics of such

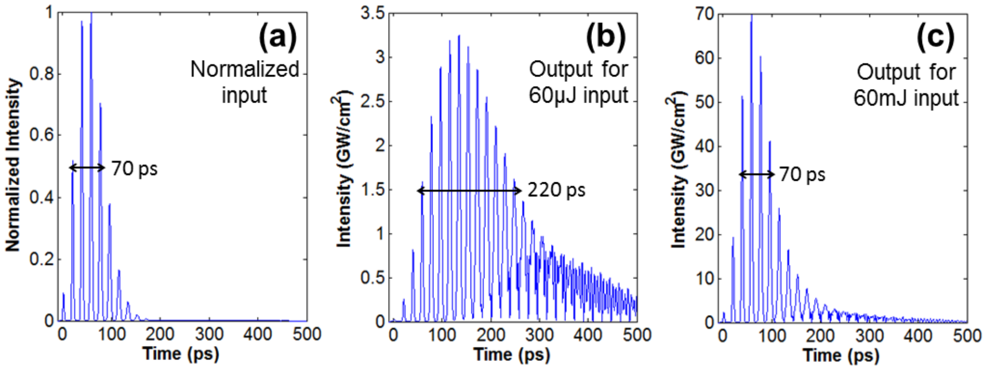

Figure 3.5: Simulation results of atmospheric amplification of 10 μm macropulses. (a) Seed macropulse into a 1 atm amplifier with a laser mix of 1:1:8 (CO_2:N_2:He) and g_oL ~7, (b) the amplified output from the seed pulse in (a) containing ~60 μJ with a peak intensity of 10 MW/cm^2, and (c) the amplified output from the seed pulse in (a) containing ~60 mJ with a peak intensity of 10 GW/cm^2. The distortion seen in (b) on the tail of the macropulse is an artifact of the simulation code.

a macropulse are fundamental properties of picosecond pulse amplification in a CO_2 active medium having a residual gain modulation. Spectral gain broadening from the pressure of the gas mixture and the electric field of the laser pulse itself have been shown to be useful methods of concentrating the extracted laser energy into a shorter macropulse, or even single picosecond pulse. When amplifying at high intensities, field broadening of the gain medium has been shown to evolve the macropulse into ultimately a single pulse. In this coherent amplification regime, field broadening compensates for the lack of pressure broadening allowing for single pulse production in low pressure (<3 atm) amplifiers.

At intensities reaching TW/cm^2, Rabi Flopping of the lasing transition begins to occur which effectively shortens the pulsewidth and increases the energy extraction from the amplifier. These effects have been shown to potentially lead to the production of a petawatt 10 μm pulse with 1 kJ of energy in 1 ps while still accounting for ionization of the gas mixture and damage of the NaCl windows on the amplifier. Both the beam size of 35 cm and the 1 kJ of extracted energy are realizable with current CO_2 amplifiers built at the Los Alamos National Laboratory and in use today at the UCLA Neptune Laboratory. Additionally, for the myriad applications seeking a high repetition rate source of GW-TW levels of 10 μm light, field broadening can be applied in atmospheric amplifiers capable of up to kilohertz repetition rates and 10's of joules level energy extraction.

Based upon the ideas presented in this chapter, the generation of high-power 10 μm pulses in a CO_2 laser chain must involve the use of both pressure and field broadening mechanisms in two stages of amplification. The first stage amplifies a nJ level seed pulse to the mJ level in a pressure broadened regime. This results in a macropulse whose envelope is restricted by the pressure broadened bandwidth of the individual rotational line. In the second stage of amplification, the mJ level macropulse is amplified to the Joule level in relatively low-pressure, large-aperture amplifiers where the field broadening mechanism assists in the evolution of the macropulse into a single pulse. This strategy is the basis behind the multi-terawatt CO_2 laser chain in the Neptune Laboratory.

CHAPTER 4

The Neptune CO_2 Laser System

The CO_2 laser system at the UCLA Neptune Laboratory is capable of amplifying picosecond 10 μm pulses up to an unprecedented peak power of 15 TW. The CO_2 master oscillator - power amplifier (MOPA) laser system is shown schematically in Fig. 4.1. It consists of three main stages :

1. The first stage produces a 3 ps, nJ-level seed pulse from a Hybrid TEA master oscillator
2. In the second stage, a regenerative amplifier boosts the energy of the seed pulse to the mJ level in a high pressure (8 atm) module
3. The third stage involves final amplification producing $\sim$100 J in a large aperture (20 x 35 cm^2) 2.5 atm module

4.1 Picosecond 10 μm Seed Production

To compensate for the lack in bandwidth of the CO_2 molecule that is needed for the generation of a picosecond pulse, a 10 μm picosecond time-scale seed pulse is often gated utilizing a short laser pulse produced by solid-state laser systems. Here a picosecond 1 μm pulse produced from an Nd:Glass CPA laser system is used. There are various methods by which a picosecond 10 μm seed pulse can be generated using a short 1 μm pulse, the most common of which is semiconductor switching [91]. An alternative method makes use of the ability of the short intense 1 μm pulse to gate the 10 μm radiation using the

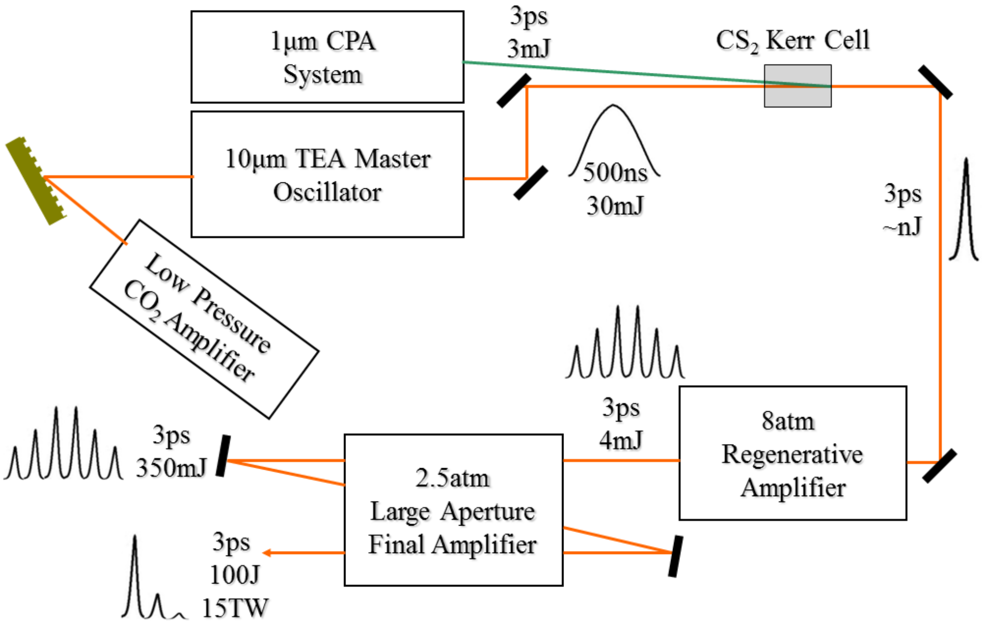

Figure 4.1: The Neptune CO_2 master-oscillator power-amplifier laser chain.

Kerr effect [92]. One advantage of the using the Kerr effect is its proportionality to the intensity of the 1 μm pulse as opposed to the fluence in semiconductor switching. For picosecond pulses, this results in a less stringent requirement on the energy needed from the 1 μm pulse. Additionally, gating a picosecond 10 μm pulse is accomplished in a single stage as opposed to two semiconductor switches needed to accomplish the same task [91].

In mediums that exhibit the optical Kerr effect, the index of refraction is dependent on the intensity of an optical pump pulse (here the 1 μm pulse) according to the following [93]:

$$n(I) = n_o + n_2 I \tag{4.1}$$

where n_o is the linear index of refraction, n_2 represents the strength of the Kerr effect in the medium, and I is the intensity of the 1 μm pump pulse in W/cm^2. This change of the refractive index along the polarization axis of the 1 μm pulse induces a birefringence in the medium which can be used as a transient phase retarder for a weaker 10 μm probe pulse. To obtain full 90° rotation of the 10 μm polarization, the following equation must be satisfied [93]:

$$|n(I) - n_o| = \frac{\lambda}{2d} \tag{4.2}$$

where $n(I)$ is the index of refraction according to Eq. 4.1, $\lambda = 10$ μm, and d is the length of the Kerr medium.

The Kerr medium chosen is carbon disulfide, CS_2, due to its transparency at 10 μm and 1 μm as well as its large nonlinear refractive index of $n_2 = 2 \times 10^{-14}$ cm^2/W [94]. Group velocity dispersion in CS_2 between the wavelengths of the pump pulse (1 μm) and the probe pulse (10 μm) is 1 ps/cm, therefore the length of our Kerr cell is limited to 2.5 cm to avoid significant broadening of the 10 μm seed pulse. For the above stated parameters, 90° rotation is provided with an intensity of 10 GW/cm^2, a practical value for picosecond pulses.

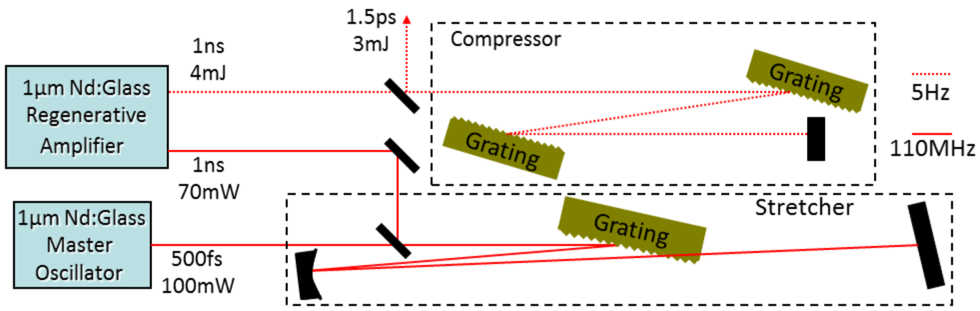

Figure 4.2: Nd:Glass 1 μm CPA laser system built to gate a picosecond 10 μm seed pulse.

An Nd:Glass 1 μm CPA system (schematic shown in Fig. 4.2) was built for controlling the CS_2 Kerr switch. The GLX-200 glass oscillator, which normally produces 200 fs pulses at 1058 nm, was altered to shift the central wavelength to 1061 nm to match the peak gain of the regenerative amplifier. At 1061 nm, the oscillator produces 500 fs pulses which are stretched to ~1 ns in a single grating stretcher. The pulses are then amplified in a glass regenerative amplifier and two single-pass booster amplifiers to ~4 mJ. Finally the pulses are sent to a double grating compressor with a 75% throughput leaving 3 mJ.

To characterize the output of the Nd:Glass laser system, a multishot non-collinear autocorrelator was built using the second harmonic generation in a 500 μm thick BBO

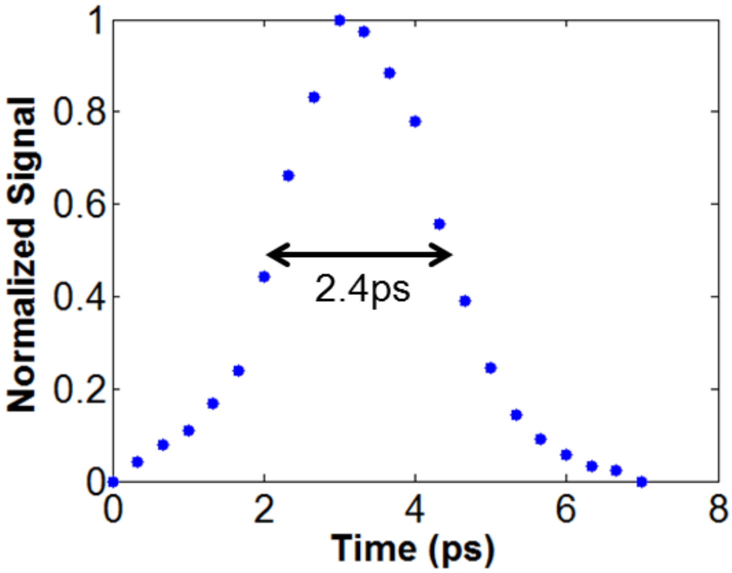

Figure 4.3: Autocorrelation measurement of the compressed 1 μm pulses from the Nd:Glass CPA laser system. The measurement was performed with a multishot non–collinear autocorrelator using the second harmonic generation from a 500 μm thick BBO crystal.

crystal to measure the pulsewidth of the compressed 1 μm pulses. Fig. 4.3 displays the autocorrelation measurement where one can extract a quasi-Gaussian pulsewidth of $\Delta\tau_{FWHM} = \frac{\Delta\tau_{AUTO}}{\sqrt{2}} = 1.7$ ps. This pulsewidth was typically on the order of 3 ps. Approximately 1 mJ of the energy is split off from the main beam and focused into the CS_2 Kerr cell with a spot size $w_o = 1$ mm (radial distance at which the intensity drops to $1/e^2$ of its peak value). This produces an intensity of 10 GW/cm^2 which provides the maximum polarization rotation for the 10 μm probe pulse. The rest of the 1 μm is sent to a Ge semiconductor switch.

The 10 μm probe pulse is produced by a hybrid TEA CO_2 oscillator. Single longitudinal mode output is obtained by placing a low pressure (30 Torr) amplifier in the cavity along with the TEA module. The output of the hybrid oscillator is 30 mJ in a 500 ns pulse. This pulse is copropagated with the 1 μm pulse at a small angle ($\sim$2°) through the Kerr cell. The polarization of a 3 ps portion of the 10 μm pulse is rotated from s-to p-polarization and transmitted through a 6-plate Ge analyzer (II-VI Inc., model:PAG-15-AC-6) that provides a measured contrast of 5x10^5. This measurement was carried out using the 500 ns long 10 μm pulse by comparing the throughput of the Ge analyzer with and without a $\lambda/2$ waveplate placed in front of the Kerr cell. After the analyzer, the CO_2 laser beam is sent to the 1 μm controlled Ge semiconductor switch to increase the contrast. Here, the 1 μm pulse forms a plasma on the surface of the Ge plate inducing reflection for 10 μm radiation a few picoseconds before the arrival of the seed pulse. The aspect ratio of the overlapped beams on the Ge plate provided a Gaussian profile for the reflected 10 μm pulse. Although this system only produces a nJ level 10 μm seed pulse, it is sufficient to injection mode lock the high-pressure regenerative amplifier.

4.2 Regenerative Amplification

The 3 ps seed pulse is sent into an 8 atm TE CO_2 laser for regenerative amplification. The laser has a gain volume of 1x1x60 cm^3 and is filled with a gas mix of 1:1:14 (CO_2:N_2:He). The amplifier is injection mode locked by seeding through a 50% ZnSe output coupler [25]. It therefore produces a pulse train with a separation equal to the 12 ns cavity roundtrip time. The total gain of $\sim 10^7$ brings the nJ level seed pulse to $\sim$10 mJ. The injection mode locked pulse train is decoupled from the seed pulse vector via transmission through the Ge semiconductor switch after the decay of the surface plasma. The pulse with maximum energy (10 mJ) is then switched out using an external CdTe Pockels cell placed between crossed polarizers. Due to the elipticity in the polarization of the input 10 μm beam, the limiting aperture of the crystal housing, and an insufficient voltage applied across the CdTe crystal, the throughput of this single pulse selector is $\sim$40% leaving 4 mJ to seed into the final amplifier.

The temporal structure of the regeneratively amplified CO_2 pulses is measured with a streak camera diagnostic described in detail in Appendix A. One such measurement using the Hammamatsu (C5689) streak camera of the regeneratively amplified pulses is displayed in Fig. 4.4 where the production of a macropulse with an 18 ps micropulse separation is evident.

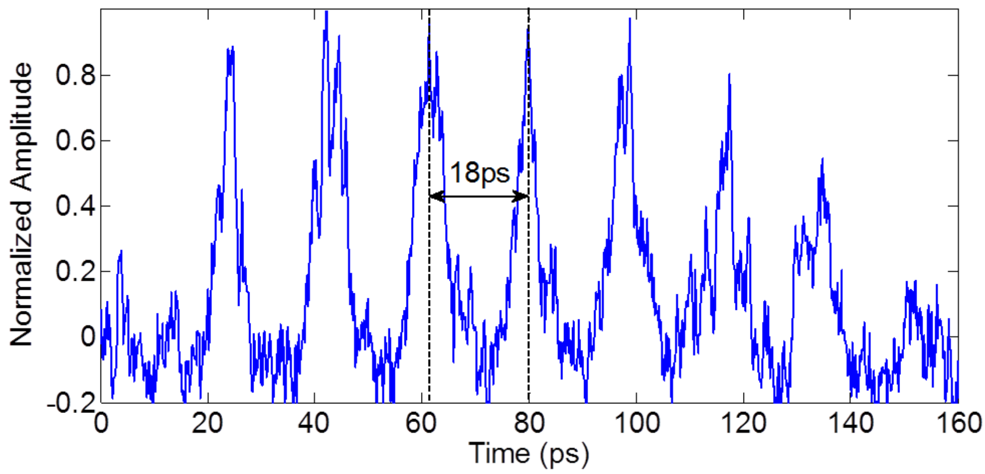

Figure 4.4: Temporal profile of the CO_2 macropulse after amplification in the regenerative amplifier as measured by the streak camera diagnostic with the Hammamatsu (C5689) streak camera.

The expected individual pulsewidths of 3 ps is near the resolution limit of the Hammamatsu (C5689) streak camera, therefore their measurement must take into account the instrumental function of the streak camera. The streak camera's instrumental function, or resolution, was experimentally determined to be 3 ps via measurement of sub-picosecond 532 nm laser pulses (see Appendix A). In the streak camera measurements of the CO_2 amplified pulse, the actual pulse width is obtained by deconvolution using:

$$\tau_p^2 = \tau_m^2 - \tau_{ins}^2 \tag{4.3}$$

where τ_p^2 is the actual pulsewidth, τ_m^2 is the pulsewidth as measured by the streak camera, and τ_{ins}^2 is the temporal resolution of the streak camera. The application of Eq. A.1 to the measurement of the individual pulsewidths seen in Fig. 4.4 leads to an average temporal FWHM of 3.3 ps. This measurement confirms that the vibrational branch bandwidth supports the amplification of ~3 ps 10 μm pulses.

The regenerative amplification produces a macropulse due to the residual 55 GHz modulation in the gain spectrum at 8 atm. The length of the pulse train envelope at the output of the laser is governed by the pulse broadening equation [87]:

$$\tau_p^2(z) = \tau_p^2(0) + (16\ln 2)\frac{\ln(G_o)}{\Delta\omega^2} \tag{4.4}$$

where $\tau_p^2(0)$ and $\tau_p^2(z)$ are the initial and final FWHM of the macropulse envelopes, G_o is the total gain, and $\Delta\omega$ is the gain bandwidth in radians. In predicting the effect of macropulse broadening on the width of the pulse train envelope, the restricting bandwidth is that of the rotational line. At 8 atm $\Delta\omega/2\pi = 37$ GHz, and for $\tau_p^2(0) = 3$ ps and $G_o = 10^7$, the expected gain narrowed macropulse envelope (FWHM) is $\sim$60 ps, which is in relative agreement with the $\sim$100 ps FWHM pulse train envelope seen in the streak camera measurements (Fig. 4.4).

4.3 Final Amplification

The final amplification occurs in a large aperture (20 x 35 cm^2) amplifier employing an electron-beam controlled discharge [17]. Three passes through the amplifier totaling 7.5 m provide a gain of $G_o \sim 25{,}000$ that produces 100 J from the 4 mJ seed. It is operated at 2.5 atm with a gas mix of 4:1 (CO_2:N_2) resulting in a collisional line bandwidth of 14 GHz. In the absence of further line broadening, this bandwidth would result in the broadening of the macropulse envelope distributing the extracted energy into many more pulses. However measurements of the amplified pulse train temporal profile recorded by the streak camera diagnostic show a significant shortening of the injected pulse train down to as low as 2 main pulses (Fig. 4.5b). The evolution from the seeded pulse train shown in Fig. 4.4 to the amplified pulse train in Fig. 4.5b is attributed to the significant increase in the CO_2 linewidth induced by field broadening and is in qualitative agreement with our simulation results displayed in Fig. 3.4. Note, due to an elevated jitter in the Hammamatsu streak camera, the single shot nature of the final amplifier necessitated the use of a Hadland Photonics (Imacon 500) streak camera with a temporal resolution of 5 ps.

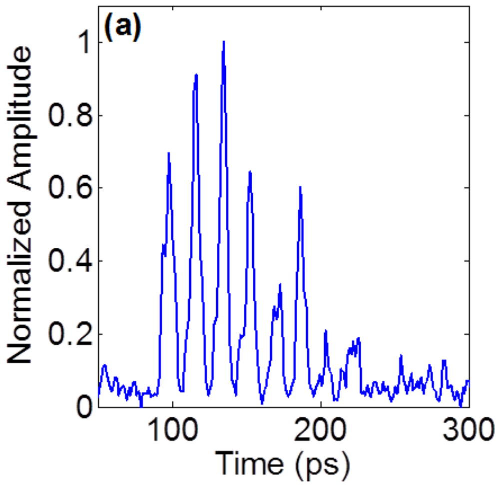

Figure 4.5: Temporal profiles of the CO_2 laser pulses after amplification in the first pass of the final amplifier (a), and all three passes of the final amplifier (b) as measured by the streak camera diagnostic with the Hadland Photonics (Imacon 500) streak camera.

The input beam for the first pass of amplification is quasi-collimated with a radius of $w_o = 4$ mm which provides an input intensity of only ~200 MW/cm^2. With a measured total gain of ~100, the intensity reaches 20 GW/cm^2 at the exit of the first pass. As evidenced by a streak camera measurement of the output shown in Fig. 4.5, the bandwidth from pressure and field broadening is sufficient to sustain the macropulse envelope pulsewidth from the regenerative amplifier.

In the second and third passes of amplification, the beam is expanded from a $w_o = 1$ cm to $w_o = 6.25$ cm to extract a large amount of energy and avoid laser damage to the NaCl window located at the output of the final amplifier. The total gain of these passes is $G_o \sim 285$ producing 100 J from the input 350 mJ. Using the energy partition extracted from the streak camera lineouts (Fig. 4.5a and 4.5b), this corresponds to an increase in peak intensity from 4 GW/cm^2 to 140 GW/cm^2. At these intensities field broadening can augment the 14 GHz bandwidth of the 2.5 atm amplifier to values up to ~200 GHz.

With such a bandwidth, one would expect the gain spectrum to be continuous across the entire vibrational branch. Thus, field broadening makes it possible to amplify high-power picosecond pulses in a 2.5 atm amplifier. A conservative estimation from Fig. 4.5b of the energy partition gives ~45 J (45%) in the peak 3 ps pulse, which equates to 15 TW of power.

4.4 Energy Extraction in Picosecond Pulse Amplification

Efficient energy extraction is an important aspect of the production of high-power pulses. In CO_2 lasers, the energy of the gain medium is stored in a manifold of vibrational-rotational levels with a Boltzmann distribution across the vibrational branch. For pulsewidths $\tau_p > 18$ ps, the spectrum of the pulse only directly interacts with a single rotational line. In this case, the saturation energy is related to the ratio of τ_p and τ_r, the rotation relaxation constant (~100 ps-atm). For $\tau_p >> \tau_r$, such as for nanosecond long pulses, the CO_2 molecule relaxation sustains a Boltzmann equilibrium between rotational lines which allows the laser pulse to extract energy from the entire vibrational branch. As τ_p is shortened and approaches τ_r, as realized in the pressure broadened case, the "rotational bottleneck effect" prevents repopulating of the rotational laser levels [95]. This causes the saturation energy to decrease and asymptotically approach that of a single line extraction, or $1/15^{th}$ of the energy stored in the vibrational band. However, further decrease in the τ_p to less than 18 ps results in the direct interaction between the pulse and multiple rotational lines separated by 55 GHz. In this case, energy is simultaneously extracted from the lines contained within the input pulse bandwidth causing an increase in saturation energy. Ultimately, for a 1 ps input pulse the stored energy from the entire vibrational branch can be extracted resulting in a theoretically calculated saturation energy of 300 mJ/cm^2 [96].

As described in the previous section, amplification of a broadband macropulse in the first pass of the final amplifier is made with a quasi-collimated small beam. In the

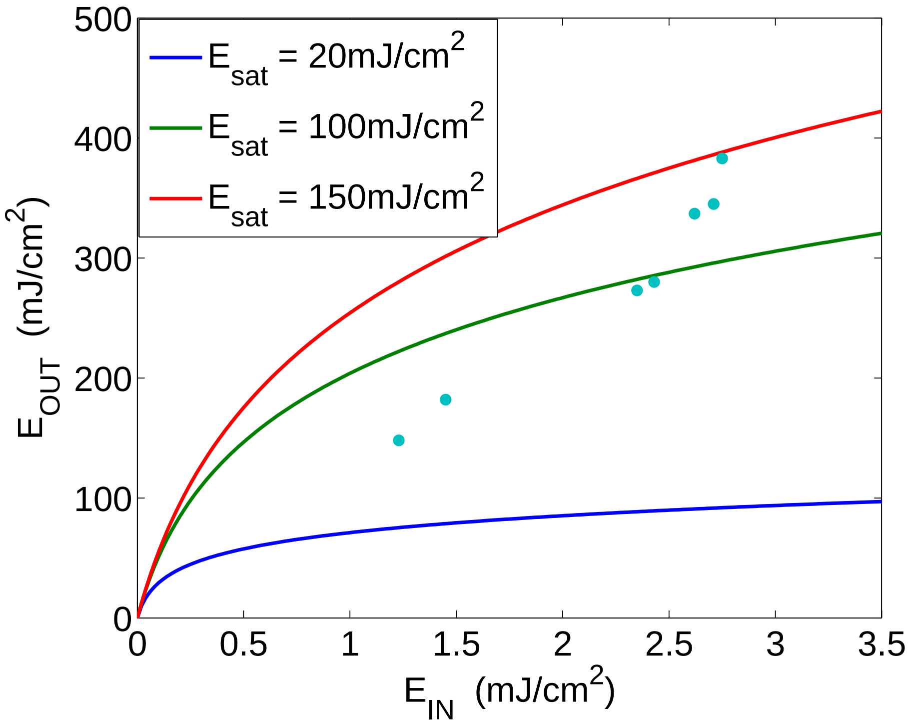

Figure 4.6: Output energy vs. input energy from the first pass of the final amplifier (data points), compared to theoretical predictions of the Frantz Nodvik equation for a saturation energy of 20 mJ/cm^2 (blue), 100 mJ/cm^2 (green), and 150 mJ/cm^2 (red).

experiment we observed strong deviation from exponential growth by a factor of five as a result of strong saturation. This enabled the extraction of the saturation energy value by measuring the output pulse energies from the first pass of amplification while varying the amplitude of the input pulse. The results are plotted in Fig. 4.6 and compared to the Frantz-Nodvik equation [97]:

$$E_{OUT} = E_{SAT} \left\{ \ln \left[1 + e^{\alpha_o l} \left(e^{E_{IN}/E_{SAT}} - 1 \right) \right] \right\} \tag{4.5}$$

where E_{IN}, E_{OUT}, and E_{SAT} are the input, output, and saturation energies respectively, α_o is the small signal gain, and l is the gain length. For these calculations, a measured small signal gain of $\alpha_o = 2.6$ %/cm and gain length of $l = 2.5$ m are used while the saturation energy is used as a fitting parameter. From these results, we can extract a saturation energy of approximately 120 mJ/cm^2. In previous measurements using 100 ps pulses in the first pass of this amplifier resulted in a saturation energy of <20 mJ/cm^2 [25]. This comparison shows a clear indication that the dynamics of the energy extraction has changed drastically between the amplification of 100 ps smooth pulses and 100 ps macropulses containing 3 ps micropulses. As opposed to the 100 ps pulse that only directly interacts with a single rotational line, the 333 GHz bandwidth of the 3 ps micropulse covers six rotational lines. Note that for a 100 ps long macropulse used for the measurement, the rotational relaxation constant of 43 ps in the amplifier introduces only a small error in the saturation energy value. It is important to stress that this extracted value is in good agreement with the theoretical value for 3 ps pulses [96].

4.5 Conclusion

We describe here a CO_2 master oscillator-power amplifier laser chain in which a 3 ps, 10 μm seed pulse is amplified to a peak power of 15 TW. The total extracted energy reaches 100 J and it is distributed over several 3 ps pulses separated by 18 ps, a time characteristic to the separation between the CO_2 molecule rotational lines. We show experimentally that significant shortening of the pulse train envelope results from amplification at high laser intensities of 10^{10}-10^{11} W/cm^2. This shortening is attributed to an increase in the CO_2 molecule bandwidth due to the field broadening mechanism. This coherent amplification is realized in a 2.5 atm large-aperture CO_2 module, thus opening possibilities to extract 100's of Joules of energy in picosecond pulses by using a low-pressure gas medium.

An additional artifact of CO_2 laser amplification of picosecond pulses is an increase in energy extraction. This fact is shown by a six times increase in the measured saturation fluence of 20 mJ/cm^2 for 100 ps pulses to 120 mJ/cm^2 for 3 ps pulses. Energy extraction in the picosecond regime is very efficient because for a broadband pulse, energy is simultaneously extracted from multiple lasing transitions.

Further amplification of the obtained pulses in more passes of the final amplifier in the intensity range of 10^{11}-10^{12} W/cm^2 can induce Rabi flopping of the lasing transition as seen in the simulations presented in the previous chapter. This would lead to a significant shortening of the pulse from 3 ps down to $\sim$1 ps, which is accompanied with an increase in the saturation energy to 300 mJ/cm^2. Realization of such a scheme would allow for the generation of 100 TW and higher powers at 10 μm in a single pulse, parameters unimaginable without coherent amplification.

CHAPTER 5

LDIA Experimental Setup and Methods

5.1 Target Chamber

The interaction of the focused multi-terawatt CO_2 laser beam with the gas jet occurs in a vacuum target chamber pumped down to a pressure of $< 10^{-4}$ Torr. This pressure corresponds to a residual air density of 3.2x10^{12} cm^{-3}, which is orders of magnitude below densities that could affect the laser-plasma interaction. A picture of this experimental arrangement is seen in Fig. 5.1. The CO_2 laser pulse is coupled into the vacuum chamber in a 10 cm beam through a wedged NaCl window. Transport losses of ∼40% between the final amplifier and the target chamber leave ∼60 J of energy for use in the experiment. To achieve the maximum intensity from the available energy in the laser beam, we used an F/1.5 40° off-axis parabolic (OAP) mirror to focus the laser beam. Such a tight focus results in a Rayleigh range of $z_r \sim 200$ μm (the distance at which the spot size of the laser increases by a factor of $\sqrt{2}$). Therefore a computer controlled three-axis stage powered by motorized actuators was constructed to precisely control the position of the target in the laser focus.

The target is a supersonic hydrogen gas jet operated around Mach 1.8 similar to that described in [98]. The nozzle has a conical shape with a 500 μm throat and a 1 mm opening. Operating the nozzle at supersonic speeds ensures minimal lateral expansion of the gas as it exits the nozzle opening providing a high density column of gas millimeters above the gas jet. The gas density profile measured along the laser axis at a height of 1 mm above the nozzle is 1-2 mm long (described in detail in Section 6.2.3) and the peak

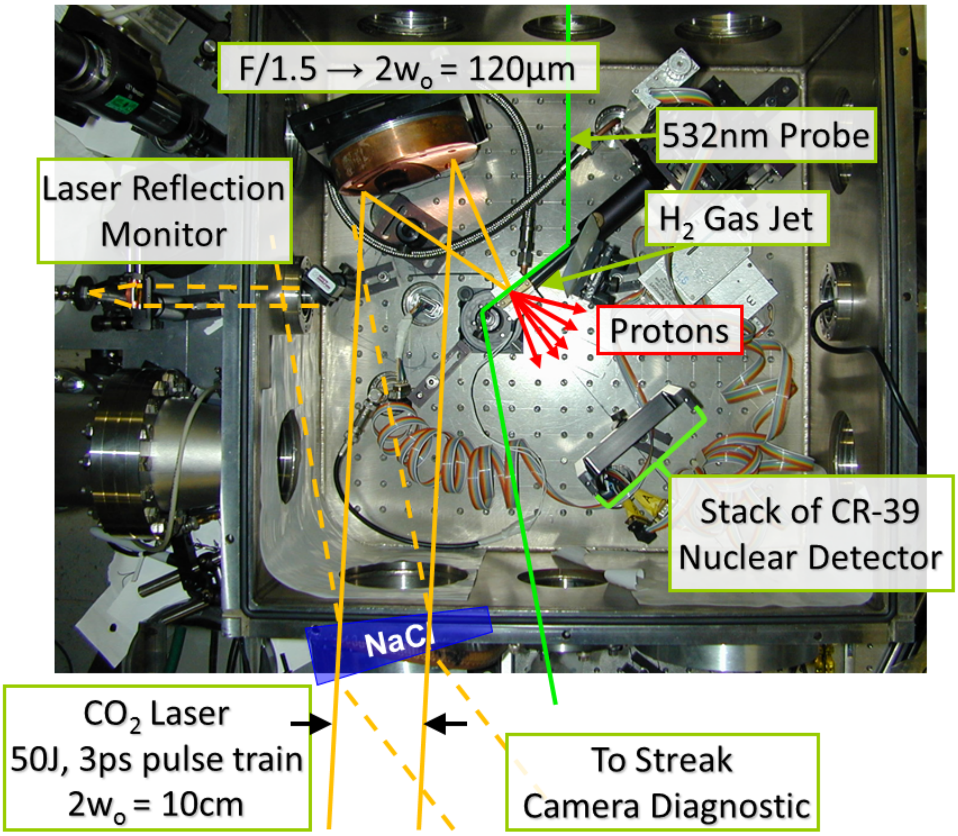

Figure 5.1: Picture of the vacuum target chamber. Drawn in are the main high power CO_2 beam line (yellow), the CO_2 plasma reflection diagnostic (dashed yellow), and the 532nm interferometry probe line (green).

density at the center is typically above the critical plasma density, n_{cr}, for 10 μm radiation (10^{19} cm^{-3}).

In such a gas density profile, the laser-plasma interactions can be quite complicated as well as involve dynamic modifications to the profile. Additionally, a significant portion of the CO_2 laser beam can be reflected from the plasma by the build up of laser-plasma instabilities [79] in the long underdense plasma region or by specular reflection from the overcritical density surface [79]. For this reason, the 10 μm transmission through and reflection from the plasma are monitored with energy meters. The transmission energy meter is simply placed ~15 cm downstream from the gas jet off the laser axis to sample

$\sim$6% of the beam. Of the light that reflects backwards from the plasma, 4% then reflects off the internal side of the wedged NaCl window toward the OAP where a small mirror sends a sample of the beam to an energy detector outside the vacuum chamber (see yellow dashed lines in Fig. 5.1). Both the transmission and reflection measurements are normalized to a full power laser shot without firing the gas jet (in vacuum). Finally, due to a shot-to-shot variation in the laser energy and macropulse structure, it was necessary to measure the temporal profile on each shot with the streak camera diagnostic (Appendix A) using the 4% reflection from the external side of the wedged NaCl window (blue dashed lines in Fig. 5.1).

5.2 Laser Focus Measurements

The focus of the 10 μm laser beam was characterized using an IR camera with a magnifying imaging system. The spatial profile of the beam was measured (without final amplification) while scanning along the laser axis (denoted $\hat{z}$). Due to residual astigmatism of the beam, its spatial profile was observed to be a elliptical and therefore a horizontal (w_h) and vertical (w_v) radius is extracted for each $\hat{z}$ position and plotted as seen in the blue and green traces, respectively, in Fig. 5.2. The red trace is an effective radius calculated as $w_{eff}^2 = w_h \cdot w_v$, which represents the intensity distribution of the laser beam. These are compared to ideal Gaussian beam profiles for an F/1.5 (dashed black) and an F/3 (dashed brown) focusing geometry.

The clear horizontal ellipse before and vertical ellipse after the focus can be seen by the green and blue traces in Fig. 5.2 resulting from the astigmatism of the laser beam. The spot size for the unamplified beam is measured to be $w_o = 70$ μm. However, the beam divergence appears to match more closely that of the F/3.75 geometry. Using this geometry to trace backwards to the OAP indicates an input beam size of 4 cm as compared to the 10 cm beam (F/1.5 geometry) observed after final amplification. This difference in beam sizes between the amplified and unamplified beams is due to saturation in the final

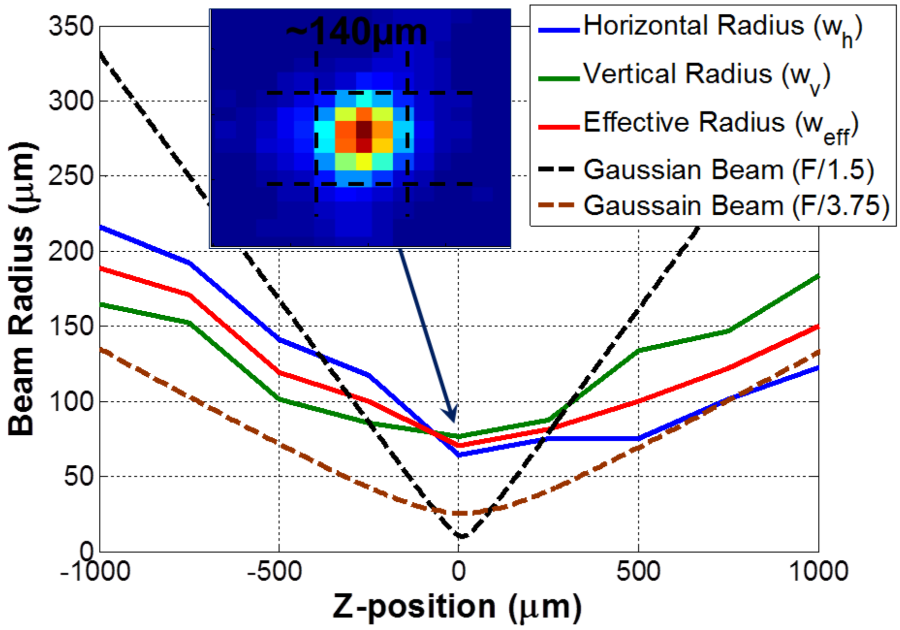

Figure 5.2: 10 μm laser beam radii (horizontal, vertical, and effective) compared to ideal Gaussian beam radii (F/1.5 and F/3.75 geometries) plotted along the laser axis ($\hat{z}$). The insert is an IR camer image of the best focus for the unamplified pulse showing a beam size of $2\mathrm{w}_o = 140$ μm.

amplification which occurs stronger on axis thus widening the diameter of the amplified laser beam. Also observed in Fig. 5.2 is the M^2 factor due to beam distortions equaling $\omega_{eff}/\omega_{F/3.75} = 2.7$. Multiple factors contribute to the non-optimal focus of the laser beam. First and foremost, the many small angle reflections from telescope mirrors impart and ellipticity in the beam. Also associated with each of these reflections is a spherical abberation which worsens throughout the system. Finally, small phase front distortions can result from the reflection from and transmission through damaged or imperfect optics. Though no single instance of these effects causes a large distortion, their accumulation over $\sim$100 optics in the Neptune laser system results in the observed final focus.

Estimating the amplified beam focal spot size is difficult due to the saturation effect mentioned previously. Not only does this increase the size of the beam which changes the F# focusing geometry, but it results in a flat-top profile which has an increased M^2 value as compared to the Gaussian unamplified beam profile. However, one can extract the beam size by observing the ionization of a gas as proof of the focused intensity in combination with knowledge of the energy and temporal with of the laser pulse. This measurement has been performed for the current focusing geometry resulting in an estimated focused radius of $w_o = 60\ \mu$m. For a typical CO_2 pulse train as shown in Fig. 4.5 in Chapter 4, the peak micropulses can reach intensities of up to $3.3\text{x}10^{16}$ W/cm^2, or a normalized vector potential of $a_o \sim 1.8$ for 10 μm radiation.

5.3 CR-39 Proton Detection System

The detection of accelerated ions is frequently accomplished using one or more of these techniques: radiochromic film (RCF) dosimetry, fluorescence, and nuclear track recording. RCF has an active monomer layer which polymerizes after exposure to ionizing radiation or particles [99]. This reaction causes a change in color of the film and can be analyzed by densiometry to obtain quantitative information about the dose of absorbed radiation. The total yield of detected ions is then calculated based upon optical density versus dose calibration curves for the specific type of film used, ie. GafChromic MD-55, HS, and HD-810 films [100,101]. Fluorescers, on the other hand, are materials whose atoms absorb the energy of a photon or energetic particle by changing electronic energy states. When these excited states relax they emit a photon which can be observed by a CCD camera. Here the calculation of the total detected ion yield is based upon knowledge of the quantum efficiency of the fluorescer (energy emitted verses incident energy) and an estimation of the total fraction of emitted light collected. For ions, typically a scintillator is used due to its advantageous quantum efficiency as compared to other flouressors (eg. Saint Gobain BC-400 with QE = 10^5 photons/20 MeV proton). Unfortunately, there are two major limitations of both of these detection principles. First, their respective reactions (color change or atomic excitation) are also sensitive to energetic electrons and photons, both of which are common emission from the interaction of an intense laser pulse with a plasma.

Therefore, additional filtering techniques are needed when using these materials to void the detection system of false ion signals. Second, because of the complications involved in the calculation of the total ion yield inferred from a secondary collective signal, oftentimes they are cross-calibrated with the a direct single ion detection system : CR-39 nuclear track recorders.

CR-39, or allyl diglycol carbonate, is a clear plastic polymer that is commonly available with an optical polish in many shapes and sizes due to its widespread use for eyeglass lenses. It was first suggested in 1978 that CR-39 may be used for the detection of accelerated ions through the production of damaged tracks [102]. As an ion propagates through the CR-39 material, it ionizes and destroys molecular bonds in a very localized area along its path. These damaged areas are revealed as cavities, or pits, by etching the CR-39 in a basic solution, typically NaOH. The clear advantage of using CR39's for ion detection is their response to a single ion allowing for an unambiguous determination of ion yield. This quality was explicitly displayed by Hara *et al.* by extracting a single He ion from and accelerated beam and detecting it with a CR-39 plate [103]. These etched pits can be observed on a micron spatial scale using traditional microscopes and even the sub-micron scale with atomic force microscopes [104] allowing for a high spatial resolution in a CR-39 detection system. However, these advantages come with the drawback of post-processing. Not only is the etching and counting of pits a time consuming and meticulous process, it also prevents CR-39's from being an online diagnostic.

CR-39's can also be used to deconvolve the spectrum of certain ions due to their nonlinear loss of energy while propagating through a dielectric medium. As an ion travels through a dielectric, it loses its energy primarily due to inelastic collisions with the atomic electrons of the material. These collisions could result in ionization or simply excitation of the atomic electrons. This process was analytically described using quantum mechanics by Bethe and Bloch resulting in the following formula for the energy lost per unit length [105]:

$$\frac{dE}{dx} = -2\pi N_a r_e^2 m_e c^2 \rho \frac{Z}{A}\frac{z^2}{\beta^2}\left[\ln\left(\frac{2m_e\gamma^2 v^2 W_{max}}{I^2}\right) - 2\beta^2\right] \tag{5.1}$$

where :

$$W_{max} = \frac{2m_e c^2\beta^2\gamma^2}{1 + 2(m_e/M_i)\sqrt{1+\beta^2\gamma^2} + (m_e/M_i)^2}$$

$\beta = v/c$: normalized ion velocity

$\gamma = 1/\sqrt{1-\beta^2}$: relativistic Lorentz factor

$N_a = 6.022\text{x}10^{23}$ mol^{-1} : Avogadro's number

$r_e = 2.817\text{x}10^{-13}$ cm : classical electron radius

$m_e = 9.11\text{x}10^{-31}$ kg : electron mass

$M_i = 2.67\text{x}10^{-27}$ kg : proton mass

$c = 3\text{x}10^8$ m/s : speed of light

$\rho = 1330$ kg/m^3 : density of CR-39

$Z = 146$: atomic number of CR-39

$A = 272$: atomic weight of CR-39

$z = 1$ e : charge of a proton in units of e

As the ion loses energy in the CR-39 material, the slower moving ion has a larger collisional cross-section thus increasing its energy deposition rate (dE/dx α $1/\beta^2$ in Eq. 5.1). This results in a nonlinear increase to the deposited energy as the ion propagates culminating with the peak deposition of energy in a thin layer where the ion stops, called the Bragg Peak. This can be seen in Fig. 5.3 which is an iterative plot of Eq. 5.1 for a proton propagating through CR-39 (see parameters above) with an initial energy of 20 MeV.

The response of the CR-39 to this energy deposition is obtained through chemical

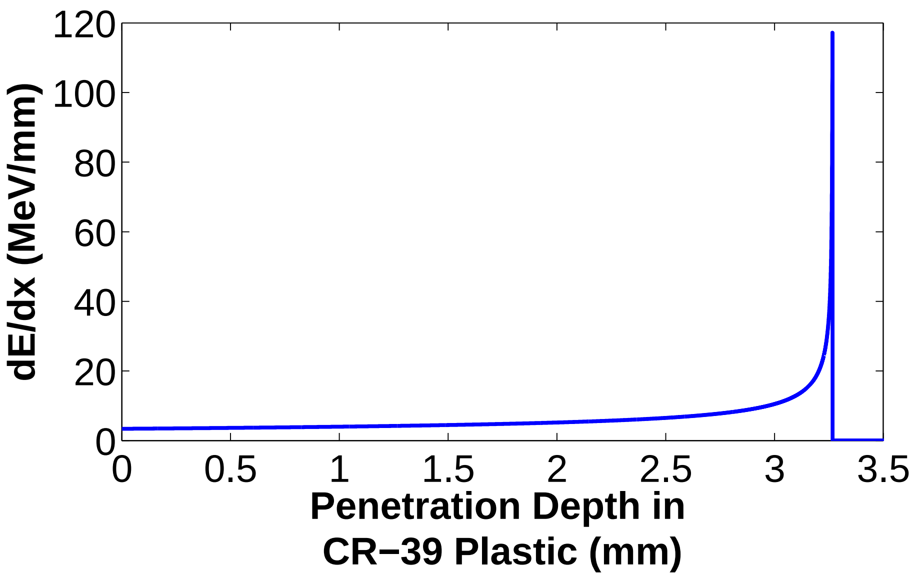

Figure 5.3: Energy deposition of a proton propagating through CR-39 with an initial energy of 20 MeV

etching. It is commonly characterized by the ratio of the etch rate in the vicinity of the damaged areas, called the track etch rate V_t, as compared to the bulk material etch rate, V_b. If V_t is larger than V_b, it is possible for an etched track to form and be observed under a microscope. This response increases with increasing charge of the ion, Z, or with decreasing velocity, $\beta = v/c$, due to an increase in the collisional cross-section of the ion with atomic electrons. It is predicted that observable tracks will form in CR-39's at a Z/β as small as 8-10 (ref. [102], [106]). This minimum threshold of Z/β for an ion to produce an observable pit is the key to the determination of its energy. To illustrate this fact, using the data from the dE/dx plotted in Fig. 5.3, the Z/β ratio (with $Z = 1$ for protons) is calculated as a function of propagation distance in the CR-39 and shown in Fig. 5.4.

The functional dependence of Z/β on propagation distance is very similar to that of the energy deposition remaining relatively low until the proton nears the end of its trajectory (black dashed line in Fig. 5.4). For the majority of the distance, the proton will not leave observable damage until near its Bragg Peak. This allows for the discrimination

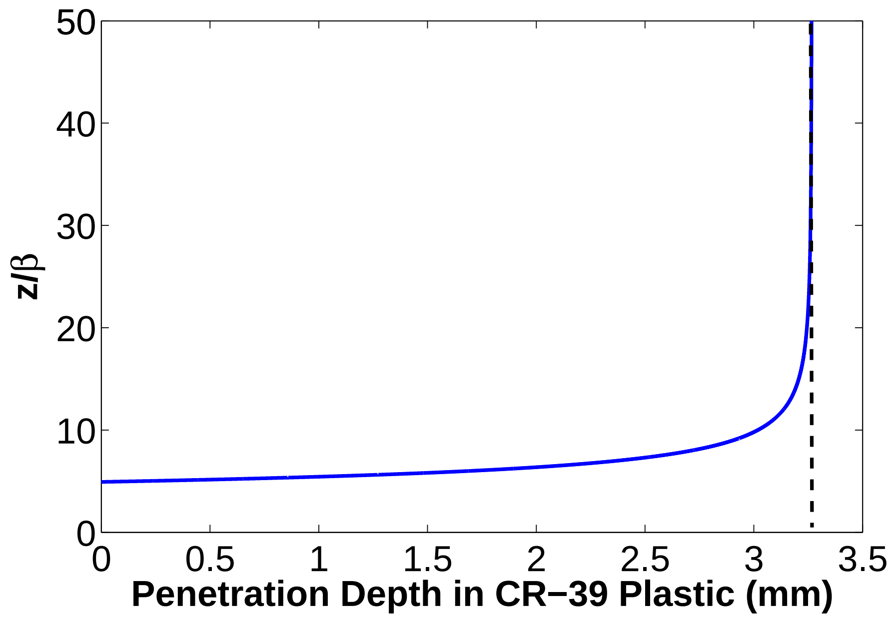

Figure 5.4: The ratio of the ion charge, Z, over the normalized velocity, β, plotted versus propagation distance in CR-39 for an ion with an initial energy of 20 MeV. The vertical black dashed line represents where the ion stops ($\beta \sim 0$).

of protons with different energies corresponding to different positions of their respective Bragg Peaks. Thus it is possible to achieve a high energy resolution by observing the onset of proton related damage in small distance increments while etching into a CR-39 plate.

The CR-39 detection system used in the LDIA experiment is depicted in Fig. 5.5a. A stack of five 1 mm thick detectors were placed 15 cm downstream from the gas jet and span 100x100 mm^2 subtending a solid angle of 36°, which contains the full F/1.5 expansion of the laser beam. Each 1 mm detector consists of four 50x50 mm^2 pieces of CR-39 held together in a frame as shown in Fig. 5.6. In Fig. 5.5b, the energy deposition of protons traversing CR-39 plastic is plotted versus distance where the Bragg peaks are clearly visible. This is plotted for a single energy of protons ranging from 1-25 MeV in discrete 1 MeV steps. Superimposed on this plot are the edges of five 1 mm thick CR39's (shown in black dashed lines) to display the spectral sensitivity of the detection system.

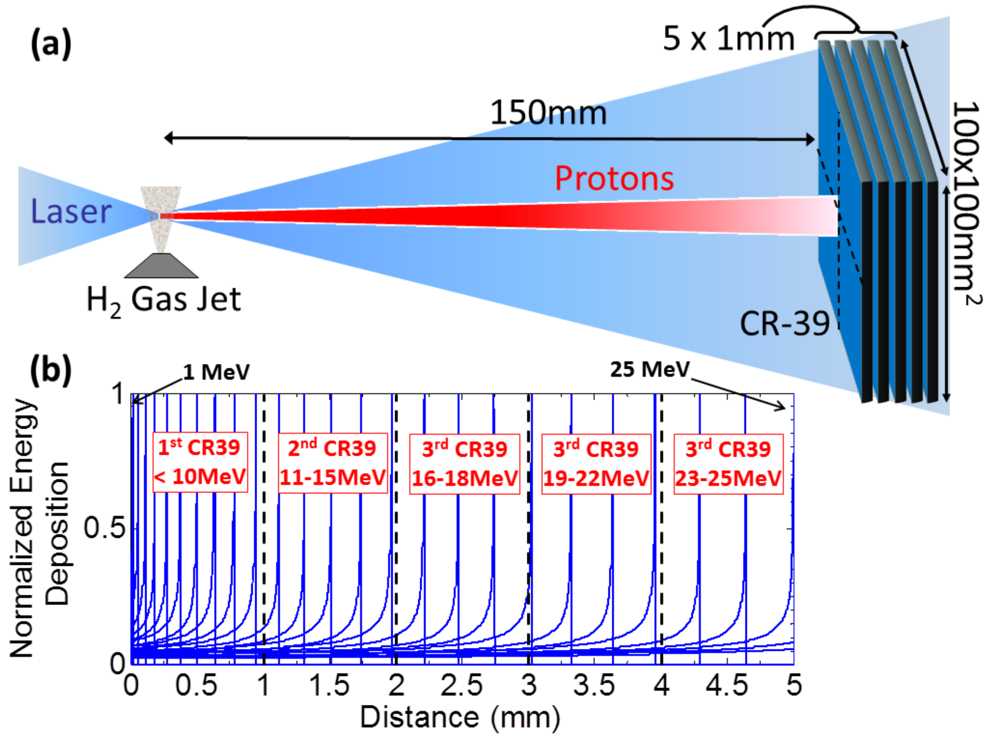

Figure 5.5: Depiction of the experimental arrangement for proton detection (a), the proton energy deposition versus propagation length in CR-39 plastic (b). Overlayed in (b) are the detection ranges of the five 1 mm thick CR-39 pieces.

The five CR39's will detect protons of energies $<$ 10 MeV, 11 - 15 MeV, 16 - 18 MeV, 19 - 22 MeV, and 23 - 25 MeV, respectively. After exposure to protons, each CR-39 in a detection stack is etched for 5 hours producing one energy bin or data point on the front and back side. For spectra necessitating finer spectral resolution, further etching of the corresponding CR-39 in 5 hour increments up to a total of 20 hours was performed effectively moving the plane of detection by small increments deeper into the CR-39. A detailed description of the processing and analysis of the exposed CR-39's can be found in Appendix B. The spectral resolution of the detection system is 0.1 MeV at a central energy of 20 MeV, and the background noise level is $\sim$100 counts.

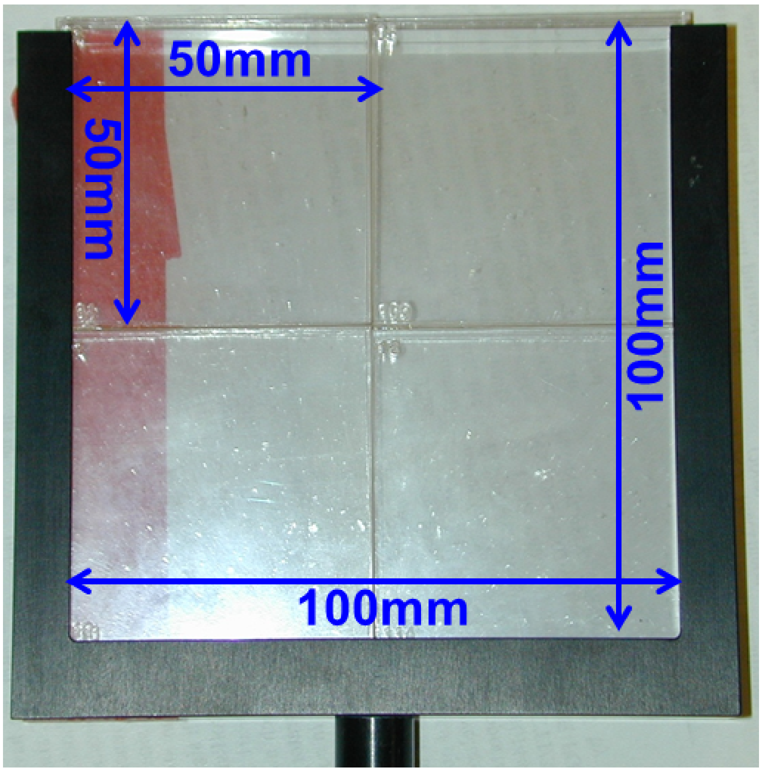

Figure 5.6: A picture of one detection stack of CR-39's. The whole stack spans 100x100 mm^2, where each 1 mm thick layer consists of four individual 50x50 mm^2 pieces of CR-39.

5.4 Conclusion

An experimental arrangement for the acceleration of protons via the interaction of a high power CO_2 laser pulse with a H_2 gas jet is presented. The spot size of the laser through the F/1.5 focusing OAP has been measured and revealed an astigmatism in the beam evidenced by a horizontal beam shape before the focus and vertical beam shape after the focus. The beam waist has a radius of $w_o = 60\ \mu$m yielding a peak intensity of 3.3x10^{16} W/cm^2, or a normalized vector potential of $a_o \sim 1.8$.

CR-39 nuclear track detectors are used for the measurement of the yield and spectrum of the accelerated protons. The advantages of this detection system is the unambiguous sensitivity to only ions as opposed to RCF or scintillator plates which are sensitive to electrons and x-rays. These advantages come at the cost of time-consuming post-processing and the delay in measurement results. In addition, CR-39's are limited in their ability to detect different ion species and monoenergetic ion beams. First, there is no discerning between ions of different species and heavier ions have such a short penetration distance on the MeV energy-scale so there is practically no spectral resolution. In our case with protons, spectral resolution is possible but initially limited by the millimeter width of the CR-39. Finer spectral resolution could be obtained with thinner CR-39's which are available down to $\sim$100 μm widths; however, they become fragile and warped especially after chemical etching, which strongly limits their practicality in precise microscopic analysis. To circumvent this limitation, we developed and implemented the incremental etching technique described in Appendix B with some success, though there are limitations here as well. First, in terms of time spent in etching and analyzing CR-39's, it is not practical to apply this incremental etching method to all exposed CR-39's. Therefore, a monoenergetic proton beam needs to deposit its energy near the edges of the millimeter thick CR-39's for it's existence to be uncovered in the first round of etching. Therefore, successful proton acceleration producing a monoenergetic beam could be missed if the entire beam's spectrum lies within the bulk of the millimeter thick CR-39. Second, it was observed that the surface roughness of the CR-39 increased as it was etched further into the bulk. This surface roughness produced more noise, or false pits as observed by a microscope, which limited the depth of accurate measurements to $\sim$200 μm from the initial clean surface. To circumvent all the above mentioned problems and provide cleaner measurements of the spectrum of accelerated ions, a magnetic spectrometer or Thompson parabola can be used with care taken to filter out electrons and x-rays.

CHAPTER 6

Characterization of the Laser-Plasma Interaction

6.1 Introduction

The evolution of the plasma density profile during a laser-plasma interaction provides pertinent information for the diagnosis of the physical processes occurring therein. This is especially true with an extended plasma density profile with a peak density around the critical plasma density for the incoming laser light which can result in a strong modification of the plasma profile [79]. The hole boring through the plasma, as well as the inhibition of laser ionization of the gas behind the n_{cr} layer, are dynamics important to the LDIA experiment and necessitated a temporally resolved measurement of the plasma density profile.

One way to obtain information about the plasma density profile is to probe it with a short laser pulse in various configurations such as interferometry [107], Thompson scattering [108], shadowgraphy [109], Schlieren [109], etc. Although there are advantages to each method of probing, interferometry is the most convenient method of obtaining quantitative information of the 2D plasma density profile transverse to the pump laser pulse and was therefore implemented in the LDIA experiment. For temporal resolution, consideration of the time scale of the plasma movement (discussed below) results in the necessity of a picosecond probe pulse. As described in Chapter 4, the 3 ps CO_2 laser seed pulse is produced by using a <3 ps 1 μm pulse from the Nd:Glass CPA system. This pulse is intrinsically synchronized with the final amplified 10 μm pulse and can serve as a probe pulse for CO_2 laser driven plasmas.

In this chapter, we present the experimental setup of a Mach-Zehnder interferometer used to measure the plasma density profile at various time delays with respect to the main CO_2 laser pulse. The description includes the production of the probe light and its transportation to the vacuum target chamber, the experimental arrangement of the Mach-Zehnder interferometer, and the synchronization of the probe and CO_2 laser pulses.

6.2 Mach-Zehnder Interferometry for CO_2 Laser Driven Plasmas

A basic interferometer involves first splitting a probe pulse into two arms, hereafter referred to the signal and reference arms. The signal arm is sent through the plasma and then combined with the reference arm at a slight angle to form an interference pattern. The peaks, called fringes, of the interference pattern are directly related to the phase difference between the signal and reference arms. Under conditions where there is no plasma in the signal arm, the crossing angle of the two arms provides an interference pattern with straight fringes. Once the plasma is present in the signal arm, the phase change experienced by the probe rays that pass through the plasma will shift the positions of the fringes in the interference pattern in direct proportion to this extra phase. The plasma density can then be calculated from this phase change.

The shift in the phase as observed in the interference pattern between the 'plasma' and 'no plasma' conditions can be written as :

$$\Delta\phi = \int_{-\infty}^{\infty} (k_p - k_o)\, dz \tag{6.1}$$

where $\Delta\phi$ is the phase shift due to the plasma, k_p and k_o are the wave numbers of the signal arm under 'plasma' and 'no plasma' conditions, respectively, and z is the propagation direction of the probe light. This expression can be written in terms of the index of refraction :

$$\Delta\phi = \left(\frac{2\pi}{\lambda}\right)\int_{-\infty}^{\infty}(1 - n_p(z))\,dz \tag{6.2}$$

where λ is the wavelength of the probe pulse, n_p is the index of refraction of the plasma, and 1 is the index of refraction of vacuum ('no plasma' case). Noting that the index of refraction of a medium is equal to the ratio of the speed of light in vacuum to the speed of light in the medium, it can be can be expressed in terms of the plasma density by use of the plasma dispersion relation :

$$\frac{c^2k^2}{\omega^2} = n_p^2 = 1 - \frac{\omega_p^2}{\omega^2} \tag{6.3}$$

where c is the speed of light, k is the wave vector of the probe, ω is the frequency of the probe, $\omega_p = \sqrt{\mathbf{n}_p e^2/m\varepsilon_o}$ is the plasma frequency, $\mathbf{n}_p$ is the plasma density, e and m are the charge and mass of an electron, and ε_o is the permittivity of free space. If the probe frequency is much greater than the plasma frequency, the index of refraction of the plasma can be approximated as :

$$n_p \approx 1 - \frac{1}{2}\frac{\mathbf{n}_p}{\mathbf{n}_{cr}} \tag{6.4}$$

where $\mathbf{n}_{cr} = (4\pi^2 m\varepsilon_o c^2)/(e^2\lambda^2)$ is the critical plasma density for the probe wavelength. Substituting Eq. 6.4 into Eq. 6.2 yields an integral over the density profile of the plasma :

$$\Delta\phi = \left(\frac{\pi}{\lambda\mathbf{n}_{cr}}\right)\int_{-\infty}^{\infty}(\mathbf{n}_p(z))\,dz \tag{6.5}$$

Finally, with the $\Delta\phi$ measured from an interferogram, Eq. 6.5 can be numically solved using Abel inversion [110] for an arbitrary but axisymmetric plasma density profile. If a certain profile is assumed, such as Gaussian or rectangular, one can analytically solve for the plasma density yielding :

$$\text{Gaussian} : \mathbf{n}_p(z) = \mathbf{n}_{p,max} e^{-z^2/L^2} \;\Rightarrow\; \mathbf{n}_{p,max} = \frac{\Delta\phi}{2\pi}\frac{\lambda}{L_g}\frac{2}{\sqrt{\pi}}\mathbf{n}_{cr} \tag{6.6}$$

$$\text{Rectangular} : \mathbf{n}_p(z) = \mathbf{n}_p \;\Rightarrow\; \mathbf{n}_p = \frac{\Delta\phi}{2\pi}\frac{\lambda}{L_f}2\mathbf{n}_{cr} \tag{6.7}$$

where L_g is the $1/e$ half width of the Gaussian profile and L_f is the full width of the rectangular profile.

6.2.1 Generation and Transport of the 532 nm Probe Pulse

In the selection of a probe pulse of wavelength λ and pulse duration $\Delta\tau$, it is important to consider the effect of refraction, temporal resolution of the plasma dynamics, and the ease of production, transportation/alignment. Density gradients in the plasma that are transverse to the probe propagation translate to gradients in the index of refraction (Eq. 6.4) and will refract the probe light. Although refraction will not affect to first order the phase information on the light ray, it can strongly distort the image of the interference fringes resulting in a loss of data. From simple geometric considerations, an approximation to the angle of refraction, θ, of light traveling through an inhomogeneous medium can be written as $\theta = (L/n_o)(dn/dx)$ [109], where L is the length of the medium, n_o is the average index of refraction, and dn/dx is the change in index across one transverse dimension. From this expression in combination with Eq. 6.4, as n_{cr}/n_p increases, the effect of refraction decreases. Therefore, for an experiment with a fixed plasma density, a short enough wavelength should be chosen for a probe beam such that its n_{cr} is far above this density. For the LDIA experiment involving plasma densities around n_{cr} for the 10 μm radiation (10^{19} cm^{-3}), probe wavelengths in the visible spectrum have a n_{cr}/n_p $\sim$ 400 which is suitable for all but very strong density gradients (dn/dx large). The additional benefit of ease of transportation and alignment of visible wavelengths makes them a desirable choice.

The second harmonic of the aforementioned 3 ps 1 μm, or 532 nm, fits the above criteria and is easily generated using a KDP crystal. The energy conversion efficiency of the SHG process is 30% yielding 300 μJ at 532 nm from the 1 mJ of fundamental 1 μm light. To temporally resolve the plasma dynamics, the probe pulsewidth should be short on the timescale of the movement of the plasma which is expected to be on the order of the ion sound speed, $C_s = \sqrt{kT_e/M_i}$, where k is the Boltzmann constant, T_e is the electron temperature, and M_i is the ion mass. For an electron temperature of $kT_e = 1$ MeV (approximated by ponderomotive heating of the plasma [42]), $C_s = 12.6$ μm/ps. For a probe pulsewidth of ~ 2 ps (SHG process yields a $\sqrt{2}$ shortening from the fundamental) the plasma density profile may shift by 25 μm. Since this value is at the spatial resolution limit of the interferometer, the probe pulsewidth is adequate.

Generating the 532 nm probe and the 10 μm seed pulses from the same 1 μm pulse ensures the two pulses are inherently synchronized on each laser shot. However, the one challenge of this method is that the probe pulse is generated very early in terms of the experimental timing sequence and therefore needs to be delayed greatly to arrive at the IP at the same time as the CO_2 laser pulse. Specifically, after the 10 μm seed pulse is generated, it undergoes regenerative amplification (many round trips), final amplification (three 2.5 m passes), and long transportation distances between the two amplifiers and the IP, which when summed together delays its arrival by 592 ns or 178 m. Therefore, the probe pulse needs to be delayed accordingly by the same time.

For this purpose, an optical delay line (depicted in Fig. 6.1a) was designed to incorporate this long delay in the probe beam transport to the IP. Two optical tables separated by 10 m supported 1" - 2" optical mirrors and lenses to guide the probe beam through 13 table-to-table reflections before finally continuing to the IP. To aid in designing the telescopes used to control beam diffraction over such long distances, an in-house optical ray tracing program written in Matlab [111] was used to model the transport. Fig. 6.1b displays the approximate beam diameter ($2w_o$) for an ideal Gaussian beam profile throughout the transport system. The vertical lines represent mirrors (red) and lenses (green).

The beam diameter is plotted for the probe pulse from its generation to the IP where

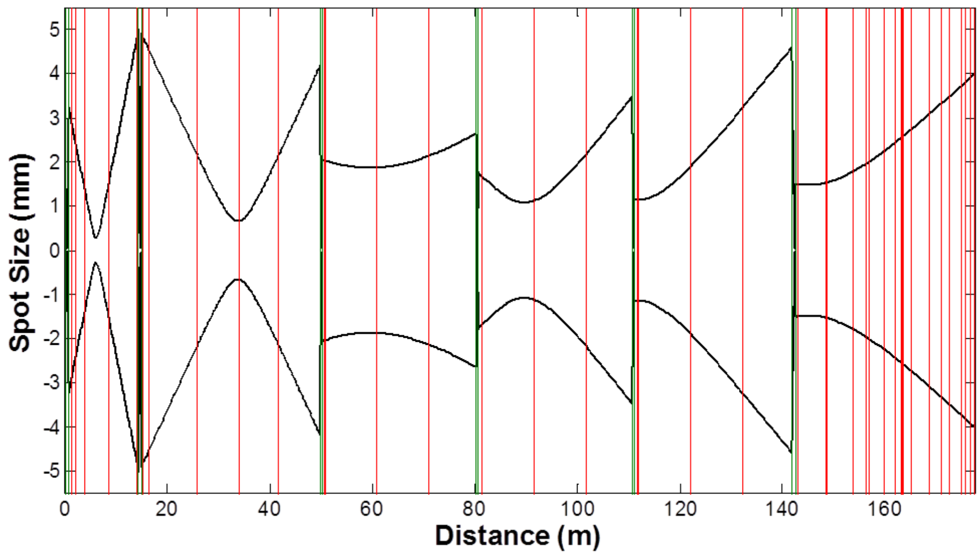

Figure 6.1: Ideal Gaussian beam diameter ($2w_o$) plotted versus propagation distance through the probe pulse transport system from its generation to the IP. Mirrors and lenses are represented by red and green vertical lines, respectively. The plot was generated by an in-house optical ray tracing program written in Matlab [111].

the 13 passes separated by 10 m can be seen in the range of ∼20 - 140 m along the x-axis. In the experiment, the beam profile is very non-Gaussian from the beginning which is exacerbated by the very long propagation distances allowing diffraction of the non-Gaussian rays to lead to transport losses and a severe degradation of the beam profile. The total throughput of the transportation system from the pulse generation to the IP is ∼7%. To obtain a homogeneous Gaussian beam profile for probing, the pulse is then focused through a 25 μm pinhole for spatial filtering with a throughput of ∼10%. The remaining few microjoules are sufficient for visual alignment of the probe beam and illumination of the CCD cameras.

6.2.2 Experimental Arrangement of the Mach-Zehnder Interferometer and Synchronization

After transportation and spatial filtering, the probe pulse is used in a Mach-Zehnder interferometer as depicted in Fig. 6.2. The input probe beam is split and combined at beam-splitters BS1 and BS2 with the signal arm passing through the target chamber and plasma. A delay stage (DS1) was inserted into the reference arm to precisely temporally overlap the signal and reference arm at BS2 creating an interference pattern. Finally a f = 30 cm lens was placed 40 cm from the plasma to image the plasma plane onto the CCD camera with a measured resolution of ~20 μm and magnified field of view of 1.5 x 2.0 mm.

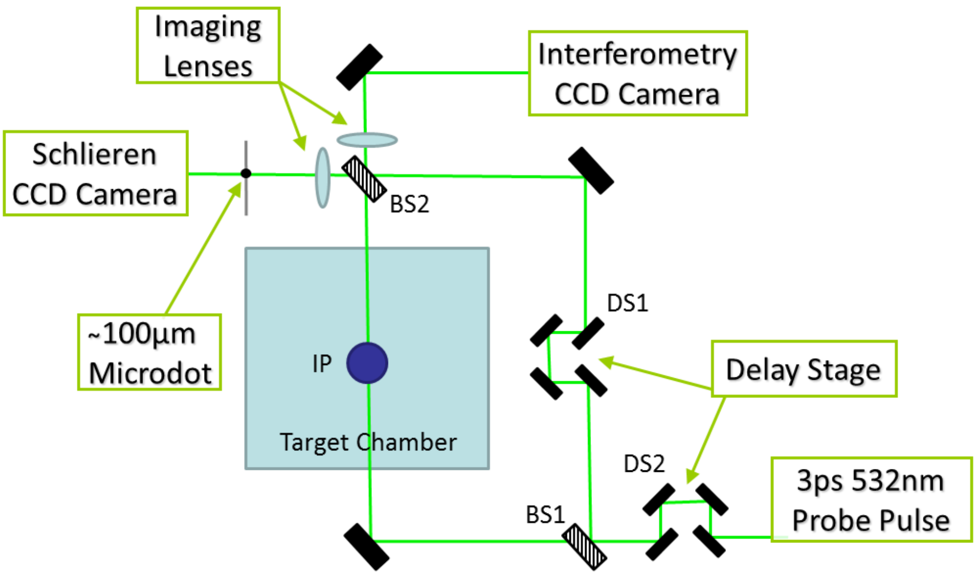

Figure 6.2: Experimental setup for the Mach-Zehnder interferometry and Schlieren setup using a 532 nm 2 ps long probe pulse.

Though the probe pulse and CO_2 macropulse are inherently synchronized, the pulses must be temporally overlapped at the IP with a picosecond accuracy. For this purpose, we used a Si semiconductor switch [91] controlled by the green pulse for a cross-correlation measurement. Here, a piece of Si is placed at the IP normal to the bisection of the probe and CO_2 laser pulses. Normally it transmits a large fraction of the 10 μm light but absorbs the 532 nm light which has a photon energy exceeding the bandgap of Si. As the 532 nm photons are absorbed, an electron-hole plasma is formed on the surface of the Si eventually modulating the transmission/reflection of the 10 μm light as the plasma density reaches and surpasses n_{cr} for 10 μm radiation.

For maximum reflection of the 10 μm light from the Si plate, an absorbed fluence of $\sim$2 mJ/cm^2 is required [91, 112]. Due to the very limited energy in the probe beam, for this measurement the spatial filter was removed producing $\sim$20 μJ at the IP, of which $\sim$50% is reflected because the index of refraction of Si at 532 nm is 4.2. Focusing the probe beam to approximately three times the 10 μm beam diameter of $2w_o = 120$ μm produces a peak fluence of 10 mJ/cm^2 which is sufficient for efficient reflection/absorption of the 10 μm radiation.

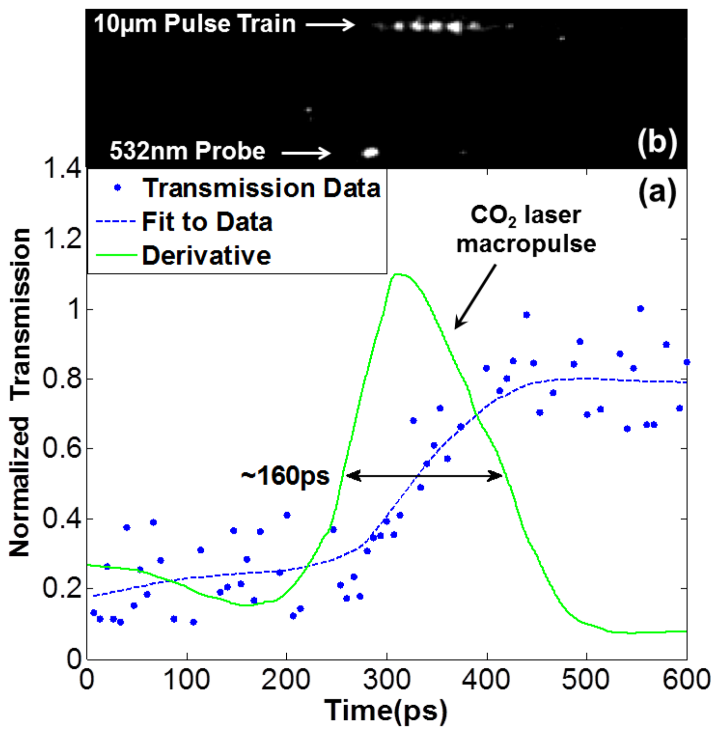

Figure 6.3: Results of the cross-correlation measurement of the 2 ps 532 nm probe pulse with the 10 μm pulse train (a), and a raw streak camera image showing the relative delay between the laser pulses (b).

A typical result of the cross-correlation measurement is shown in Fig. 6.3a. The data points represent the normalized transmission of 10 μm light through the Si plate versus the delay in the probe pulse (using DS1). When the probe pulse arrives early, the 10 μm light is screened by the plasma, and when the probe pulse arrives later the 10 μm light is transmitted. The blue dashed line represents a fit to the data and the solid green line is the derivative of the fit. This derivative then correlates to the temporal width of the 10 μm pulse train which was measured to be $\sim$160 ps (FWHM). Fig. 6.3b shows a typical streak camera image where the temporal delay between the 10 μm pulse train and the 532 nm probe represents probing in the middle of the pulse train.

The uncertainty of the probe timing is dominated by two factors : scattering of the data of the cross-correlation measurement and identification of the 1^{st} pulse in the CO_2 macropulse in the streak image. Shot-to-shot fluctuations in the pointing of the green beam through the 172 m transport system and ultimately the 50 μm spatial filter caused its energy to fluctuate $\pm$50%. This along with the shot-to-shot fluctuations in the 10 μm macropulse cause a scattering in the 10 μm transmission data (as seen in Fig. 6.3a) which in combination with a poor signal to noise ratio resulted in a $\pm$15 ps accuracy to the identification of the middle of the CO_2 macropulse. In addition to this, the extraction of the probe timing on any given laser shot relies on a comparison of its streak image with that of the cross-correlation. This in turn relies on identifying the 1^{st} pulse in the 10 μm macropulse on the streak camera. Due to the signal to noise ratio of the streak camera image, this identification has a $\pm$ one pulse (or $\pm$18 ps) accuracy. Note, however, that in the comparison between probe timings of two different shots, the former uncertainty is subtracted out as it is the same on both shots. This is the case, for example, for the measurement of the hole boring velocity described below.

6.2.3 Gas Jet Density Profile Measurement

The profile of the gas jet was characterized with a similar Mach-Zehnder interferometer using a 800 nm 40 fs Ti:Sapp laser pulse both as the pump and probe. The supersonic gas jet is operated around Mach 3 and has a nozzle of conical shape with a 500 μm throat and a 1 mm opening similar to that described in ref. [98]. The gas jet profile is characterized at a height of 1 mm above the nozzle along the CO_2 laser axis. A typical Abel inverted [113] plasma profile for a H_2 pressure of 100 psi is shown in Fig. 6.4 which reveals a quasi-triangular profile with a FWHM of ~800 μm and a peak plasma density of ~1.8x10^{19} cm^{-3}. The peak density is found to be linearly proportional to gas pressure and can be varied from 5x10^{18} to 10^{20} cm^{-3} which corresponds to 0.5 to 10 times the critical plasma density for 10 μm light (10^{19} cm^{-3}).

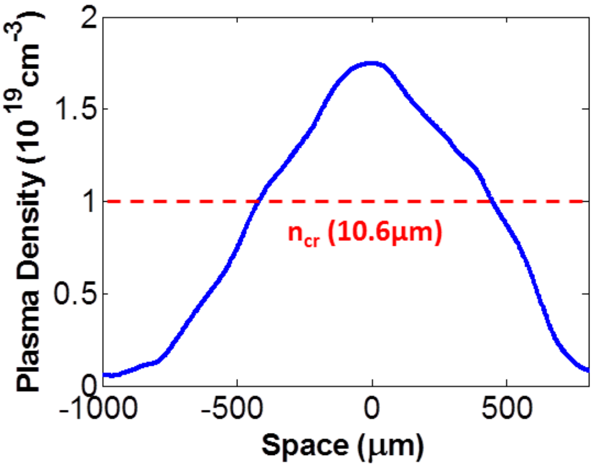

Figure 6.4: Abel inverted plasma density profile for the gas jet using low power Ti:Sapp laser interferometry. The plasma profile is obtained at a height of 1 mm above the gas jet (along the CO_2 laser axis) at a H_2 pressure of 100 psi. The phase retrieval from the interferogram and Abel inversion was performed with an in-house Matlab software program [113].

6.3 Dark Field Schlieren Measurements

In addition to the Mach-Zehnder interferometer, a Schlieren diagnostic was implemented to obtain qualitative information about the general shape of plasma profile to complement the interferograms. Put simply, the Schlieren technique images the refraction experienced by a probe beam as it passes through an object, here the plasma. This is accomplished by partial or whole preferential blocking the unperturbed light (dark-field) or the refracted light (light-field). This preferential blocking will produce an intensity pattern on a CCD camera (imaging the object plane) yielding information on the object's gradients in index of refraction, corresponding to gradients in density for a plasma (Eq. 6.4).

There are many methods of preferential blocking of the unperturbed or refracted light and all involve placing an object of a certain shape in the focus of the probe beam after passing through the plasma [109]. In the LDIA experiment, the probe beam that reflects off of BS1 after passing through the plasma (see Fig. 6.2) is focused by a f = 20 cm lens. A ~100 μm diameter ink dot printed on transparency is placed precisely at the focus of the probe beam to block the unperturbed light forming a dark-field Schlieren image. Therefore, in the absence of a plasma to refract some of the probe beam rays, the entire probe beam is blocked from reaching the CCD camera, hence the name 'dark-field'. However, probe rays that are refracted by the plasma will follow a different trajectory around the 100 μm ink dot and form an image on the camera. This beam block was chosen, as opposed to more traditional knife-edge blocks [109], because it is sensitive to plasma density gradients in both transverse directions.

An example Schlieren image (a) along with the corresponding interferogram (b) are shown in Fig. 6.5 for a single 100 ps (FWHM) 10 μm laser pulse containing 50 J, taken at a probe timing near the peak of the CO_2 laser pulse. The peak plasma density is $4n_{cr}$ therefore the ponderomotive force of the laser is expected to push the plasma forward (to the left in the figure) and outwards forming a plasma wall as seen. The magnification of the Schlieren system gives a field of view of 3 x 4 mm which not only provides an independent indication of the plasma profile but displays its relative position to the gas jet. In some cases, the Schlieren image can also provide additional information not seen in the interferogram, such as a view of the entire plasma if parts of it are not contained within the limited field of view of the interferogram. In this particular shot, the Schlieren image shows a long density gradient indicating a falling density profile on the back side of the plasma wall ($\sim$1500-1800 μm on the Schlieren horizontal axis) where the interferogram's information has been blurred.

6.4 Conclusion

Presented here is the main diagnostic for probing the laser plasma interaction : interferometry. Through phase retrieval of an interferogram and Abel inversion, the 2D plasma density profile is obtained with a temporal resolution of 2 ps, the width of the probe pulse. The probe pulse is crosscorrelated at the IP with the CO_2 macropulse using semiconductor switching technique to obtain a synchronization accuracy of $\pm$20 ps. In addition to interferometry, a the same probe pulse is split and used to obtain a Schlieren image of the laser-plasma interaction for the purposes of a wider field of view as well as a confirmation of dynamics that are observed in the interferometry.

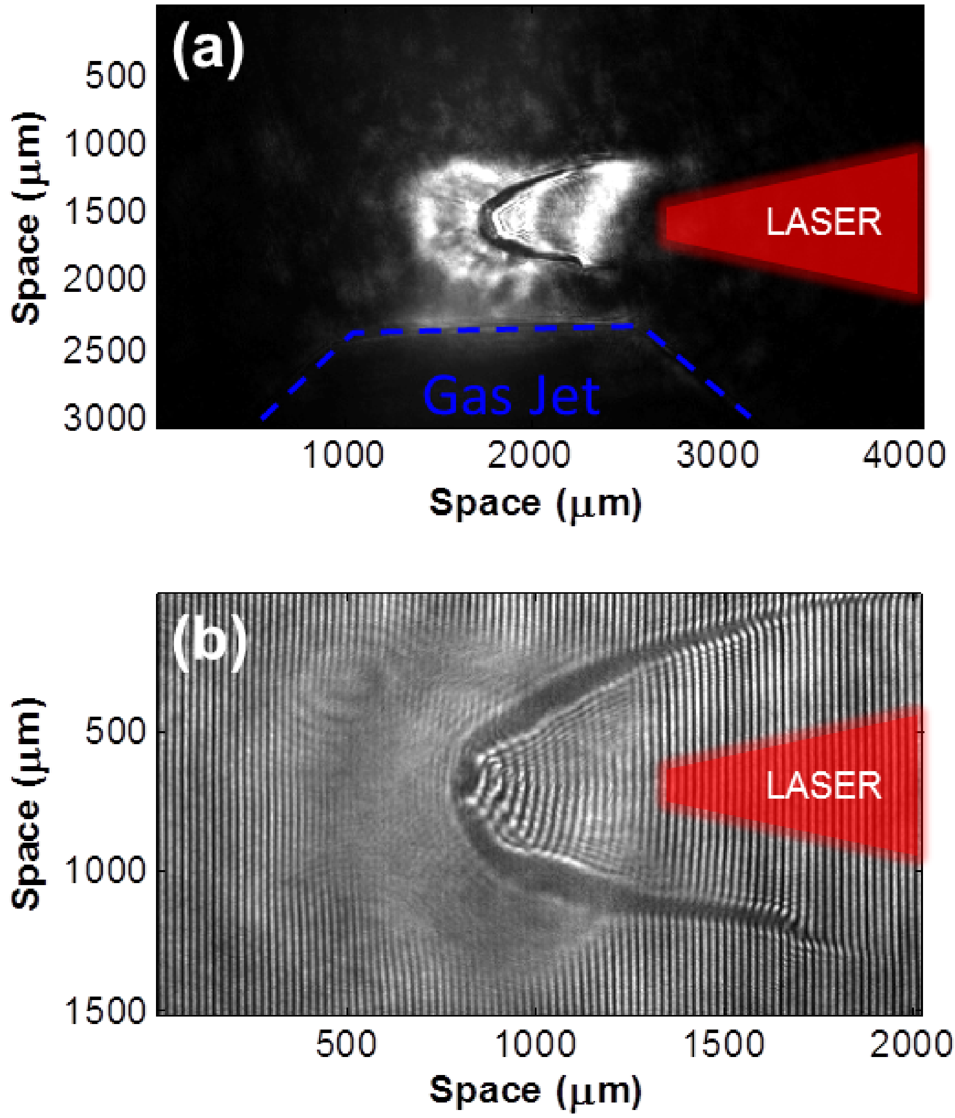

Figure 6.5: Images obtained on a single laser shot from the Schlieren (a) and interferometry (b) diagnostics. These were obtained for a single 100 ps (FWHM) 10 μm pulse containing 50 J of energy incident upon the gas jet with a peak initial plasma density of $4n_{cr}$ ($4\text{x}10^{19}$ cm^{-3}). The probe pulse was timed near the peak of the CO_2 laser pulse.

CHAPTER 7

Shock Wave Acceleration of Protons in Hydrogen Gas

7.1 Introduction

SWA of ions in solid-state targets was proposed first by Denavit [67] via 1D simulations and elaborated on by Silva et. al [68] using 2D simulations. However, the energy spread of the accelerated ions was increased significantly by the strong sheath fields that exist on the back side of the plasma. These fields, which are responsible for the acceleration of ions in the TNSA mechanism, are inversely proportional to the plasma scale length [42] which is very short for a solid density plasma target.In addition, the interaction of the laser pulse with a 100n_{cr} plasma is inefficient requiring laser pulses with peak a_o's of 10 to significantly heat the electrons.

In this chapter experimental realization of SWA of monoenergetic proton beams by the interaction of a picosecond CO_2 laser pulse with a H_2 gas jet is discussed. Proton beams with a narrow spectrum were produced for the first time by deploying a long density scale-length plasma that can exist on the back side of an overdense gas jet target. Here in this long exponentially decaying plasma profile, the sheath field is expected to be small and constant allowing for the protons to sustain their energy spread as they exit the plasma. Because the gas jet target is tuned to a plasma density that is near the critical density of 10^{19} cm^{-3} for the 10 μm radiation, efficient heating of plasma electrons occurs in the region leading up to the critical density at a relatively modest laser field strength of a_o ~ 2. This heating along with a significant increase to the hole boring velocity (per Eq.

2.5) at near critical peak plasma densities are key conditions for producing a shock which travels at a high velocity leading to a favorable scaling for SWA protons.

7.2 Accelerated Proton Spectra and Emittance

The following experimental results were obtained using the experimental setup described in Chapter 5 involving the interaction of the high power CO_2 laser (described in Chapter 4) with the H_2 gas jet. Protons accelerated from this interaction are recorded in the CR-39 stacks. After each laser shot, the five CR-39's are etched in 6N NaOH solution at 80°C for five hours to uncover proton pits near the edges of each CR-39. Near the peak of the proton spectrum, additional etching in five hour increments is performed to obtain a finer spectral resolution. After each etching period, the CR-39's were observed under a microscope with 5 μm resolution and the etched pits were counted by an in-house computer software program written in Matlab [114]. A detailed description of the processing and analysis of exposed CR-39's can be found in Appendix B.

The resulting proton spectra obtained throughout the course of the LDIA experiment are compiled in Fig. 7.1. The complete spectrum of the protons obtained for a smooth 100 ps laser pulse ($a_o \sim 0.3$) and a laser macropulse (peak micropulse $a_o \sim 2$) containing the same energy are plotted in Fig. 7.1a. The peak plasma densities for these shots is $4n_{cr}$. For the smooth pulse the proton spectrum is monotonically decreasing, whereas for the macropulse there is a well-defined peak centered around 18 MeV with an energy spread $\Delta E/E_{FWHM} \sim 1$ %. The central energy of this peak varied depending on the structure of the laser macropulse (number and peak a_o of micropulses). An example of four shots all showing a narrow energy spread but energies varying between 15-22 MeV is shown in Fig. 7.1b obtained with different macropulse structures (number of pulses and a_o values ranging from 1.5 to 2.5). The transfer of laser energy to the protons within the monoenergetic peaks reaches 10^{-6} %.

In Fig. 7.2 we show an image of the expanding proton beam seen on the fourth 1

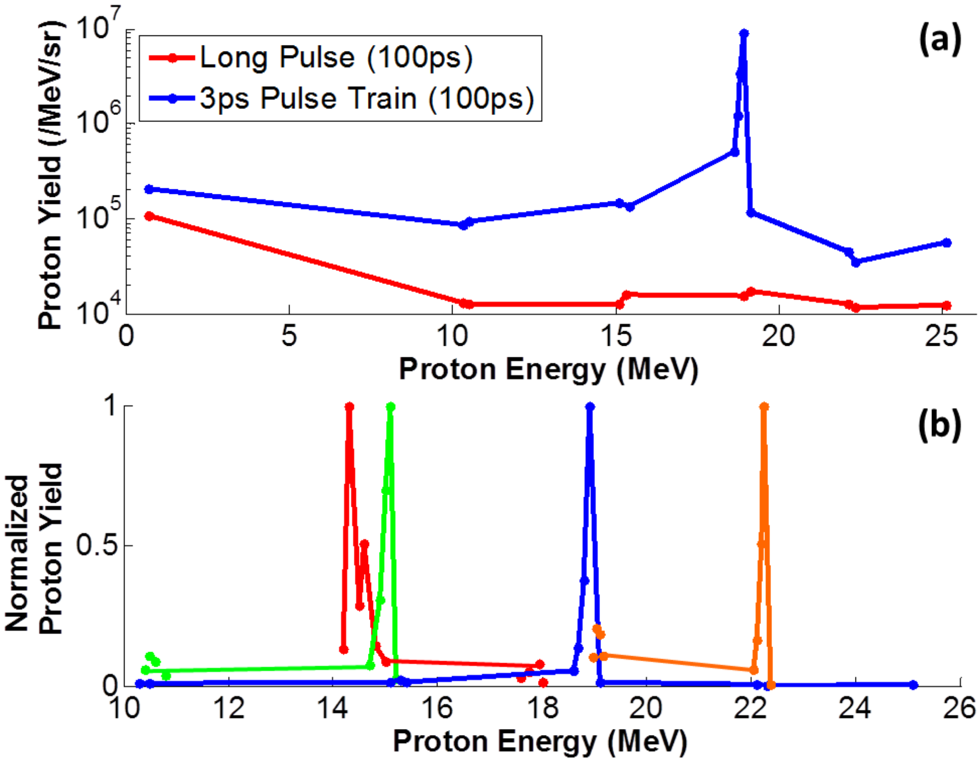

Figure 7.1: Proton spectra obtained with a 100 ps long laser pulse (red) and a 100 ps macropulse consisting of a number of 3 ps micropulses (blue) both containing 50 J (a). The typical noise level on a single CR-39 detector was 200 pits. The total number of protons contained within the monoenergetic peak was 2.5×10^5. The details of the energy spectra on four different laser shots with different macropulse structures (number of pulses and a_o's ranging from 1.5-2.5) (b).

mm CR-39 detector with a nominal energy of 22 MeV. This beam is contained within a solid angle that is an order of magnitude smaller than that subtended by the laser beam. The transverse spatial profile of the proton beam appears to be correlated to that of the incident laser beam at the point of reflection from the plasma. A measurement of the CO_2 laser beam profile in vacuum for this focusing condition uncovered a strong astigmatism of the laser beam (see Fig. 5.2, which is then apparently transferred to the accelerated proton beam. Assuming an initial source size equal to the laser spot size (60 μm), we have estimated the geometric emittances of this beam to be $\varepsilon_x = \theta_x w_o = 1.1$

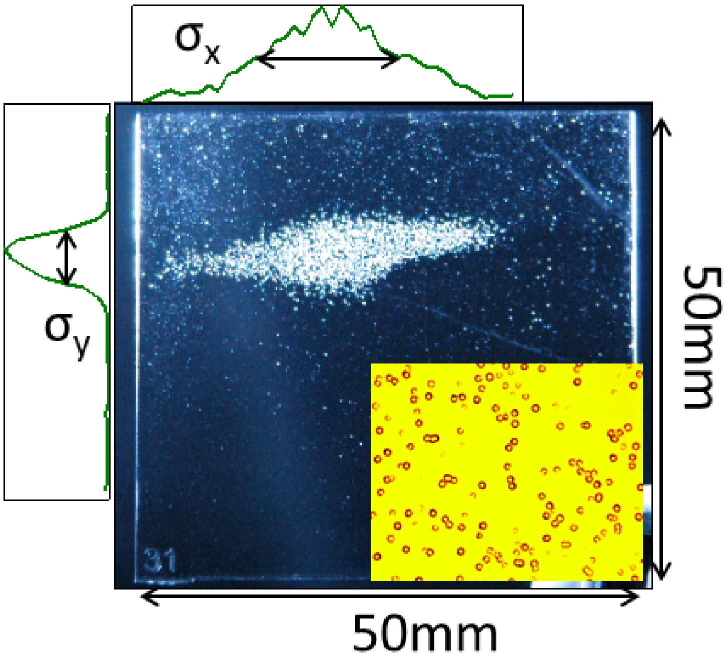

Figure 7.2: An image of the 22 MeV proton beam on the fourth CR-39 detector. The inset shows a magnified portion of the CR-39 indicating no significant overlap of individual proton tracks. σ_x = 5.7 mm and σ_y = 2.2 mm are the FWHM dimensions of the proton beam in the x and y directions respectively.

mm·mrad by ε_y = 0.4 mm·mrad, where $\theta_{x,y}$ is the half-angle divergence of the proton beam in the x or y direction. This corresponds to normalized emittances of $\varepsilon_{n,x} = \varepsilon_x \beta\gamma$ = 250 μm·mrad by $\varepsilon_{n,y}$ = 90 μm·mrad. By scanning the focal position more symmetric (albeit larger) emittance proton beams were obtained. The typical geometric emittances were ~5 mm·mrad.

7.3 Diagnosing the Laser-Plasma Interaction

The laser-plasma interaction was diagnosed to first order by monitoring the laser transmission through and reflection from the plasma with standard energy meters. With the ability to scan the gas jet density from below to above n_{cr} for 10 μm light, the plasma target can be set to be transparent or opaque to 10 μm radiation. This can be seen in a plot of the transmission and reflection versus the initial peak plasma density (assuming full ionization of the neutral gas) as seen in Fig 7.3a and 7.3b, respectively. For a peak initial plasma density of $n_p < 2\mathrm{n}_{cr}$, there is a pure underdense interaction characterized by minimal reflection and maximum transmission (and visa versa in the overdense case of $n_p > 2\mathrm{n}_{cr}$). This abnormal transmission above n_{cr} is mainly attributed to rapid plasma expansion during the long 100-200 ps interaction after early micropulses which reach 10^{14} W/cm^2 begin to ionize the target. The expansion can decrease the peak plasma density to n_{cr} or below leading to the transmission of a large fraction of the macropulse depending on the initial peak plasma density. Another contributing factor, though to a much lesser degree, that can aid in the transmission of the CO_2 laser pulses is the relativistic increase in n_{cr} for the peak micropulses. As the plasma electrons oscillate in the relativistic laser field, their mass increases causing an effective decrease to ω_p, and therefore an increase in n_{cr} by a factor of $\sqrt{1+a_o^2}$ [42]. For the peak micropulses with an $\mathrm{a}_o \sim 2.5$, the effective n_{cr} is 2.7x10^{19} cm^{-3} leading to partial transmission of the macropulse.

To further uncover these dynamics of the plasma density profile, we take advantage of the temporal resolution of picosecond interferometry as opposed to the time integrated reflection and transmission diagnostics. An example of two interferograms obtained with an initial peak plasma density of $4\mathrm{n}_{cr}$ at different probe times are seen in Fig. 7.4. The dotted yellow line represents the center of the gas jet where the peak neutral gas density is 4x10^{19} cm^{-3}; therefore, the initial position of the critical surface where $\mathrm{n}_p = 10^{19}$ cm^{-3} is $\sim$600 μm to the right of this line (see gas jet density profile in Fig. 6.4). The interferogram in Fig. 7.4a is a snapshot of the plasma density profile approximately 30 ps before the peak of the 10 μm macropulse where qualitatively one can see that the laser has pushed the critical surface all the way to the center of the gas jet boring a parabolic shaped hole or cavity. Unfortunately, strong refraction of the probe light near the walls of the cavity complicates a quantitative analysis of these interferograms, and in this case makes it impossible. However, to the left of the overcritical surface, the plasma density on axis (y = 0 μm) can be estimated using Eq. 6.6 assuming the upstream plasma profile as

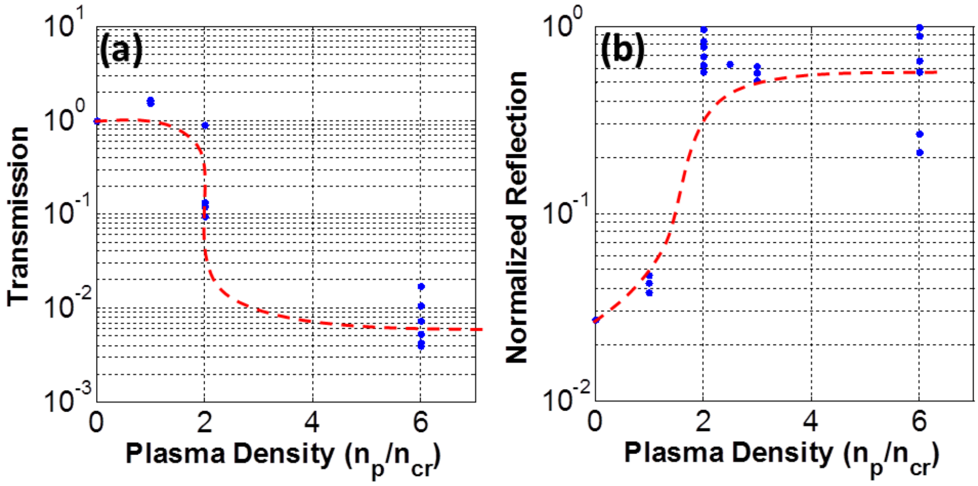

Figure 7.3: CO_2 laser transmission through (a) and reflection from (b) the plasma target plotted versus the initial peak plasma density. Full ionization of the neutral H_2 gas particles is assumed since the peak laser intensity (10^{16} W/cm^2) is more than 100 times larger than the H_2 ionization intensity of 10^{14} W/cm^2. Both measurements are normalized to a laser shot without the plasma (in vacuum) and the density is normalized to n_{cr} for 10 μm light.

Gaussian. Here from left to right, the plasma density on axis is seen to increase reaching $\sim$2.7x10^{19} cm^{-3} at the last measureable fringe (x = -150 μm), and is expected to continue to increase to its peak within the palsma wall (close to the initial 4n_{cr}).

The interferogram in Fig. 7.4b is a snapshot of the plasma density profile $\sim$100 ps later, or 70 ps after the peak of the macropulse. The peak plasma density is taken to be at x = -475 μm where the direction of the fringe shift changes from bending to the left (increasing plasma density) to bending to the right (decreasing plasma density). Here, Eq. 6.6 can again be applied assuming a Gaussian profile just to the left of where the plasma wall complicates the estimation, resulting in a plasma density on axis of $\sim$1.4x10^{19} cm^{-3}. Not only has the laser continued to bore a hole through the plasma pushing the critical surface towards the back side of the initial gas profile, but due to continuous plasma expansion the peak density has dropped to almost n_{cr}. Eventually the peak plasma density will drop

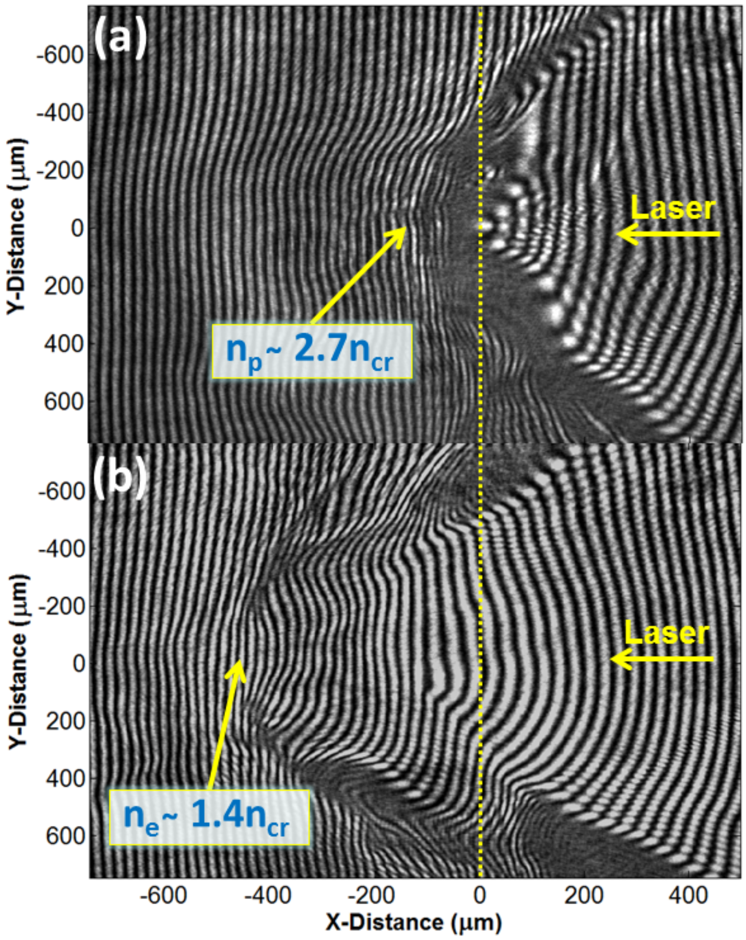

Figure 7.4: Interferograms taken at a probe timing of 30 ps before (a) and 70 ps after (b) the peak of the macropulse. The peak initial plasma density was 4x10^{19} cm^{-3}, or 4n_{cr}, and its original position is denoted by the yellow dotted line. The densities n_p noted on the interferograms are obtained using Eq. 6.6 assuming a Gaussian transverse profile at the last measurable fringe from the left side.

below n_{cr} leading to the transmission of part of the macropulse. This change from opaque to transparent will occur earlier for a lower initial peak plasma density contributing to the dynamics seen in the transmission curve in Fig. 7.3a.

The hole boring velocity, v_{hb}, averaged over multiple micropulses can be extracted from the position of the overdense plasma layer seen in the interferograms of Fig. 7.4. The plasma wall is seen to move ∼450 μm in ∼100 ps, or at a velocity of 0.015c. An upper end of this velocity at the peak of a laser pulse can be obtained using Eq. 2.5 which results in $v_{hb} = 0.041c$ using $a_o = 2.5$ and $n_p = 2n_{cr}$ (reduced from its initial value of $4n_{cr}$ due to expansion). It is not surprising that the measured average hole boring velocity is almost a factor of 2.6 smaller than the peak v_{hb} since the plasma is only accelerated forward during the 3 ps laser pulse whereas it coasts and even decelerates during the 18 ps between the micropulses. It is possible for the potential inherent in the hole boring process to reflect protons to twice the hole boring velocity [53, 54]. Cold plasma protons that reflect off this moving layer would gain a maximum energy of $1/2M_i(2v_{hb})^2 \approx 100$ keV (experiment) or 800 keV (theory), which represents an upper bound by assuming that the upstream ions are stationary before reflection. These values are more than an order of magnitude smaller than the proton energies observed in the experiment (see Fig. 7.1), therefore pointing to a much faster moving potential which can be provided by a shock wave.

Successful proton acceleration was empirically found for peak initial densities of 3-$5n_{cr}$ where the entire CO_2 laser macropulse is stopped in the gas jet. Therefore it is of interest to carefully analyze the plasma density profile in this density range just before the peak micropulses arrive and presumably lend the largest contribution to the proton acceleration process. One such interferogram obtained ∼15 ps before the peak of the macropulse is shown in Fig. 7.5a. The initial neutral gas density profile is plotted below it (Fig. 7.5b) in blue reaching a peak density of 3.8×10^{19} cm^{-3}. Again it is evident that the laser is boring a hole through the plasma creating a parabolic shaped plasma wall. Some of the information has been lost near the plasma wall, therefore a manual analysis of the interferogram has been performed to abstract the on-axis ($y = 0$ μm) plasma density profile. A detailed description of this method can be found in Appendix C. The resultant plasma profile is plotted in red in Fig. 7.5b which is vastly different from the initial gas jet profile. On the laser side, the profile has been strongly steepened by the ponderomotive force of the laser forming a sharp ($< 10\lambda$) rise to an overcritical surface. Though the laser hasn't reached the back side of the gas jet, cold electrons accelerated by the early micropulses ($a_o << 1$) collisionally ionize the H_2 atoms forming a millimeter scale length plasma. As this plasma expands, the plasma density on the rear of the target drops rapidly to generate an exponentially falling density profile.

Additional support for the extracted plasma profile is gained through comparison to a simulated interferogram using a 3D parabaloid plasma. The longitudinal profile used for the 3D model plasma closely resembles the measured plasma profile (black dashed and solid red lines in Fig. 7.5b, respectively). The mathematical method used to create the synthetic interferogram from this 3D plasma model is described in Appendix C. Fig. 7.5c displays the resultant simulated interferogram which contains the same basic features as that experimentally obtained in Fig. 7.5a. Specifically note the change in curvature of the fringes on the front side of the profile (x = 0 μm) which is indicative of a change in the derivative of the plasma density. First, the fringes on the back side of the gas jet have a slowly increasing shift indicative of the long exponentially decreasing plasma density profile. At x = 0, the strong change in curvature of the fringes indicates the passing of the peak plasma density and rapid decline to low densities.

This dynamically formed plasma density profile with a fast rise to an overcritical surface (stopping the incident laser pulse) followed by a long exponential tail is key to the understanding of the proton acceleration process. Its formation is a product of the long interaction of the 100-200 ps macropulse with a mildly overcritical plasma source which allows for laser hole boring on the front side and plasma expansion on the rear side of the gas jet. An equivalent scenario using the more common 1 μm (Nd:Glass) or 800 nm (Ti:Sapph) high power laser systems could involve a prepulse exploding a foil target with a certain predetermined delay for the main pulse to obtain a similar initial plasma density profile. However, this plasma density profile is thus far unique to the interaction of a high power 10 μm pulse with a gas jet target [60].

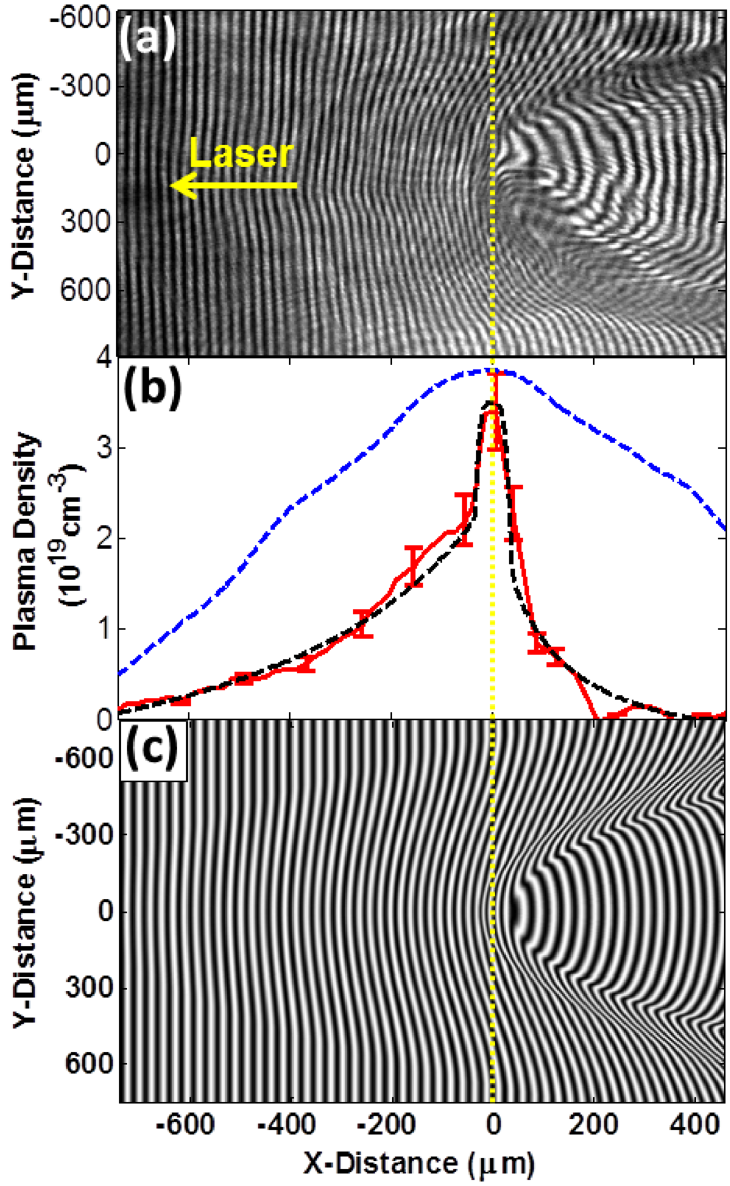

Figure 7.5: a) Interferogram of the plasma taken at the peak of the CO_2 laser macropulse showing the hole bored into the plasma by the laser pulse. b) The initial gas jet density profile (dotted-blue), the plasma density profile extracted from the interferogram in (a) (solid-red), and the simulated plasma density profile (dashed-black). c) Simulated interferogram using a 3D parabaloid plasma with a longitudinal profile shown in the black dashed line in (b).

7.4 Proton Yield and Laser Plasma Instabilities

The maximum yield obtained within the monoenergetic proton beam is 2.5x10^5 particles. This yield is the limiting factor in the applicability of these proton beams in their current state, not only as a single shot source but also as a high repetition rate source at 100-1000 kHz. We believe this not to be a fundamental limitation of the acceleration of protons in a H_2 gas jet by a CO_2 laser as other recent results indicate that this interaction can produce up to 10^{12} protons per shot [53, 54]. In order to increase the yield in future experiments, one must optimize the experimental parameters. From the limited parameter space investigated in the current experiment, there are indications that underdense laser plasma instabilities (LPI) can play a role in inhibiting the formation of a quasi-1D shock wave optimal for proton acceleration.

Laser self-focusing, laser filamentation, and electron filamentation are examples of processes that can strongly change the target geometry and may affect the proton acceleration process. Laser self-focusing and filamentation can occur in the long underdense plasma leading up to the critical plasma density where the peak laser power (4TW) can be up to 100 times greater than the critical power for self-focusing : $P_{cr} = 17(n_{cr}/n_p)$ GW. Though these processes were not directly observed in the interferometry or schlieren images, indirect evidence of them can be inferred from the transmission curve seen in Fig. 7.3a. The transmission energy meter has a diameter of 1" and so samples ~6% of the 4" diameter 10μm laser beam, therefore the measurement is sensitive to the focusing geometry of the laser beam. Data points at $n_p = n_{cr}$ which lay above 100% transmission (no plasma) indicate a strong change in the focusing or propagation direction of the CO_2 laser pulse hinting towards the existence of the aforementioned processes.

In addition to laser filamentation, the breakup of an electron beam into filaments can also occur as the beam travels through a background plasma. This has been observed in laser plasma experiments where electrons accelerated from a solid density target irradiated by a laser pulse are seen to filament in the lower density plasma on the back side of the

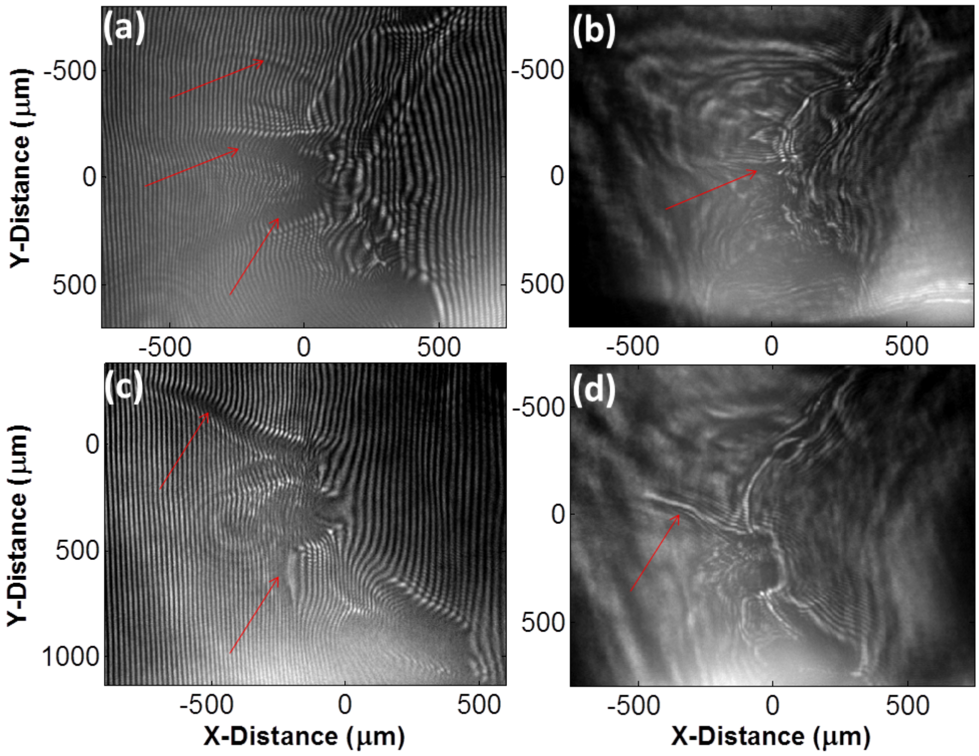

Figure 7.6: Electron filamentation as observed in interferograms (a and c) and the corresponding Schlieren images (b and d) for an initial peak plasma density of $n_p = 6n_{cr}$ (a and b) and $n_p = 5n_{cr}$ (c and d). The position of the initial peak plasma density occurs at x = 0.

target [115, 116]. Simulations show that initial filament widths are on the order of the plasma period (c/ω_p) but can merge into much larger scale filaments as they propagate [117]. Electron filaments were observed in the LDIA experiment through interferometry and schlieren images as shown in the two examples in Fig. 7.6. The interferogram and schlieren images of two shots are shown where the peak initial density of the plasma was $6n_{cr}$ (Fig. 7.6a and 7.6b) and $5n_{cr}$ (Fig. 7.6c and 7.6d). The laser pulse is seen to be penetrating into the plasma from the right but is stopped near the peak of the gas jet density profile (x = 0). Electrons accelerated by the laser penetrate the overdense plasma and are seen to form filamentary structures, some of which are denoted by red arrows in the figure. It is interesting to note that the filament widths which lay in the range of

25-200 μm are much larger than $c/\omega_p \sim 1$ μm. Filaments on the order of c/ω_p are not observable since they are smaller than the 20 μm resolution of the image; nonetheless, they have appeared to coalesce into large filaments rather quickly in front of the laser pulse. Though no direct correlation can be made between shots producing filaments and shots producing protons, the vast majority of the electron filamentation observed in the experiment occurred on shots with peak plasma densities at or above $5n_{cr}$.

Possible evidence for LPI's affecting the proton acceleration process can be gained through the longitudinal scan of the laser focus through the gas jet. The most optimal focal position, based on the production of a significant amount of protons, was found to be 500-1000 μm in front of the gas jet. In this case, the laser beam is slightly diverging when interacting with the overdense plasma layer as opposed to a converging beam in the case of focusing in the middle or behind the gas jet. The wavefront curvature of this diverging laser beam could possibly compensate for the effect of self-focusing which can lead to filamentation of the laser beam and therefore provide for a more planar interaction with the overdense plasma. These different focal positions also produced differently shaped proton beams as the transverse profile of the proton beam appears to be correlated with that of the laser beam incident upon the overdense surface. This can be seen in Fig. 7.7 which shows the CO_2 laser beam profiles of two different focusing conditions. Fig. 7.7a and 7.7b correspond to focusing 750 μm in front of the gas jet placing the CO_2 laser focus (Fig. 7.7a) directly on the initial position of the overdense plasma surface and the proton beam produced is shown in Fig. 7.7b. However, one proton beam was obtained while focusing 500 μm behind the gas jet where now the converging part of the CO_2 laser beam is incident upon the overdense plasma layer. Due to the residual astigmatism in the focus of the OAP (see Fig. 5.2), the laser beam has an horizontal oval shape as shown in Fig. 7.7a and produced a similarly shaped proton beam shown in Fig. 7.7b.

Though there are some signs of a deleterious effect of the aforementioned processes on the SWA process, one must consider the time scales involved. The result of laser self focusing, laser filamentation, and electron filamentation can be the production of a very

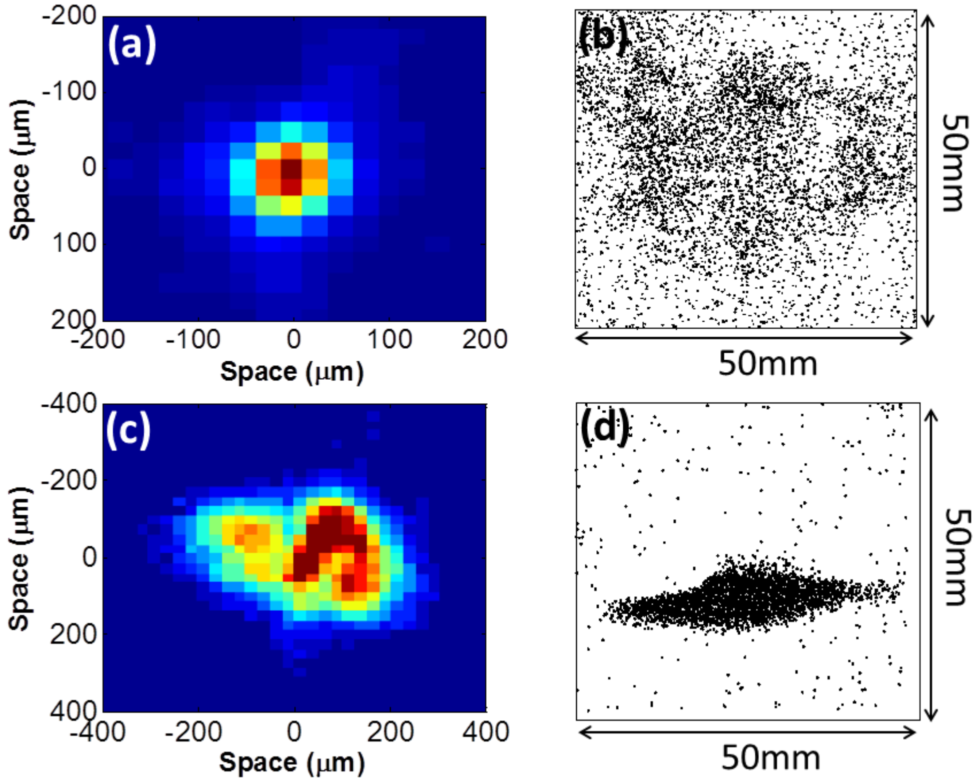

Figure 7.7: Measurement of the laser beam profile that is incident upon the critical plasma density surface when focusing 750 μm in front of the gas jet (a) and 500 μm after the gas jet (c). The corresponding accelerated proton beams as observed on the CR-39 detectors are shown in (b) and (d).

inhomogeneous population of hot electrons. However, these electrons are expected to recirculate and therefore homogenize the distribution on a time scale of $\sim L_p/v_{the}$, where L_p is the length scale of the plasma and v_{the} is the thermal velocity of the electrons. For T_e = 1 MeV, v_{the} = 0.9c, therefore the recirculation time scale (1 mm / 0.9c $\sim$ 3 ps) is much shorter than that for the shock dynamics which are dominated by the protons which move on a time scale of $\sim L_p/C_s$. Therefore, conclusive knowledge of effect of these processes on the formation of a shock wave and subsequent acceleration of protons would require additional simulational and experimental effort.

One last controllable parameter that was investigated in the LDIA experiment was the initial peak plasma density which is easily scanned by changing the pressure of the gas at the nozzle. As previously stated, the optimal range of peak initial densities were in the 3-5 n_{cr} range. Below this density range, the combination of hole boring and expansion caused the plasma to become transparent early on in the macropulse as indicated by the change in the transmission/reflection curves seen in Fig. 7.3. In this range of gas jet densities, the plasma density profile observed in the interferograms and Schlieren images never formed a sharp overcritical layer as seen in Fig. 7.5a, therefore the peak laser pulses are not able to push the overcritical surface into the bulk plasma causing the formation of a shock wave (see further description below). When the gas jet density was set above the optimal range, the entire laser pulse was stopped near the front end of the gas jet leaving behind a thick dense plasma. In this case it is speculated that the strong positive density gradient on the front side of the gas jet profile will inhibit the formation (as well as propagation) of a shock wave since it acts to minimize the density drop on the upstream side. This is compared to the optimal range of densities where a shock is formed near the peak of the gas jet density profile and therefore the upstream density is exponentially falling. Additionally, in this range of densities both interferograms and shadowgrams often showed strong filamentation as mentioned earlier.

7.5 2D OSIRIS Simulations of Laser-Driven Shock Wave Acceleration of Protons

SWA of protons is elucidated using the 2D particle-in-cell code OSIRIS [72] and was carried out by Frederico Fiuza. For the practical purpose of reducing simulation time, only the interaction of the two peak micropulses with a preformed plasma is simulated. The plasma is initialized cold ($T_e = T_i = 0$) and has a density profile modeled after the measured plasma density profile (shown in Fig. 7.5b red line) with a 10λ linear rise to $2.5n_{cr}$ and exponential fall with a characteristic length of 30λ. Two linearly polarized 3 ps long micropulses with an a_o of 2.5 and separation of 18 ps are incident upon this

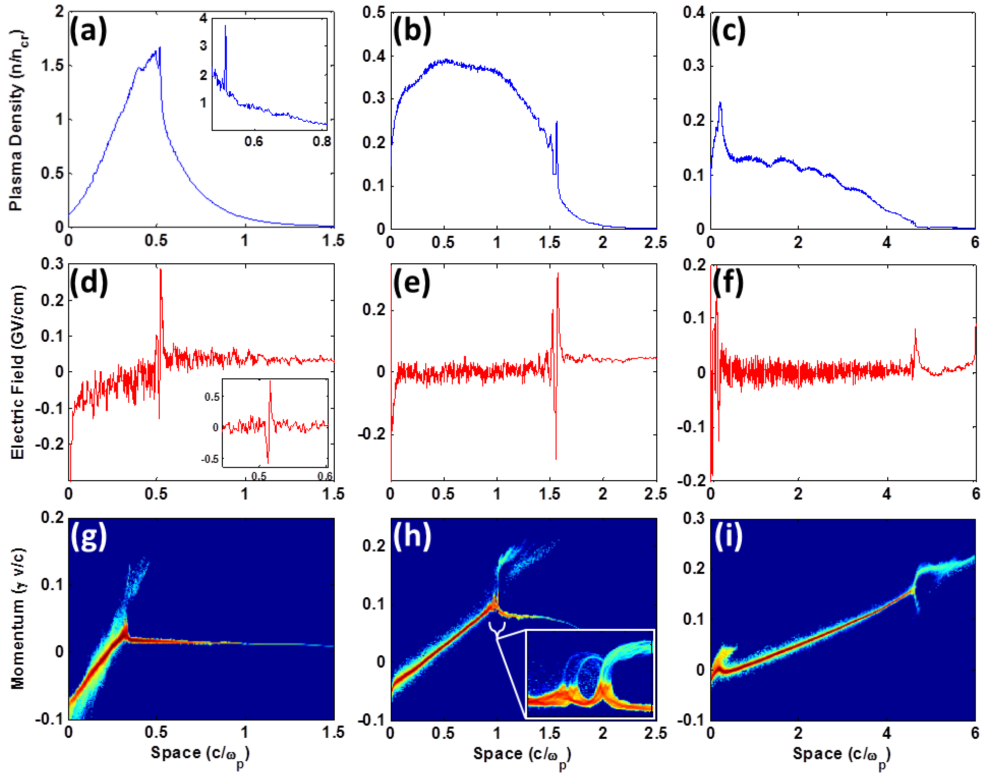

Figure 7.8: Results of a 2D OSIRIS simulation modeling two 3 ps CO_2 pulses separated by 18 ps with a peak a_o of 2.5 incident upon a plasma with a 10λ rise to 2.5n_{cr} and and exponential fall with a characteristic length of 30λ. The average proton density (a-c), average longitudinal electric field (d-f), and proton phase space (h-i) are plotted versus space for the times of 17 ps (a,d,h), 52 ps (b,e,h), and 122 ps (c,f,i). The times of arrival for the two laser pulses are 7 ps and 25 ps, respectively.

plasma. A summary of the results of the simulation is seen in Fig. 7.8 where the average proton density (a-c), average longitudinal electric field (d-f) and proton phase space (h-i) are plotted versus space for the times of 17 ps (a,d,h), 52 ps (b,e,h), and 122 ps (c,f,i). The first laser pulse is incident upon the plasma at 7 ps and is absorbed near the critical density, heating up the plasma causing its expansion. The laser pulse also drives the critical surface forward at the hole boring velocity causing a build up of the ion density in a spike. These two conditions of having counterstreaming plasmas and a density discontinuity have both been shown to facilitate the formation of a collisionless shock wave in Chapter 2. At 17 ps (Fig. 7.8a,d,h) the shock is seen as a discontinuity in the proton density and phase space and as a characteristic spike in the longitudinal electric field. Averaging over the 2D transverse plane results in a weaker discontinuity due to some inhomogeneity that develops across the plasma. This can be seen in the insert in Fig. 7.8a which is a zoomed picture of a lineout of the proton density. Here, a spike up to 3.5n_{cr} is observed as compared to the peak density of 1.5n_{cr} in the averaged density. This effect is also seen in the electric field where a stronger density discontinuity results in a larger electric field as shown in the zoomed picture picture in Fig. 7.8b which contains the corresponding lineout of the electric field which peaks at 0.7 GV/cm instead of the averaged field of 0.3 GV/cm.

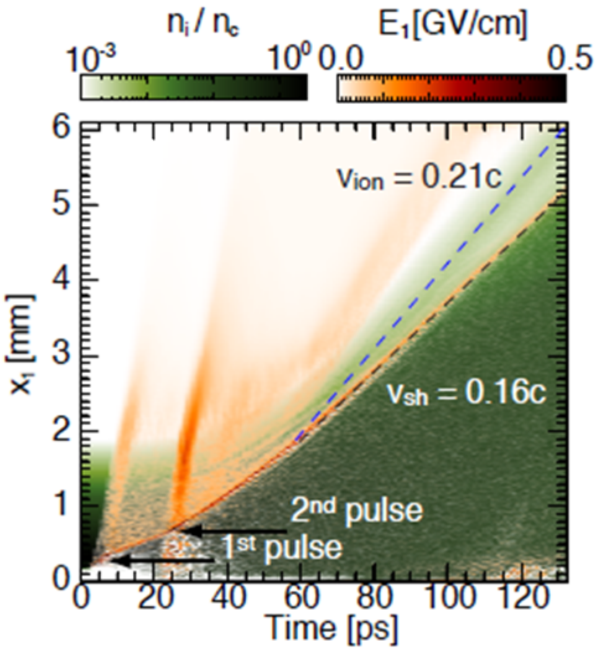

Figure 7.9: Results of a 2D OSIRIS simulation modeling two 3 ps CO_2 pulses separated by 18 ps with a peak a_o of 2.5 incident upon a plasma with a 10λ rise to 2.5n_{cr} and and exponential fall with a characteristic length of 30λ. Here, the average proton density (green) and electric field (orange) are plotted versus space and time.

When the second laser pulse arrives at 25 ps, the peak density is near the critical density due to plasma expansion and therefore the electrons are efficiently heated and the hole boring velocity is increased (see Eq. 2.5). The electrons are heated to a temperature of ~1.1 MeV which is is consistent with the ponderomotive scaling for the hot electrons, $T_{hot} = m_e c^2 \sqrt{1 + a_o^2/2} = 1.04$ MeV. These effects both help to increase the speed of the shock as observed in Fig. 7.9 displaying the density and electric field (shown in green and orange, respectively), versus time and space. After the arrival of the second laser pulse, the shock speed increases to $V_{sh} = 0.16c$ and remains constant. The shock dissipation is provided by proton reflection and proton trapping/heating in the trailing ion acoustic wave as seen in the proton phase spaces in Fig. 7.8h and i. Due to the long exponentially decaying plasma profile, the TNSA field is small and constant (Fig. 7.8d and e) and therefore the protons are expanding at a slow and constant velocity of <0.1c. As the shock passes, it reflects an average of 0.5% of the protons to a velocity $V_{refl} = 2V_{sh} - V_{up} = 0.21c$, or ~21 MeV, an energy in reasonable agreement with the experimentally measured values. Due to the cold expansion and constant shock velocity, the reflected protons are contained within a narrow energy spread of $\Delta E/E_{FWHM} \sim 12\%$. This beam of protons is seen leaving the plasma in Fig. 7.8i retaining its energy spread due to the lack of a TNSA field at the edge. It should be noted that when the laser a_o was reduced to 2, the peak proton energy dropped to 15 MeV, a variation of energy consistent with that observed in the experiment (Fig. 7.1b).

It is of great interest to study the potential of SWA protons to reach energies in the range 100-300 MeV/a.m.u. required for medical applications [35, 36]. For this purpose, similar simulations were performed using a single 10 ps laser pulse with varying intensities (a_o = 2.5 - 20) incident upon the same plasma profile but with increased peak plasma densities (n/n_c = 2.5-10) in order to compensate for relativistic transparency [42]. In each case, a shock was observed to reflect protons with a narrow energy spread as shown by their spectra plotted in Fig. 7.10a. The increase of the reflected proton energy with the laser a_o is shown in Fig. 7.10b which illustrates that the proton energy scales approximately as $a_o^{3/2}$, allowing for the generation of ~200 MeV proton beams with 100 TW class laser system ($a_o = 10$).

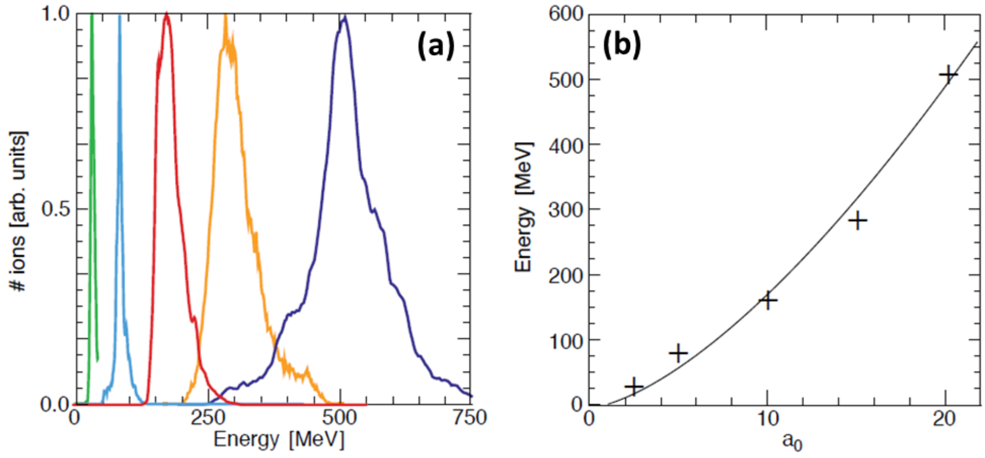

Figure 7.10: Final spectra of the proton beams reflected by a shock generated by a 10 ps laser pulse with a normalized vector potential, a_o, of 2.5 (green), 5 (light blue), 10 (red), 15 (orange), and 20 (dark blue). The obtained peak energies are 31, 79, 165, 287, and 512 MeV, with corresponding energy spreads ranging from 10% to 25%. b) Scaling of proton energy with laser amplitude. The simulation points (+) are well fitted to E[MeV] $= 5.6a_o^{3/2}$ (solid line).

7.6 Conclusion

Here we have shown that the interaction of a high power CO_2 laser macropulse consisting of 3 ps micropulses separated by 18 ps with a mildly overcritical gas jet plasma can launch a shock wave capable of accelerating protons to high energies. Protons are detected by stacks of CR-39 nuclear track detectors where energies up to 20 MeV, energy spreads down to $\Delta E/E$ of 1%, and geometrical emittance as low as ~mm·mrad are measured. 2D OSIRIS simulations elucidate the shock wave formation and propagation through the rear side of the gas jet where the long exponential plasma profile results in a slow and constant expansion. As the shock wave, traveling at a constant velocity of 0.16c, passes these expanding protons, they are reflected into a monoenergetic beam.

These results are compared to the trend of LDIA proton energies plotted in Fig. 1.1 where it is clear that 20 MeV protons accelerated by a 4 TW laser show the superior scaling of SWA protons to those of TNSA and RPA. Furthermore, the majority of the accelerated protons are contained within an energy spread of $\sim$1% which is a factor of 10 times smaller than the most narrow LDIA ion beam [53, 54] reported to date. The small spatial extent of the source (laser spot size) as well as the rapid acceleration by the fast propagating shock wave provides a picosecond-scale pulse of protons with geometric emittances down to a mm·mrad. 2D simulations show the potential of this acceleration mechanism to achieve 100's of MeV/u ions with current laser 100 TW laser systems. Aside from a potential application in areas needing a high energy source of ions with a narrow energy spread such as cancer radiotherapy [35, 36], these beam qualities are beneficial to the control and further acceleration of the protons by external magnets and RF cavities where typical ion injectors produce 1-100 ns long pulses of ions with large energy spreads. Finally, a gas jet plasma source has the capability to provide many species of ions for various applications such as helium, carbon, nitrogen, oxygen, neon, argon, zenon etc.

CHAPTER 8

Conclusion

In this dissertation, it is shown that laser-driven collisionless electrostatic shock waves can produce high quality proton beams far exceeding the energy versus laser power scaling of current LDIA results and with an order of magnitude improvement in the energy spread ($\Delta E/E \sim 1\%$). The LDIA field seeks to deliver compact and affordable sources of high energy ions with narrow energy spreads as an alternative to conventional radio-frequency accelerators. The most demanding application of hadron cancer therapy necessitates ion energies on the order of 100-200 MeV/a.m.u. and energy spreads of less than 5%, thus far exceeding the results of LDIA experiments using the most powerful lasers available. From this first demonstration of laser driven SWA of protons, a promising path is laid towards meeting the application driven demands of LDIA ion beams.

The basic physics of shock wave formation, propagation, plasma heating, and proton reflection is studied via 1D OSIRIS simulations for the interaction of two semi-infinite plasmas (with no laser). It was shown that a shock can form from either the expansion of one dense plasma into a more rarefied one or by colliding plasmas with an initial drift velocity. Associated with the shock wave is a characteristic spike in the longitudinal electric field which is capable of accelerating the upstream protons up to twice the velocity of the shock. For optimization of the shock speed which maximizes the energy of the reflected protons, the two key parameters are the initial drift velocity and the temperature of the plasma. For the laser-driven shock case, the initial drift velocity is compared to the hole boring velocity, highlighting the importance of the a_o of the laser and the near critical peak plasma density ($1 < n_{peak}/n_{cr} < 5$). Laser plasma heating is a complicated issue that depends grossly on the laser parameters (polarization, pulse width, energy) and plasma parameters (underdense plasma scale length, peak density). However, the most efficient heating is obtained when the peak plasma density is near the critical density of the laser allowing for a resonant interaction of the laser with the plasma electrons. Though many heating mechanisms have a dependence on the a_o of the laser, it was shown that heating the bulk of the plasma to MeV temperatures necessitates Joules of energy and therefore the total energy in the laser is also an important factor.

A picosecond multi-terawatt CO_2 laser was developed at the UCLA Neptune Laboratory for the purposes of experimentally investigating laser-driven SWA of ions. First, through simulations it was shown that the amplification of a picosecond pulse results in the production of a pulse train, or macropulse, of 3 ps pulses separated by 18 ps, a time characteristic to the separation between the CO_2 molecule rotational lines. Spectral gain broadening from the pressure of the gas mixture and the electric field of the laser pulse itself (field broadening) have been shown to be useful methods of concentrating the extracted laser energy into a shorter macropulse, or even single picosecond pulse. Amplification of a short pulse in this coherent amplification regime when field broadening dominates allows for the production of short macropulses resulting in high peak power while using low pressure (<3 atm) amplifiers capable of multiple Joule energy extraction and high repetition rate.

An experimental description of the UCLA Neptune Laboratory CO_2 laser system built on this basis is described. Both the pressure and field broadening mechanisms are used in a master oscillator-power amplifier laser chain resulting in a total extracted energy of 100 J which is distributed over several 3 ps pulses separated by 18 ps. Due to the high intensities in the final amplifier of up to 10^{11} W/cm^2, quasi-single pulse production is possible and a world record peak power of 15 TW was achieved. Further amplification of the obtained pulses in more passes of the final amplifier can induce Rabi flopping of the lasing transition as seen in the simulations which can lead to a significant shortening of the pulse from 3 ps down to $\sim$1 ps. Realization of such a scheme would allow for the generation of 100 TW at 10 μm in a single pulse, a power level unimaginable without coherent amplification. Ultimately, use of the full aperture of the final amplifier allowing for the amplification of a 10" beam could result in the production of a petawatt 10 μm laser pulse containing one kilojoule of energy in one picosecond.

This CO_2 laser system is then applied for SWA of protons in a H_2 gas jet where the peak plasma densities are 3-5 times the critical plasma density for 10 μm light (10^{19} cm^{-3}). Plasma density interferometry is developed to probe the laser-plasma interaction using a picosecond 532 nm pulse which uncovered a dynamically formed plasma profile with a sharp (10λ) rise to overcritical densities and a long exponential fall (30λ). Protons accelerated by this interaction were detected using CR-39 nuclear track detectors and an incremental etching technique was developed to allow for a 0.1 MeV spectral resolution around 20 MeV energies. Protons up to 22 MeV are detected with energy spreads as low as 1% and geometrical emittances as low as a few mm·mrad. 2D OSIRIS simulations elucidate the shock wave formation and propagation through the rear side of the gas jet where the long exponential plasma profile results in a slow and constant expansion. As the shock wave, traveling at a constant velocity of 0.16c, passes these expanding protons, they are reflected into a monoenergetic beam with an energy of up to 22 MeV. Due to the reduced sheath fields in a long exponentially decaying plasma density profile, the proton beam is able to exit the plasma while retaining its narrow energy spread.

These results are compared to the trend of LDIA proton energies plotted in Fig. 1.1 where it is clear that 20 MeV protons accelerated by a 4 TW laser show the superior scaling of SWA protons to those of TNSA and RPA. Furthermore, the majority of the accelerated protons are contained within an energy spread of ~1% which is a factor of 10 times smaller than the most narrow energy spread reported to date [53, 54]. 2D simulations show the potential of this acceleration mechanism to achieve 100's of MeV/a.m.u. ions with state-of-the-art 100 TW laser systems. Aside from potential application in areas requiring a high energy source of ions with a narrow energy spread such as cancer radiotherapy [35,36], the narrow energy spread and small emittance are beneficial to the control and further acceleration of the protons by external magnets and RF cavities. Expanding beyond protons to heavier ions is made simple using a gas jet plasma source which has the capability to provide many species of ions for various applications such as helium, carbon, nitrogen, oxygen, neon, argon, xenon etc.

As a closing remark, we would like to propose a method for scaling the laser-driven SWA mechanism from a 10 μm driver (CO_2) to the more abundant 1 μm (Nd:Glass) driver. Achieving extended plasmas with a peak density in the range of 1-10n_{cr} for a 10 μm laser pulse is easy with the use of a gas jet target. However, 1-10n_{cr} for 1 μm laser pulses corresponds to 10^{21} - 10^{22} cm^{-3}, and is therefore unreachable for gas jets, but is still far from solid density targets ($\sim 10^{23}$ cm^{-3}). A possible scenario for producing such a near critical plasma density profile for a 1 μm laser, similar to that obtained in a gas jet for 10 μm laser, is by the use of a pre-pulse to ionize a thin solid density target. After a certain time of expansion, a peak plasma density of 10^{21}-10^{22} cm^{-3} could certainly be reached where now the main 1 μm pulse is incident upon the plasma target. For easily achievable a_o's of 10 or above, ponderomotive steepening of the front side of the profile combined with the expansion on the back could in principle produce similar plasma profiles as those used here for the launching of collisionless shocks and the acceleration of ions. This is the natural progression of these results as Nd:Glass lasers are more abundant and can more easily reach peak a_o's of 10-20 as opposed to CO_2 lasers.

APPENDIX A

Streak Camera Dianostic for the Measurement of sub-ns 10 μm Laser Pulses

A streak camera diagnostic was built to measure the temporal structure of the amplified 10 μm macropulses. Two streak cameras were used over the course of the experiment. The primary streak camera is a Imacon 500 Hadland Photonics having a resolution of 5 ps and a shot-to-shot jitter of $\sim$200 ps. Due to its stability this camera was used on each high power laser shot to reveal the structure of the macropulse, though not resolving the individual 3 ps micropulses. To characterize the micropulses, a C5680 Hamamatsu streak camera having a measured 3 ps resolution (measurement described in Section A.2) was used. The shot-to-shot jitter of this camera is $\sim$1 ns therefore it could only be used in a reliable manner to measure the 10 μm pulses from the regenerative amplifier which can be operated at 1 Hz.

A.1 Experimental Setup of the Streak Camera Diagnostic

A portion of the streak camera diagnostic, using a similar setup to that described by Filip et. al. [92], is depicted in Fig. A.1. The spectral sensitivity of both streak cameras peaks in the visible wavelength range, therefore the 10 μm light is used to gate 658 nm, visibly red, before measurement. The gating is accomplished in a CS_2 Kerr cell in the same manner as that used for the picosecond 10 μm seed production described in detail in Section 4.1.

On each laser shot, 4% of the CO_2 laser beam reflects off the input salt window (see

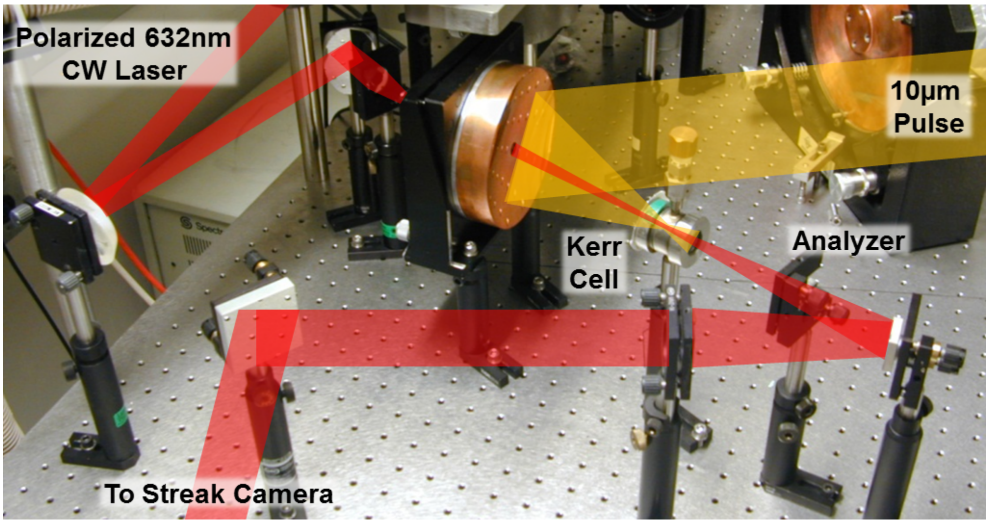

Figure A.1: A picture of the streak camera diagnostic. The yellow path denotes the propagation of a portion of the 10 μm beam reflecting from the input NaCl window on the target chamber. The red path denotes the propagation of a CW 658 nm beam propagating from a red diode laser.

Fig. 4.1), is attenuated down to less than 10 mJ, and is focused into the CS_2 Kerr cell by an F/1.5 off-axis parabolic mirror (OAP) as shown in Fig. A.1. This intense 10 μm pulse acts as the pump producing a temporal birefringence in the CS_2 liquid via the nonlinear index of refraction (see Section 4.1 for more detail). A 658 nm diode laser beam is used as the probe. After passing through a polarizer (behind the OAP mount in Fig. A.1) set at 45^o between s- and p-polarization, it is focused through a hole at the center of the OAP and propagates collinearly with the p-polarized 10 μm pulse overlapping through the Kerr cell. An analyzer then transmits only the portion of the diode pulse whose polarization has been rotated thus copying the temporal structure of the 10 μm macropulse. This transmitted pulse is then sent to the streak camera for measurement. A small portion of the green 532 nm probe pulse is also sent to the streak camera for simultaneous measurement yielding the temporal delay between the probe and 10 μm pulses at the IP.

An example of the raw data extracted from the streak camera on a high power laser

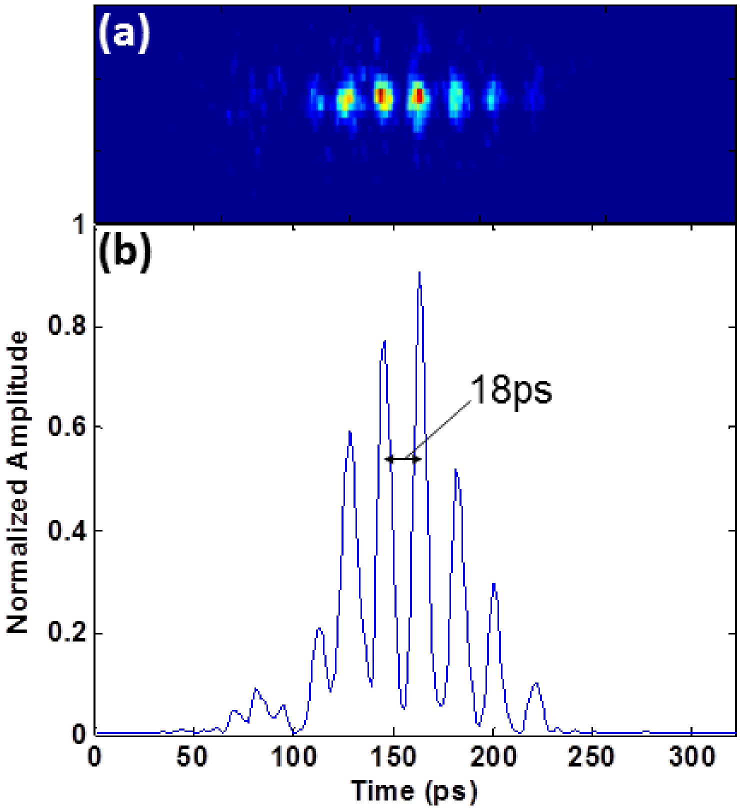

Figure A.2: Raw streak image from the streak camera (a) and the column sum of the data showing the temporal structure of the CO_2 macropulse (b).

shot is shown in Fig. A.2a. A simple column sum of the pixels reveals the temporal structure of the CO_2 macropulse as shown in A.2b. Clearly the macropulse structure showing a pulse separation of 18 ps is resolved where as the 3 ps pulsewidth of the micropulses is not. Due to an early saturation pixel count in the streak camera of ∼1000 counts and a noise floor pixel count of ∼50, the dynamic range of the measurement is limited to 20.

A.2 Resolution Measurement of the Hamamatsu C5680 Streak Camera

The temporal resolution of the Hamamatsu C5680 streak camera was measured using the second harmonic (532 nm) generation of the picosecond 1 μm pulses produced from the Nd:Glass CPA system described in Section 4.1. The pulsewidth of the 532 nm pulses were measured on the streak camera and a home made multi-shot autocorrelator for comparison. The pulse shape is assumed to be Gaussian and therefore the pulsewidth reported is a factor of $\sqrt{2}$ shorter than the measured autocorrelation width. The pulsewidth was changed by changing the spacing of the gratings in the Nd:Glass CPA system. The results are shown in Fig. A.3 where τ_p and τ_m are the FWHM pulsewidths as measured by the autocorrelator and streak camera, respectively.

Near the resolution limit of the streak camera, the response can be characterized by the following equation [118]:

$$\tau_p^2 = \tau_m^2 - \tau_{ins}^2 \tag{A.1}$$

where τ_p^2 is the actual pulsewidth (in this case measured by the autocorrelator), τ_m^2 is the pulsewidth as measured by the streak camera, and τ_{ins}^2 is the instrumental function, or temporal resolution, of the streak camera. Using τ_{ins} as a fitting parameter to the data in Fig. A.3 results in a $\tau_{ins} = 3$ ps (solid line). The scattering of the data is contained within $\tau_{ins} = 2.5$ ps and $\tau_{ins} = 3.5$ ps (dotted red lines) providing an experimental accuracy of 3±0.5 ps.

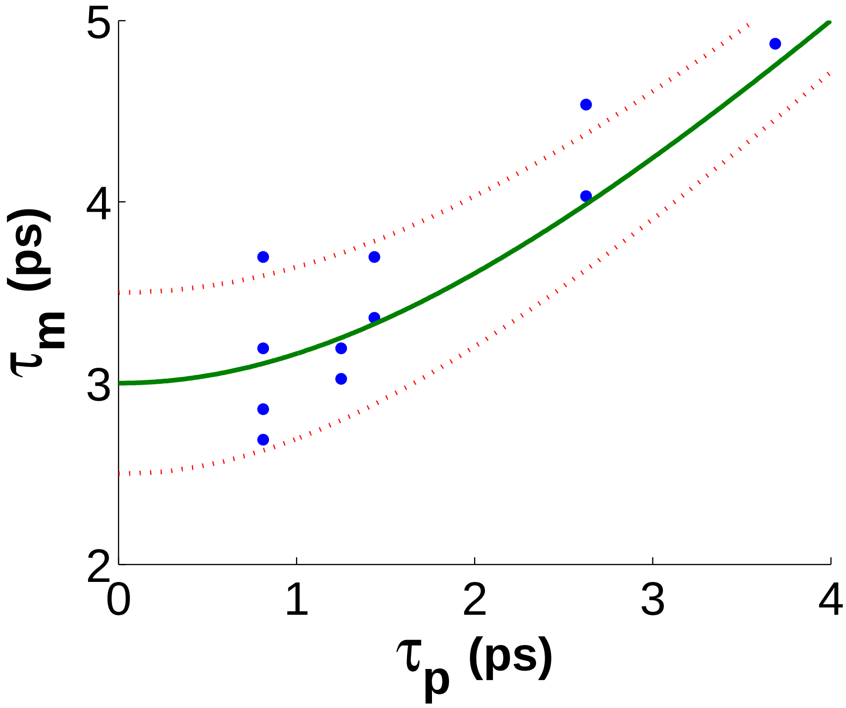

Figure A.3: Measurement of the FWHM pulsewidth of the second harmonic of the 1 μm pulse from the Nd:Glass CPA system (blue dots). τ_p and τ_m are the pulsewidths as measured by a multi-shot autocorrelator and the Hamamatsu C5680 streak camera, respectively. The solid line is the best fit of the equation $\tau_p^2 = \tau_m^2 - \tau_{ins}^2$ to the data which results in $\tau_{ins} = 3$ ps, where τ_{ins} is the instrumental function of the streak camera. The dotted red lines are a plot of the same equation with $\tau_{ins} = 2.5$ and 3.5 ps qualitatively bounding the scattering of the data.

APPENDIX B

Processing and Analysis of CR-39 Nuclear Track Detectors

B.1 Etching Procedure and Proton Pit Counting

CR-39 plastic nuclear detectors are widely used for the detection of energetic ions since they are not sensitive to electrons and x-rays [102–104]. After exposure to accelerated protons, each CR-39 is etched in a fresh 6N NaOH solution held at a constant temperaure of 80±0.1deg. A picture of the setup is shown in Fig. B.1 where one can see the glass container holding the NaOH solution, a plastic insert to provide separation of all the individual CR-39 pieces, and the hot plate along with the thermocouple probe which provides the feedback for temperature stabilization. A new solution was made for each set of CR-39's and the temperature was stabilized before inserting the pieces into the solution.

The CR-39's are etched in five hour increments which was empirically found to be the minimum etching time period to provide sufficient proton pit sizes to be resolved by the microscope ($\geq$10 μm). By carefully measuring the widths of the CR-39 plates with a caliper before and after etching, the bulk etching rate was calculated to be 10 μm/hr; therefore, each 5 hr increment removed $\sim$50 μm of bulk material from either side of the CR-39's. After etching, each CR-39 is cleaned thoroughly with distilled water and dried with compressed dry air.

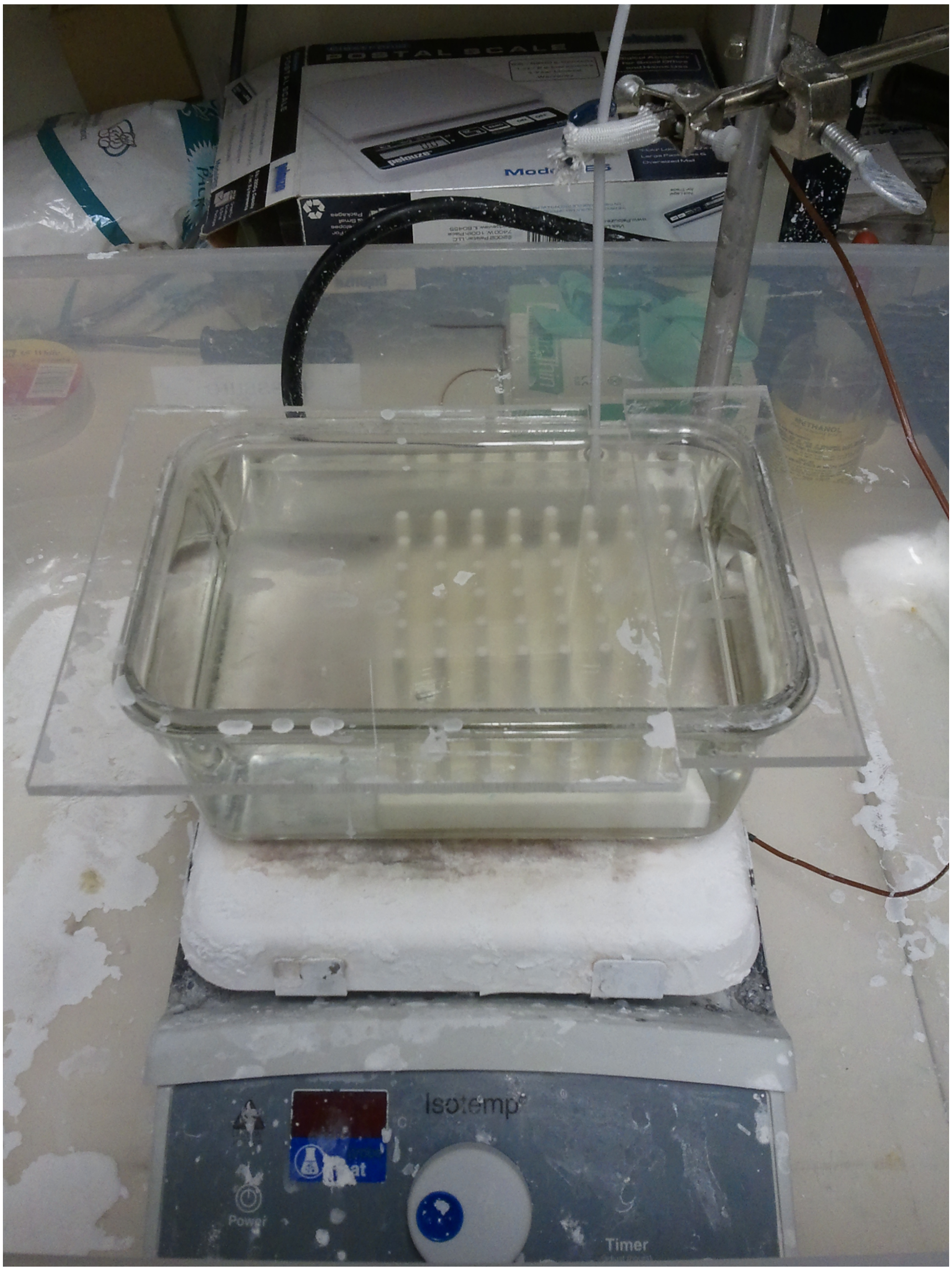

Figure B.1: A picture of the CR-39 etching station displaying the glass container holding the NaOH solution, a plastic insert to provide separation of all the individual CR-39 pieces, and the hot plate along with the thermocouple probe which provides the feedback for temperature stabilization.

The CR-39's are then viewed under a microscope at a magnification of 100. To take the data, first a 2-axis computer controlled actuator translates the CR-39 as a picture is taken by a CCD camera to record the entire surface. Second, a Matlab program [114] is run that analyzes the pictures searching for proton pits and calculates a total proton count. The energy of a detected proton is calculated by equating the distance traveled through the CR-39 plastic to the distance traveled by a proton of a certain energy to yield the Bragg peak at that location.

B.2 Fine Spectral Resolution

After the initial 5 hour etching period, monoenergetic features were then identified by a gross change in yield between adjacent data points. In these cases, further etching of the corresponding CR-39 in 5 hour increments up to a total of 20 hours was carried out to obtain a finer spectral resolution around the feature. Each 5 hour step in etching moves the plane of detection 50 μm deeper into the CR-39 plastic which corresponds to an incremental change in energy. In addition, we measured the pit diameters at each time step (plotted in Fig. B.2) which grew at a linear rate of 5 μm/hour. This rate was measured when etching an entire batch of CR-39's (16 pieces) at the same time. For the data presented in Fig. B.3 and Fig. B.4, only one CR-39 was etched at a time which yielded a pit diameter growth rate of $\sim$10 μm/hr. This linear dependence of the pit diameter growth rate on etching time enabled us to identify the protons that had a Bragg peak in each 50 μm slice of CR-39.

An example of this process is shown in Fig. B.3 which displays a representative microscope view of a CR-39 showing the proton pits (a: 5 hours, b: 10 hours), and a view of the location of all proton pits on the 50x50 mm^2 CR-39 plate (c: 5 hours, d: 10 hours). The corresponding distributions of measured proton pit diameters are shown in Fig. B.4a for 5 hours and Fig. B.4b for 10 hours. After 5 hours of etching, the size of the proton pits are rather homogeneous as seen in Fig. B.3a forming a sharp distribution in Fig. B.4a with all pits having a diameter less than 40 μm. After 10 hours of etching,

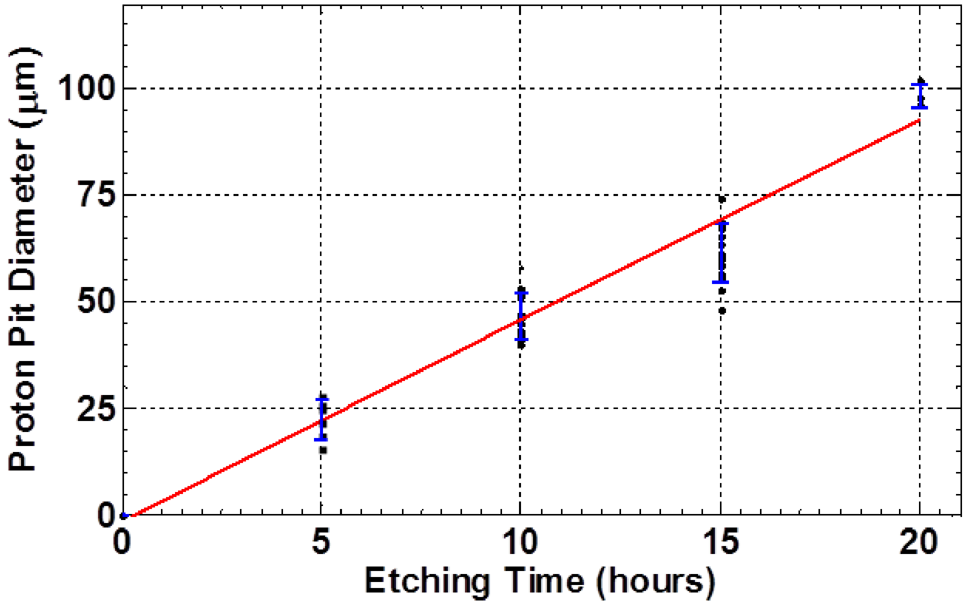

Figure B.2: Measured proton pit diameter plotted versus etching time in 5 hour increments. This data is for etching 16 pieces of CR-39's at the same time and results in a bulk etch growth rate of 5 μm/hr. Etching a single CR-39 piece results in a pit growth rate of 10 μm/hr.

visual inspection of the CR-39 under the microscope (Fig. B.3b) shows a clear qualitative distinction between the new small pits (of similar size to those in Fig. B.3a) and the old pits which have grown much larger. From the distribution of pit diameters shown in Fig. B.4b, we can see that the peaked distribution from Fig. B.4a has shifted by approximately 10 μm/hr x 5 hr = 50 μm and now is centered around 80 μm. Based on the distribution in Fig. B.4a, at each 5 hour increment of etching, only pits with diameters less than 40 μm are counted as new pits, which here results in the proton pit distribution shown in Fig. B.3d. This procedure has a counting error of 200 pits per detector plate. The detection system provides a spectral resolution of 0.1 MeV (50 μm slice) centered around 20 MeV.

The vast majority of the post processing (etching, pit counting, and analysis) of the CR-39's was carried out by Chao Gong. The author is grateful to him for his contributions to this work.

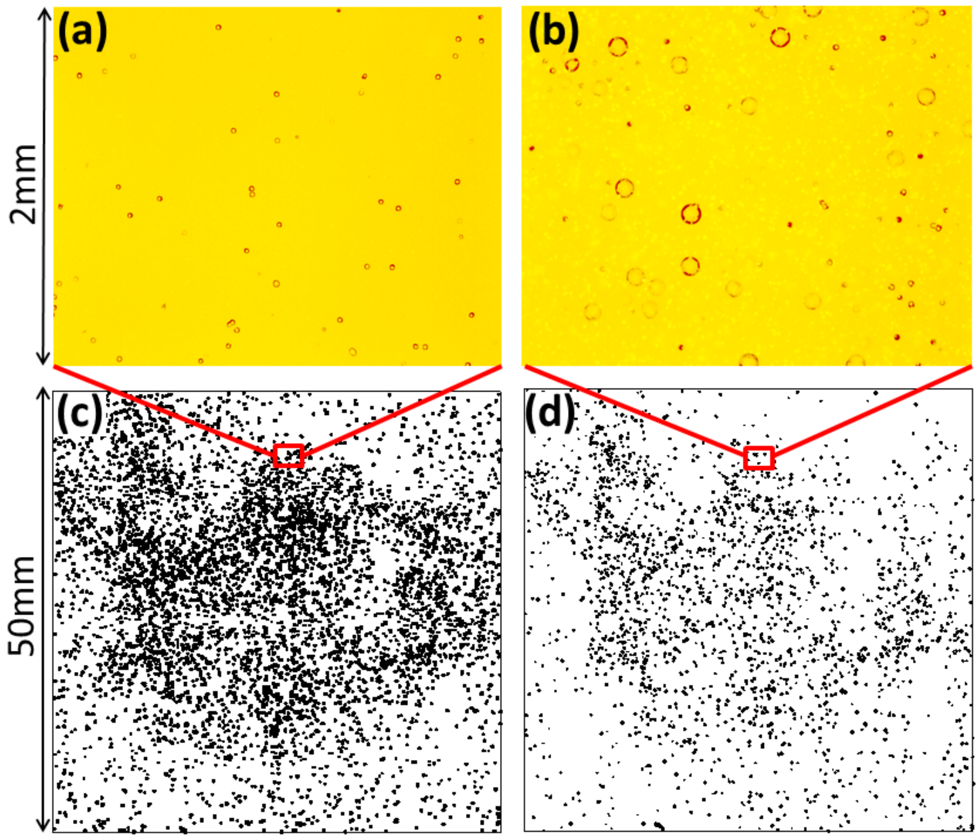

Figure B.3: Data obtained after etching a CR-39 piece for 5 hours and 10 hours. Here shown is a microscope view of the CR-39 reveling the actual proton pits (a: 5 hours, b: 10 hours), and a plot of the location of all new proton pits on the CR-39 plate (c: 5 hours, d: 10 hours).

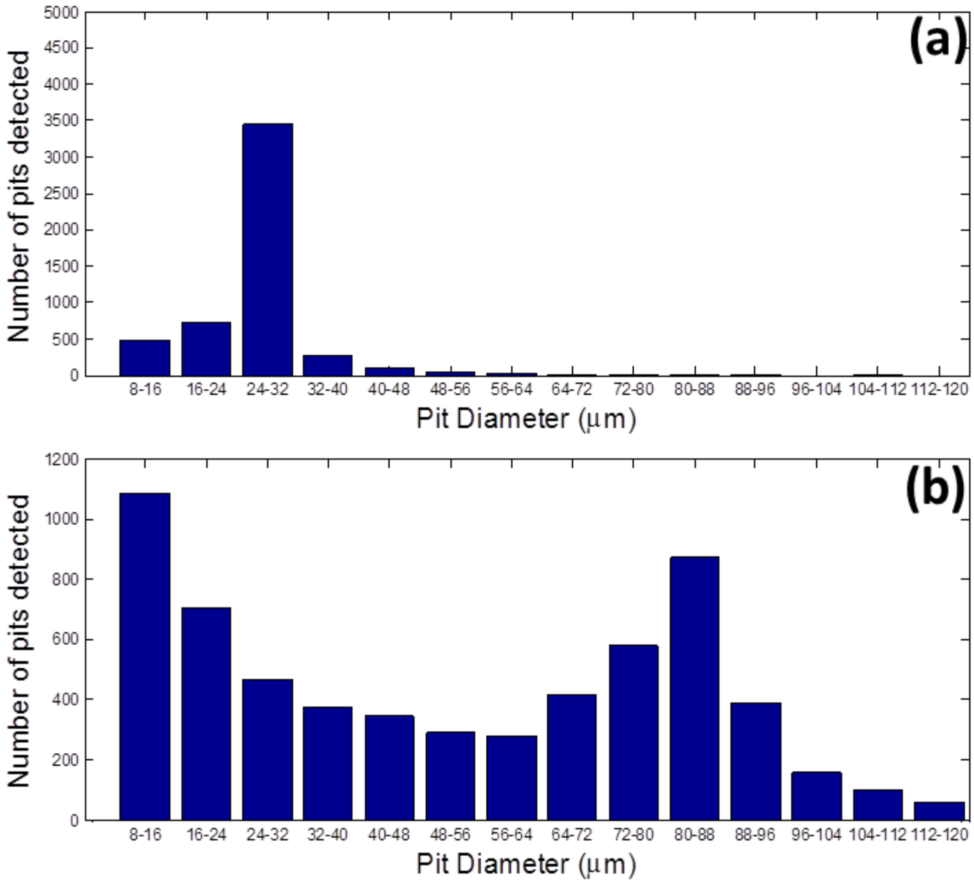

Figure B.4: Data obtained after etching a CR-39 piece for 5 hours and 10 hours. Here shown is the distribution of measured proton pit diameters for 5 hours (a) and 10 hours (b).

APPENDIX C

Analysis of Shot 14737 Interferogram

C.1 Manual Analysis of the Interferogram

Analysis of interferograms is typically performed using a phase retrieval and Abel inversion computational program [119–121]. The success of extracting an accurate 2D plasma density profile is contingent upon the homogeneity of the probe beam and the clarity of the interferogram, or the visibility, continuity, and sharpness of the fringes. In the interferogram of shot 14737 (shown in Fig. C.1a), portions of the fringes are clearly distorted resulting in a loss of phase information in those areas. This is due to strong plasma density gradients refracting the probe light which are present near the high density plasma walls surrounding the hole bored by the laser pulse. Due to this distortion, a computational analysis could not be undertaken.

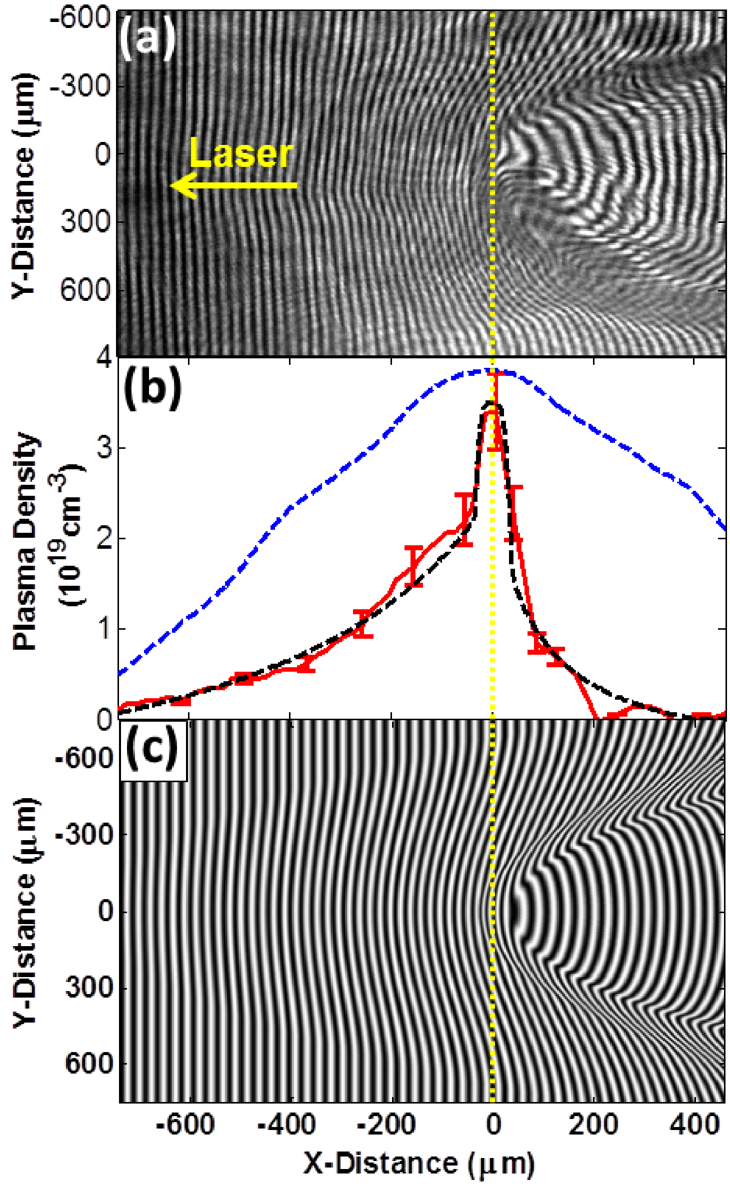

Figure C.1: a) Interferogram of the plasma on shot 14737 taken at the peak of the CO_2 laser macropulse showing the hole bored into the plasma by the laser pulse. b) The initial gas jet density profile (dotted-blue), the plasma density profile extracted from the interferogram in (a) (solid-red), and the simulated plasma density profile (dashed-black). c) Simulated interferogram using a 3D parabaloid plasma with a longitudinal profile shown in the black dashed line in (b).

To extract information from the interferogram, a manual analysis was developed that allowed for the estimation of the plasma density profile along the laser axis (y = 0) assuming the plasma density profile to be axisymmetric. The method involves a four step process :

1. Assumption of the shape of the plasma density profile in the transverse ($\hat{y}$) direction
2. Extraction of the total phase accrued by each fringe along the laser axis (y = 0) by comparison to the vacuum fringe position
3. Correction of the total phase due to geometric concerns
4. Calculation of the plasma density at each fringe according to Eq. 6.6 and 6.7

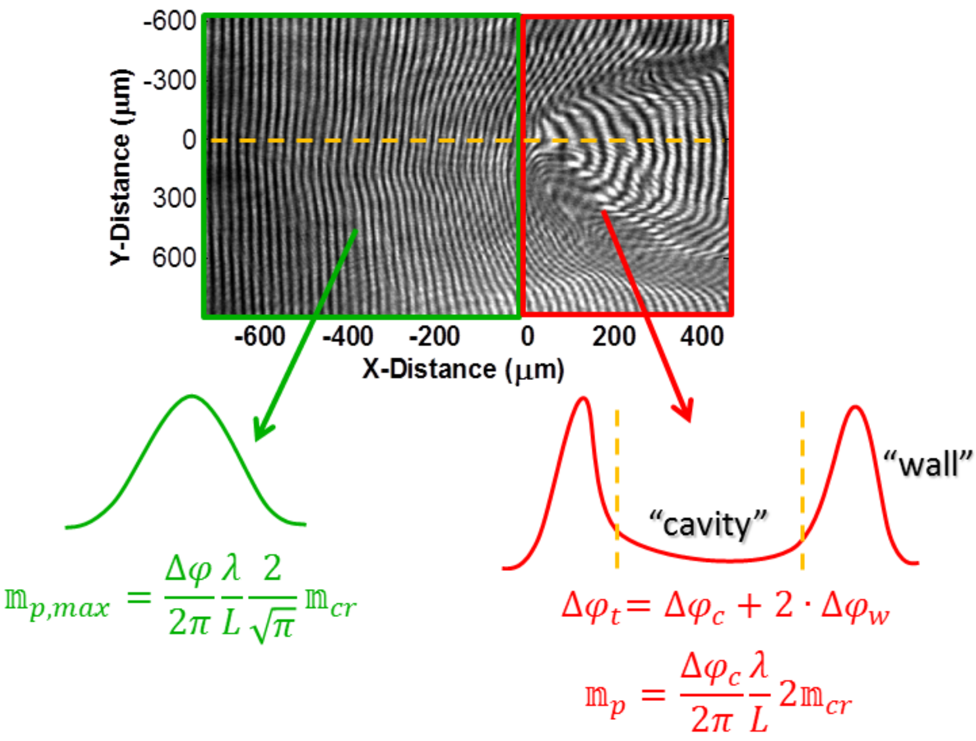

Figure C.2: Interferogram of shot 14737 with the designation of the assumed plasma density profiles downstream (Gaussian) of and upstream (cavity/walls) of the front of the hole bored by the laser macropulse. The corresponding equations for plasma density calculations are also shown.

As explained in Chapter 7, the laser is traveling from right to left in Fig. C.1 boring a hole through the overdense plasma. Therefore, it is natural to split the profile into two sections (seen in Fig. C.2): upstream ($x < 0$) where the laser has not propagated, and downstream ($x > 0$) where the laser has bored a hole. The assumed transverse plasma density profiles for the two sections are drawn into Fig. C.2, being Gaussian for the upstream side and two high density walls surrounding a low density cavity with a flat profile in the middle for the downstream side.

The total phase shift on axis ($y = 0$) is obtained by the comparison of the fringe positions in Fig. C.2 with those of a background interferogram taken with no plasma present. On the upstream side of the profile, the plasma density is calculated directly by measuring its 1/e characteristic length and using the equation for a Gaussian profile (Eq. 6.6). On the downstream side of the profile, however, the probe light accrues phase from passing through the two high density walls, ϕ_w (Fig. C.3), and from the low density cavity in between, ϕ_c (Fig. C.3). Therefore, the total phase shift measured on axis can be approximated as $\phi_t = \phi_c + 2\phi_w$. For calculating the longitudinal plasma density profile, we are only interested in the phase accrued inside the cavity for calculating the on-axis plasma density. Therefore, for each position along the laser axis, ϕ_w is estimated by comparing the fringe shift in the wall to the background interferogram, then subtracted from ϕ_t to isolate the phase shift due only to the plasma inside the cavity, ϕ_c.

One final consideration on the geometry of the plasma profile downstream needs to be taken into account before the plasma density on axis can be calculated. As depicted in Fig. C.3, an idealized cross-section of the profile taken along the dashed blue line in the interferogram is shown in the picture on the right where the dark blue circle represents the high density plasma wall surrounding the light blue area representing the low density cavity. Along the laser axis ($y = 0$), the ϕ_t measured inside the laser cavity results from the probe light traveling perpendicular to the high density plasma walls as shown by the dashed yellow line through the middle of the cross-section. However, the ϕ_w that is used to isolate the ϕ_c is measured from probe light that is traveling through a much longer

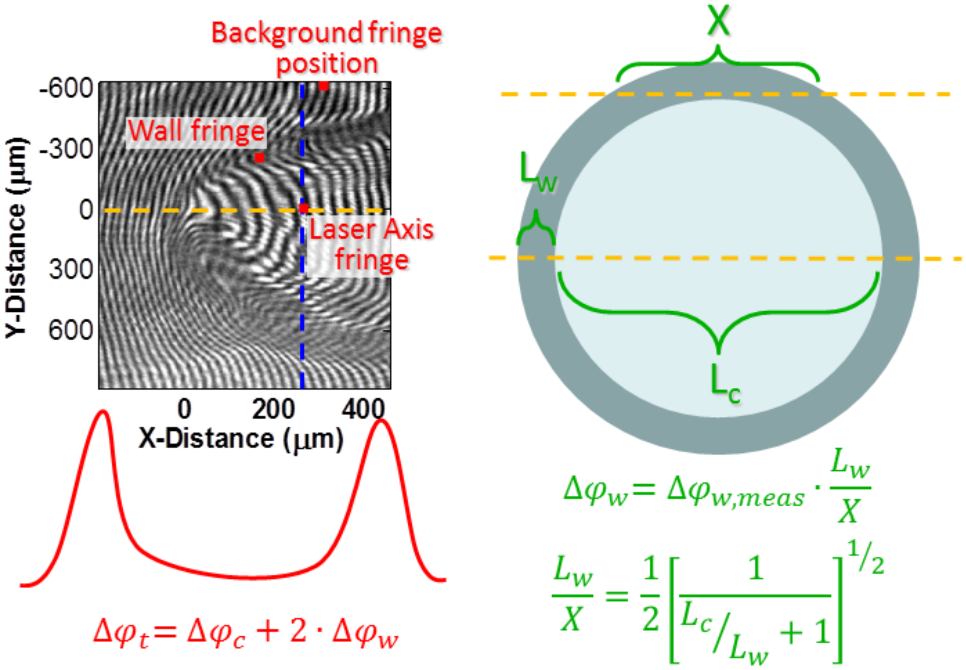

Figure C.3: Interferogram of shot 14737 along with the positions of a background, wall, and laser axis fringe denoted. The concentric circles represent an ideal cross-section of the plasma density profile taken along the black dashed line in the interferogram. The L_w/X equation is a geometrical correction to the measured phase accrued by a probe ray traveling through the plasma wall.

length along the plasma wall, and therefore accruing a larger phase, as shown by the dashed yellow line in the upper portion of the cross-section. At a constant density, since phase is linear with distance we can estimate the correction to the extracted phase by multiplying the ϕ_w by the ratio of the probe ray path in the plasma walls, or L_w/X as seen in Fig. C.3.

Finally, the density on axis in the downstream region is calculated assuming a flat plasma profile inside the cavity using Eg. 6.7. The Matlab script used to perform this analysis is shown in Section C.3. Application of this method to the interferogram in Fig. C.1a results in the density profile shown by the red line in Fig. C.1b. Though there are many sources of approximation in this analysis, the largest factor of error is due to the blurring of the interferogram along the laser axis (y = 0) as it crosses the high density plasma wall. In this area, it is a possibility that one fringe is missing due to the distortion of the image and therefore an error has been calculated based upon the addition of another fringe.

C.2 The Simulated Interferogram

Additional support for the extracted plasma profile seen in Fig. C.1a is gained through comparison to a simulated interferogram using a 3D plasma modeled after that observed in the experiment. The method of calculating the interferogram can be summarized in three basic steps :

1. A 3D matrix is created which stores the plasma density values based upon a 3D paraboloid with a longitudinal profile modeled after that extracted from the experiment (Fig. C.1b, dashed-black)
2. Integrate along the probe beam direction to calculate the accrued phase
3. Calculate the fringe pattern using an equation for the interference of two coherent plane wave beams including the additional phase of the plasma

An analysis of the interference between two identical plane wave laser beams propagating predominantly in the ẑ direction which are crossed with a small angle, θ, in the x̂ direction yields and intensity pattern :

$$I(x, y, z) = 2I_o[1 + (\alpha - \Delta\phi(x, y))] \tag{C.1}$$

$$\alpha = k_o[(1 - cos(\theta))z - sin(\theta)x] \tag{C.2}$$

where I_o is the intensity of each beam, k_o is the wave number of each beam, and $\Delta\phi$ is the additional phase due to the plasma placed in one of the laser beams. After mathematically creating a 3D plasma, the phase ($\Delta\phi$) is integrated along the probe direction and then used to calculate the corresponding interferogram according to Eq. C.2. The Matlab code [122] used to perform this analysis can be found in Section C.4 at the end of this Appendix. The longitudinal plasma profile used in the simulation is plotted in a black dashed line in Fig. C.1b which is modeled after that extracted from the experimentally measured interferogram. The resulting simulated interferogram is seen in Fig. C.1c. Though clearly the plasma in the experiment is more turbulent and the interferogram is distorted due to refraction of the probe light, the simulated interferogram is seen to contain the same basic features. Specifically note the change in curvature of the fringes near the high density wall (x = 0 μm) which is indicative of a change in the derivative of the plasma density. First, the fringes on the back side of the gas jet have a slowly increasing shift indicative of the long exponentially decreasing plasma density profile. At x = 0, the strong change in curvature of the fringes indicates the passing of the peak plasma density and rapid decline to low densities.

C.3 Matlab Script for Manual Analysis of Interferogram 14737

```
%--------------------------------------------------------------------------
%                 Manual Analysis of Interferogram 14737
%--------------------------------------------------------------------------
clc;
clear all;
close all;
%----------------Open Data and Background Interferograms-------------------
datafolder = 'C:\Users\Dan Haberberger\Documents\Neptune Data\Probe Data\2011-02-22\';
bkgfolder = 'C:\Users\Dan Haberberger\Documents\Neptune Data\Probe Data\2011-02-22\';
datafile = 'Interferometry 14737.tiff';
bkgfile = 'Interferometry 14740 background.tiff';
data = double(imread([datafolder,datafile]));
bkg = double(imread([bkgfolder,bkgfile]));
data = data - 32768; %correction for 12 bit images, Matlab only likes
bkg = bkg - 32768;   %8 bit or 16 bit

pixelsizex = 1.58; %in microns (=.88 for Old Schlieren)
pixelsizey = 1.58; %in microns (=.88 for Old Schlieren)
[leny lenx] = size(data);
x = 1:1:lenx;
y = 1:1:leny;
xmicron = x .* pixelsizex;
ymicron = y .* pixelsizey;
```

```
%----------manual marked spots of background fringes at y = 610um----------
blines = [7 21 35 49 63 78 92 106 120 135 149 163 177 192 206 ...
    220 234 248 262 277 291 305 319 333 346 361 375 389 403 418 ...
    432 446 460 475 489 503 517 532 546 560 574 588 602 617 631 ...
    645 660 674 688 702 717 730 745 758 773 787 801 816 830 844 ...
    859 873 888 902 916 930 945 959 973 987 1001 1016 1030 1044 ...
    1058 1073 1087 1101 1116 1130 1144 1159 1173 1188 1202 1217 ...
    1231 1245 1260 1274];
%-------------manual marked spots of data fringes at y = 610um-------------
dlines = [4 19 33 47 62 76 90 105 119 133 146 161 175 189 203 ...
    218 232 246 260 273 287 300 314 327 341 354 367 380 394 406 ...
    420 434 447 460 473 487 499 511 523 534 546 558 569 579 590 ...
    601 610 621 632 642 653 663 674 686 696 705 710 712 716 718 723 736 757 ...
    786 811 836 863 887 905 924 942 961 977 993 1010 1025 1042 ...
    1057 1073 1089 1104 1119 1134 1150 1166 1182 1197 1212 1228 ...
    1242];
%----------plotting lines on top of interferograms to check accuracy-------
lines = max(max(data)) .* ones(leny,1);
lines_sp = lines .*2;
for j = 1:1:length(blines)
    bkg(:,blines(j)) = lines;
    data(:,blines(j)) = lines;
end
data(:,blines(61)) = lines_sp;
data(:,dlines(61)) = lines_sp;
data(386,:) = max(max(data));
imagesc(x,ymicron,bkg)
figure
imagesc(x,ymicron,data)

%---------------measuring average separation of background lines-----------
for i = 1:length(blines)-2
    sep = blines(i+1)-blines(i);
end
meansep = mean(sep); %this gives me number of pixels per 2pi of phase

%-------------------------Back side plasma calculations---------------------
phase = blines - dlines; % phase difference in pixels
plength = (.9.*dlines + 480)./2;  % approximate fwhm at 1/e of gaussian
% dividing by two because what I measured is the full width at 1/e of the
% gaussian and what comes out of the integral is the half width at 1/e
lambda = 532e-7; %probe light wavelength (cm)
c = 3e10; %cm/sec
ncr = (1.24e-8)*(c^2)/(lambda^2); %cm^-3
plength = plength .* 1e-4; %change to cm

density = (phase ./ meansep) .* (lambda ./ plength) .* (2/sqrt(pi)) .* ncr;
%the above assumes a guassian profile, using equation from
%Interferometry chapter

%------------------------Front side plasma calculations---------------------
%----------------------calculating the phase in the walls-------------------
wlines = [741 752 768 787 807 834 850 867 881 893 907 923 938 958 974];
%wlines = pos of phase in wall
for i = 62:76
    wphase_large(i-61) = blines(i) - wlines(i-61);
end
```

```
%----------------------calculating geometric correction----------------------
%  Lw = wall width   Lc = cavity width
Lw = [400 350 300 300 300 270 261 260 254 202 180 160 140 140 140];
Lc = [100 159 218 288 346 394 434 468 505 594 590 618 637 645 655];
a = (Lc./2).^2;
b = ((Lc./2) + Lw).^2;
l = sqrt(b - a);
ratio = Lw ./ (2.*l);
wphase_small = wphase_large .* ratio;

%-------------------------correcting front side density-----------------------
densityc = density;
Lc = Lc .* 1e-4; %convert to cm
for i = 62:76
    pmeas(i-61) = phase(i)./meansep;
    pwall(i-61) = 2.*wphase_small(i-61)./meansep;
    densityc(i) = (lambda ./ Lc(i-61)).*(pmeas(i-61) - pwall(i-61)).* 2 .* ncr;
end

%-------------------------------plotting output----------------------------
xaxis = 1:1:15;
xplot = dlines .* pixelsizex;
density = density ./ 10^19;
densityc = densityc ./ 10^19;

figure;
plot(xplot,density,xplot,densityc)
xlim([400 1600])
xlabel('Space (\mum)','Fontsize',20)
ylabel('Plasma Density (10^{19}cm^{-3})','Fontsize',20)
legend('Before Correction','After Correction')
figure;
plot(xaxis,pmeas,xaxis,pwall,'r')
xlabel('Lines','Fontsize',20)
ylabel('Phase Shift (rad/2pi)','Fontsize',20)
legend('Phase Measured On Axis','Phase Measured in Wall')
```

C.4 Matlab Script for Producing a Simulated Interferogram Based on a 3D Plasma Profile

```
%---------------------------------------------------------------------------
%              Simulated Interferogram from 3D Plasma Profile
%---------------------------------------------------------------------------
clc;
clear all;
close all;

%----------for comparison to experimental profile---------
load('Simulated_Interferogram_14737_data.mat');
plot(xplot-415,densityc,'g','Linewidth',2)
hold on;
```

```
%----------------------input variables (units: meters)----------------------
nmax = 2.5e19 * 100^3; %peak plasma density in m^-3
nnorm = nmax / (1e19 * 100^3);
lamo = 532e-9;          %probe wavelength
fring_space = 23.7e-6; %fringe spacing (m)
xwindow = 1.5e-3;      %field of view in x direction
ywindow = 1.5e-3;      %field of view in y direction
zwindow = ywindow;
%----------------------physical constants----------------------------------
m = 9.1e-31;     %kg
eo = 8.85e-12;
qe = 1.6e-19;
c = 3e8;         %m/s
%----------------------mathematical constants------------------------------
theta = asin(lamo/fring_space);  %crossing angle for probe beams
ko = 2*pi/lamo;
wo = 2*pi*c/lamo;
%--------------------------------------------------------------------------
step = 7e-6;        %spatial step size : needs to be small to obtain a
            %nicely resolved interferogram but grossly affects runtime, can
            %crash Matlab if set too small
x = 0:step:xwindow; %real space x
y = 0:step:ywindow; %real space y
z = 0:step:zwindow; %real space z
xplot = x .* 10^6;  %for plotting in um
yplot = y .* 10^6;
zplot = z .* 10^6;
%--------------Creating Fringe Pattern from Crossed Beams-----------------
zz = 1;
alpha = ko*((1-cos(theta))*zz-sin(theta).*x);
int = nan .* zeros(length(y),length(x));
for o = 1:length(y)
    int(o,:) = 2*(1+cos(alpha));
end

%--------------------------------------------------------------------------
%                           Creating 3D Plasma
%--------------------------------------------------------------------------
% all the following code will be very specific to the 3D plasma profile
%----------------------Creating 3D Paraboloid Surface----------------------
offset = 742e-6;  %left-right position of tip of plasma
curvature = 1700; %arbitrary number representing the strength of curvature

xmid = xwindow/2;
ymid = ywindow/2;
zmid = zwindow/2;
x1 = nan .* zeros(length(y),length(z));
for j = 1:length(z)
    for k = 1:length(y)
        x1(k,j) = curvature*((y(k)-ymid).^2 + (z(j)-zmid).^2) + offset;
    end
end
%-----------------------Creating 3D Paraboloid Volume----------------------
wbexp = 450e-6;    %characteristic length of exponential function on back
wfexp = 50e-6;     %characteristic length of exponential function on front
lbexp = 800e-6;    %length of profile to zero density on back
lfexp = 450e-6;    %length of profile to zero density on front
```

```
%script to widen width of exponentials away from center in Y-dir and Z-dir
%if needed, but there is a line to cancel the effect
walls = x1 ./ min(min(x1));  %get a normalized parabaloid function
walls = walls ./ walls;      %cancel the effect, comment this out if the
wbexp = walls .* wbexp;      %effect is desired
wfexp = walls .* wfexp;
lbexp = walls .* lbexp;
lfexp = walls .* lfexp;

N = nan .* zeros(length(x),length(y),length(z));
center = nan .* zeros(length(y),length(z));
for j = 1:length(z)
    for k = 1:length(y)
        %finding center of paraboloid or exit if no center
        l = 1;
        while x(l) < x1(k,j)
            l = l + 1;
            if l == length(x)
                break
            end
        end
        center(k,j) = l-1;
        %-----making an exponential on back side of plasma
        b1 = x1(k,j) + wbexp(k,j);
        exponential = -wbexp(k,j)./(x-b1);
        c1 = (1/lbexp(k,j));
        d1 = (x1(k,j)-lbexp(k,j));
        triangular = c1.*(x-d1);
        N(1:l,k,j) = exponential(1:l) .* triangular(1:l);
        %------making an exponential on the front side of plasma
        b2 = x1(k,j) - wfexp(k,j);
        exponential = wfexp(k,j)./(x-b2);
        c2 = -(1/lfexp(k,j));
        d2 = (x1(k,j)-lfexp(k,j)) + 2/(1/lfexp(k,j));
        triangular = c2*(x-d2);
        N(l:length(x),k,j) = exponential(l:length(x)) ...
            .* triangular(l:length(x));
    end
end

%checking lineout down the center of the plasma before making
%wall into a supergaussian
densityplot = N(:,round(length(y)/2),round(length(z)/2));
plot(xplot,densityplot .* nnorm,'r');
ylabel(['Plasma Density',sprintf('\n'),'(10^{19}cm^{-3})'],...
    'Fontsize',15,'Fontweight','Bold')
xlabel('Space  (\fontsize{19}\mu\fontsize{15}m)','Fontsize',15,...
    'Fontweight','Bold');
set(gca,'Fontsize',15,'Fontweight','Bold')
hold on;

%widening the width of the plasma walls to form a supergaussian
walls = x1 ./ min(min(x1));       %get a normalized parabaloid function
centerwall = 80;                  %width of plasma wall along laser axis
width = (walls .^ 2.5) .* centerwall;  %width of plasma walls in microns
mwidth = width .* (.0001/186);    %get correct number for gaussian function
sharpness = 4;                    %sharpness of plasma walls
```

```
for j = 1:length(z)
    for k = 1:length(y)
        if center(k,j) ~= length(x) - 1;
            for l = 1 : length(x)
                func = 1.4*exp(-((x(l)-x(center(k,j)))/mwidth(k,j))...
                    .^sharpness);
                if func > N(l,k,j)
                    N(l,k,j) = func;
                end
                if l == length(x)
                    break;
                end
            end
        end
        degree = round((walls(k,j))^6);      %smoothing the profile to rid
        N(:,k,j) = smooth(N(:,k,j),degree);  %of discontinuities
    end
end
%--------------------get rid of any negative densities--------------------
for j = 1:length(z)
    for k = 1:length(y)
        for l = 1:length(x)
            if N(l,k,j) < 0
                N(l,k,j) = 0;
            end
        end
    end
end
densityplot = N(:,round(length(y)/2),round(length(z)/2));
plot(xplot,densityplot.*nnorm,'b');
%----------------------3D Plasma Profile Complete-------------------------

%-------------Finding Phase of Probe Beam through Plasma-------------------
dphi = zeros(length(y),length(x));
for l = 1:length(x)
    for k = 1:length(y)
        integral = step .* trapz(N(l,k,:));
        dphi(k,l) = ((lamo*qe^2)/(4*pi*c^2*m*eo)) .* nmax .* integral;
    end
end

%---Finally, calculate fringe pattern with additional plasma phase--------
intsp = zeros(length(y),length(x));
for l = 1:length(x)
    for k = 1:length(y)
        intsp(k,l) = 2*(1+cos(alpha(l)-(dphi(k,l))));
    end
end

%-------------------------------------------------------------------------
%                 Calculations complete, outputting data
%-------------------------------------------------------------------------

%------------------Output Cross-sections of Plasma----------------
crossyz = nan .* zeros(length(y),length(z));
for j = 1:length(z)
    for k = 1:length(y)
```

```
        crossyz(k,j) = N(120,k,j);
    end
end
crossxy = nan .* zeros(length(x),length(y));
for l = 1:length(x)
    for k = 1:length(y)
        crossxy(l,k) = N(l,k,round(length(z)/2));
    end
end
crossxz = nan .* zeros(length(x),length(z));
for j = 1:length(z)
    for l = 1:length(x)
        crossxz(l,j) = N(l,round(length(y)/2),j);
    end
end
fig1 = figure;
set(fig1,'Units','normalized','Position',[.1 .1 .8 .8]);
subplot(2,2,1)
    imagesc(xplot,yplot,crossyz)
    title('YZ cross-section of density','Fontsize',15,'Fontweight','Bold')
    xlabel('Space (um)','Fontsize',15,'Fontweight','Bold')
    colorbar;
    caxis([0 1.5]);
subplot(2,2,2)
    imagesc(xplot,yplot,crossxy)
    title('XY cross-section of density','Fontsize',15,'Fontweight','Bold')
    xlabel('Space (um)','Fontsize',15,'Fontweight','Bold')
    colorbar;
    caxis([0 1.5]);
subplot(2,2,3)
    imagesc(xplot,yplot,crossxz)
    title('XZ cross-section of density','Fontsize',15,'Fontweight','Bold')
    xlabel('Space (um)','Fontsize',15,'Fontweight','Bold')
    colorbar;
    caxis([0 1.5]);
subplot(2,2,4)%also output a cross-section of additional phase-informative
    imagesc(xplot,yplot,dphi);
    title('Cross-section of Probed Phase from Plasma (rad)',...
        'Fontsize',15,'Fontweight','Bold');
    xlabel('Space (um)','Fontsize',15,'Fontweight','Bold')
    colorbar;
    caxis([0 50]);
%Output final simulated interferogram in black/white for paper figure
figure;
    imagesc(xplot,yplot,intsp);
    title(['N_{max} = ',num2str(nmax./10^24)...
        ,'x10^{18}cm^{-3}   Width_{wall} = ',num2str(centerwall),'um']...
       ,'Fontsize',15,'Fontweight','Bold');
    set(gca,'Fontsize',15,'Fontweight','Bold')
    ylabel('Space (\fontsize{19}\mu\fontsize{15}m)','Fontsize'...
        ,15,'Fontweight','Bold')
    colormap gray;
    xlim([0 1200]);
    xlabel('Space (um)','Fontsize',15,'Fontweight','Bold')
    colorbar;
```

References

[1] A. G. York *et al.*, "Direct acceleration of electrons in a corrugated plasma waveguide," *Phy. Rev. Lett.*, vol. 100, p. 195001, 2008.

[2] Y. Y. Li *et al.*, "Direct laser acceleration of electrons by an ultra intense and short-pulsed laser in under-dense plasma," *Phy. Plasmas*, vol. 18, p. 053104, 2011.

[3] E. Esarey, C. B. Schroeder, and W. P. Leemans, "Physics of laser-driven plasma-based electron accelerators," *Rev. Mod. Phys.*, vol. 81, p. 1229, 2009.

[4] J. Fuchs *et al.*, "Laser-driven proton scaling laws and new paths towards energy increase," *Nature Phys.*, vol. 2, p. 48, 2006.

[5] L. Robson *et al.*, "Scaling of proton acceleration driven by petawatt-laser-plasma interactions," *Nature Phys.*, vol. 3, p. 58, 2007.

[6] T. Esirkepov, M. Borghesi, S. V. Bulanov, G. Mourou, and T. Tajima, "Highly efficient relativistic-ion generation in the laser-piston regime," *Phys. Rev. Lett.*, vol. 92, p. 175003, 2004.

[7] A. Macchi, F. Cattani, T. V. Liseykina, and F. Cornolti, "Laser acceleration of ion bunches at the front surface of overdense plasmas," *Phys. Rev. Lett.*, vol. 94, p. 165003, 2005.

[8] P. B. corkum and F. Krausz, "Attosecond science," *Nature Phys.*, vol. 3, p. 381, 2007.

[9] V. Malka *et al.*, "Principles and applications of compact laserplasma accelerators," *Nature Phys.*, vol. 4, p. 447, 2008.

[10] H. Daido, "Review of soft x-ray laser researches and developments," *Rep. Prog. Phys.*, vol. 65, p. 1513, 2002.

[11] F. Gruner *et al.*, "Design considerations for table-top, laser-based vuv and x-ray free electron lasers," *Appl. Phys. B*, vol. 86, p. 431, 2007.

[12] U. Eichmann, T. Nubbemeyer, H. Rottke, and W. Sander, "Acceleration of neutral atoms in strong short-pulse laser fields," *Nature*, vol. 461, p. 1261, 2009.

[13] P. B. Corkum, P. P. Ho, R. R. Alfano, and J. T. Manassah, "Generation of infrared supercontinuum covering 3-14 micron in dielectrics and semiconductors," *Opt. Lett.*, vol. 10, p. 624, 1985.

[14] S. H. Glenzer *et al.*, "Symmetric inertial confinement fusion implosions at ultra-high laser energies," *Science*, vol. 327, p. 1228, 2010.

[15] C. K. N. Patel, "Continuous-wave laser action on vibrational-rotational transitions of CO_2," *Phys. Rev.*, vol. 136, p. A1187, 1964.

[16] 150 kW CO_2 laser at the Air Force Research Lab. [Online]. Available: http://ammtiac.alionscience.com/pdf/AMPQ8_1ART04.pdf

[17] L. Randolph *et al.*, "Helios: A 15 TW carbon dioxide laser-fusion facility," *IEEE J. Quan. Electron.*, vol. QE-17, p. 1662, 1981.

[18] J. Deile and J. Mozdzierz, "Carbon dioxide lasers : **S**till the most successful in industrial applications," *Photonics Spectra*, p. 58, October 2007.

[19] M. R. Armenakas, J. S. Dover, and K. A. Arndt, "The spectrum of laser skin resurfacing: Nonablative, frational, and ablative laser resurfacing," *J. Am. Acad. Dermatol.*, vol. 58, p. 719, 2008.

[20] R. M. Pick and B. C. Pecaro, "Use of the CO_2 laser in soft tissue dental surgery," *Lasers in Surg. and Med.*, vol. 7, p. 207, 1987.

[21] D. Strickland and G. Mourou, "Compression of amplified chirped optical pulses," *Opt. Commun.*, vol. 56, p. 219, 1985.

[22] V. Yanovsky *et al.*, "Ultra-high intensity- 300-TW laser at 0.1Hz repetition rate," *Opt. Exp.*, vol. 16, p. 2109, 2008.

[23] I. Pogorelsky *et al.*, "Subnanosecond multi-gigawatt CO_2 laser," *IEEE J. Quan. Electron.*, vol. 31, p. 556, 1995.

[24] I. Pogorelsky (2^{nd}) *et al.*, "Proton and ion beams generaged with picosecond CO_2 laser pulses," in *Proceedings of the 13^{th} Advanced Accelerator Concepts Workshop*, 2009, p. 532.

[25] S. Y. Tochitsky *et al.*, "Generation of 160-ps terawatt-power CO_2 laser pulses," *Opt. Lett.*, vol. 24, p. 1717, 1999.

[26] S. Y. Tochitsky (2^{nd}) *et al.*, "Efficient shortening of self-chirped picosecond pulses in a high-power CO_2 amplifier," *Opt. Lett.*, vol. 26, p. 813, 2001.

[27] P. B. Corkum, "Amplification of picosecond 10μm pulses in multiatmosphere CO_2 lasers," *IEEE J. Quantum Electron.*, vol. QE-21, p. 216, 1985.

[28] D. Haberberger, S. Tochitsky, and C. Joshi, "Fifteen terawatt picosecond CO_2 laser system," *Opt. Exp.*, vol. 18, p. 17865, 2010.

[29] S. H. Autler and C. H. Townes, "Stark effect in rapidly varying fields," *Phys. Rev.*, vol. 100, p. 703, 1955.

[30] C. Joshi, M. C. Richardson, and G. D. Enright, "Quantitative measurements of fast ions from CO_2 laser produced plasmas," *Appl. Phys. Lett.*, vol. 34, p. 625, 1979.

[31] E. L. Clark *et al.*, "Measurements of energetic proton transport through magnetized plasma from intense laser interactions with solids," *Phys. Rev. Lett.*, vol. 84, p. 670, 2000.

[32] R. A. Snavely *et al.*, "Intense high-energy proton beams from petawatt-laser irradiation of solids," *Phys. Rev. Lett.*, vol. 85, p. 2945, 2000.

[33] T. E. Cowan *et al.*, "Ultralow emittance, multi-MeV proton beams from a laser virtual-cathode plasma accelerator," *Phys. Rev. Lett.*, vol. 92, p. 204801, 2004.

[34] M. Borghesi *et al.*, "Electric field detection in laser-plasma interaction experiments via the proton imaging technique," *Phys. Plasmas*, vol. 9, p. 2214, 2002.

[35] S. V. Bulanov, T. Z. Esirkepov, V. S. Khoroshkov, A. V. Kuznetsov, and F. Pegoraro, "Oncological hadrontherapy with laser ion accelerators," *Phys. Lett. A*, vol. 299, p. 240, 2002.

[36] U. Linz and J. Alonso, "What will it take for laser driven proton accelerators to be applied to tumor therapy?" *Phys. Rev. STAB*, vol. 10, p. 094801, 2007.

[37] I. Spencer *et al.*, "Laser generation of proton beams for the production of short-lived positron emitting isotopes," *Nucl. Instrum. Methods B*, vol. 183, p. 449, 2001.

[38] K. Krushelnick *et al.*, "Ultrahigh-intensity laser-produced plasmas as a compact heavy ion injection source," *IEEE Tran. Plasma Sci.*, vol. 28, p. 1110, 2000.

[39] M. Roth *et al.*, "Fast ignition by intense laser-accelerated proton beams," *Phys. Rev. Lett.*, vol. 86, p. 436, 2001.

[40] A. Noda *et al.*, "Laser ion production as the injector for cancer therapy synchrotron," in *Proceedings of* LINAC*2002, Gyeongju, Korea*, 2002, p. 644.

[41] K. W. D. Ledingham and W. Galster, "Laser driven particle and photon beams and some applications," *New J. Phys.*, vol. 12, p. 045005, 2010.

[42] S. C. Wilks and W. L. Kruer, "Absorption of ultrashort, ultra-intense laser light by solids and overdense plasmas," *IEEE J. Quan. Elec.*, vol. 33, p. 1954, 1997.

[43] K. A. Flippo *et al.*, "Ablation cleaning techniques for high-power short-pulse laser-produced heavy-ion targets," *Proc. of SPIE*, vol. 6261, p. 626121, 2006.

[44] M. Hegelich *et al.*, "MeV ion jets from short-pulse-laser interaction with thin foils," *Phys. Rev. Lett.*, vol. 89, p. 085002, 2002.

[45] B. M. Hegelich *et al.*, "Laser acceleration of quasi-monoenergetic MeV ion beams," *Nature*, vol. 439, p. 441, 2006.

[46] H. Schwoerer *et al.*, "Laser-plasma acceleration of quasi-monoenergetic protons from microstructured targets," *Nature*, vol. 439, p. 445, 2006.

[47] T. Toncian *et al.*, "Ultrafast laser-driven microlens to focus and energy-select mega-electron volt protons," *Science*, vol. 312, p. 410, 2011.

[48] M. Schollmeier *et al.*, "Controlled transport and focusing of laser-accelerated protons with miniature magnetic devices," *Phys. Rev. Lett.*, vol. 101, p. 055004, 2008.

[49] A. Noda *et al.*, "Phase rotation scheme of laser-produced ions for reduction of the energy spread," *Laser Physics*, vol. 16, p. 647, 2006.

[50] A. Macchi, S. Veghini, T. V. Liseykina, and F. Pegoraro, "Radiation pressure acceleration of ultrathin foils," *New J. Physics*, vol. 12, p. 045013, 2010.

[51] A. Henig *et al.*, "Radiation-pressure acceleration of ion beams driven by circularly polarized laser pulses," *Phys. Rev. Lett.*, vol. 103, p. 245003, 2009.

[52] F. Pegoraro and S. V. Bulanov, "Photon bubbles and ion acceleration in the plasma dominated by the radiation pressure of an electromagnetic pulse," *Phys. Rev. Lett.*, vol. 99, p. 065002, 2007.

[53] C. Palmer *et al.*, "Monoenergetic proton beams accelerated by a radiation pressure driven shock," *Phys. Rev. Lett.*, vol. 106, p. 014801, 2011.

[54] Z. Najmudin *et al.*, "Observation of impurity free monoenergetic proton beams from the interaction of a CO_2 laser with a gaseous target," *Phys. Plasmas*, vol. 18, p. 056705, 2011.

[55] K. Zeil *et al.*, "The scaling of proton energies in ultrashort pulse laser plasma acceleration," *New J. Physics*, vol. 12, p. 045015, 2010.

[56] L. Romagnani *et al.*, "Observation of collisionless shocks in laser-plasma experiments," *Phys. Rev. Lett.*, vol. 101, p. 025004, 2008.

[57] S. S. Moiseev and R. Z. Sagdeev, "Collisionless shock waves in plasma in a weak magnetic field," *J. Nuc. Energy C*, vol. 5, p. 43, 1963.

[58] R. Z. Sagdeev and C. F. Kennel, "Collisionless shock waves," *Sci. Am.*, vol. 264, p. 106, April 1991.

[59] O. Adriani *et al.*, "PAMELA measurements of cosmic-ray, proton, and helium spectra," *Science*, vol. 332, p. 69, 2011.

[60] D. Haberberger *et al.*, "Collisionless shocks in laser-produced plasma generate monoenergetic high-energy proton beams," *Nature Phys.*, vol. 8, p. 95, 2012.

[61] R. K. Dodd, J. C. Eilbeck, J. D. Gibbon, and H. C. Morris, *Solitons and Nonlinear Wave Equations.* London: Academic Press Inc., 1982.

[62] R. Z. Sagdeev, "The 1976 oppenheimer lectures: Critical problems in plasma astrophysics. II. singular layers and reconnection," *Rev. Mod. Phys.*, vol. 51, p. 11, 1979.

[63] D. Montgomery and G. Joyce, "Shock-like solutions of the electrostatic Vlasov equation," *J. Plasma Phys.*, vol. 3, p. 1, 1968.

[64] D. W. Forslund and C. R. Shonk, "Formation and structure of electrostatic collisionless shocks," *Phys. Rev. Lett.*, vol. 25, p. 1699, 1970.

[65] D. W. Forslund and J. P. Freidberg, "Theory of laminar collisionless shocks," *Phys. Rev. Lett.*, vol. 27, p. 1189, 1971.

[66] D. Biskamp, "Collisionless shock waves in plasmas," *Nuc. Fus.*, vol. 13, p. 719, 1973.

[67] J. Denavit, "Absorption of high-intensity subpicosecond lasers on solid density targets," *Phys. Rev. Lett.*, vol. 69, p. 3052, 1992.

[68] L. O. Silva *et al.*, "Proton shock acceleration in laser-plasma interactions," *Phys. Rev. Lett.*, vol. 92, p. 015002, 2004.

[69] D. A. Tidman and N. A. Krall, *Shock Waves in Collisionless Plasmas.* New York: Wiley-Interscience, 1971.

[70] F. Fiuza *et al.*, "Laser-driven shock acceleration of mono-energetic ion beams," *Phys. Rev. Lett.*, Submitted.

[71] G. Sorasio, M. Marti, R. Fonseca, and L. O. Silva, "Very high mach-number electrostatic shocks in collisionless plasmas," *Phys. Rev. Lett.*, vol. 96, p. 045005, 2006.

[72] R. A. Fonseca *et al.*, "Osiris, a three-dimensional fully relativistic particle in cell code for modeling plasma based accelerators," *Lec. Not. Comput. Sci.*, vol. 2331, p. 342, 2002.

[73] G. Sarri, M. E. Dieckmann, I. Kourakis, and M. Borghesi, "Generation of a purely electrostatic collisionless shock during the expansion of a dense plasma through a rarefied medium," *Phys. Rev. Lett.*, vol. 107, p. 025003, 2011.

[74] P. Mora, "Plasma expansion into a vacuum," *Phys. Rev. Lett.*, vol. 90, p. 185002, 2003.

[75] J. Denavit, "Collisionless plasma expansion into a vacuum," *Phys. Fluids*, vol. 22, p. 1384, 1979.

[76] F. Chen, *Introduction to Plasma Physics and Nuclear Fusion.* New York: Plenium Press, 1984.

[77] J. D. Huba, *NRL Plasma Formulary.* Washington DC: Naval Research Laboratory, 2011.

[78] L. Spitzer, *Physics of Fully Ionized Gases.* New York: Interscience, 1962.

[79] W. L. Kruer, *The Physics of Laser Plasma Interactions.* Boulder, Colorado: Westview Press, 2003.

[80] F. Tsung, S. Y. Tochitsky, D. J. Haberberger, W. B. Mori, and C. Joshi, "CO_2 laser acceleration of forward directed MeV proton beams in a gas target at critical plasma density," *J. Plasma Phys.*, p. Published Online, 2012.

[81] O. R. Wood, "High-pressure pulsed molecular lasers," *Proceedings of the IEEE*, vol. 61, p. 355, 1974.

[82] C. Fenstermacher, "High-energy short-pulse carbon dioxide lasers," *Phil. Trans. R. Soc. Lond. A*, vol. 298, p. 377, 1980.

[83] R. K. Brimacombe and J. Reid, "Accurate measurements of pressure-broadened linewidths in a transversely excited CO_2 discharge," *IEEE J. Quantum Electron.*, vol. QE-19, p. 1668, 1983.

[84] R. K. Brimacombe and J. Reid (2^{nd}), "Influence of the dynamic stark effect on the small-signal gain of optically pumped 4.3- μm CO_2 lasers," *J. Appl. Phys.*, vol. 58, p. 1141, 1985.

[85] R. K. Brimacombe and J. Reid (3^{rd}), "Measurements of anomalous gain coefficients in transversely excited CO_2 lasers," *IEEE J. Quantum Electron.*, vol. QE-19, p. 1674, 1983.

[86] V. Platonenko and V. D. Taranukhin, "Coherent amplification of light pulses in media with a discrete spectrum," *Sov. J. Quantum Electron.*, vol. 13, p. 1459, 1983.

[87] A. E. Siegman, *Lasers.* Mill Valley: University of Science Books, 1986.

[88] L. Wang, J. E. Reutt, Y. T. Lee, and D. A. Shirley, "High resolution UV photoelectron spectroscopy of CO_2, COS, and CS_2 using supersonic molecular beams," *J. Electron Spectrosc. Relat. Phenom.*, vol. 47, p. 167, 1988.

[89] M. Polyanskiy, "CO_2 amplification simulation program written in C++," 2009.

[90] B. Sheehy *et al.*, "High harmonic generation at long wavelengths," *Phys. Rev. Lett.*, vol. 83, p. 5270, 1999.

[91] A. J. Alcock and P. B. Corkum, "Ultra-fast switching of infrared radiation by laser-produced carriers in semiconductors," *Can. J. Phys.*, vol. 57, p. 1280, 1979.

[92] C. V. Filip *et al.*, "Optical kerr switching technique for the production of a picosecond, multiwavelength CO_2 laser pulse," *J. App. Opt.*, vol. 41, p. 3743, 2002.

[93] J. M. Liu, *Photonic Devices.* Cambridge: Cambridge University Press, 2005.

[94] R. A. Ganeev, A. I. Ryasnyanski, and H. Kuroda, "Nonlinear optical characteristics of carbon disulfide," *Opt. and Spec.*, vol. 100, p. 108, 2006.

[95] B. F. Kuntsevich *et al.*, "Field mechanism for simultaneous oscillation on several transitions in tea CO_2 lasers," *IEEE J. Quantum Electron.*, vol. QE-23, p. 481, 1993.

[96] S. Tochitsky *et al.*, "Present status and future prospects of high-power CO_2 laser research," in *Proceedings of the International Conference on Lasers*, 2000, p. 417.

[97] L. M. Frantz and J. S. Nodvik, "Theory of pulse propagation in a laser amplifier," *J. App. Phy.*, vol. 34, p. 2346, 1963.

[98] S. Semushin and V. Malka, "High density gas jet nozzle design for laser target production," *Rev. Sci. Instrum.*, vol. 72, p. 2961, 2001.

[99] W. L. McLaughlin, M. Al-Sheikhly, D. F. Lewis, A. Kovacs, and L. Wojnarovits, "Radiochromic solid-state polymerization reaction," in *Irradiation of Polymers*, R. L. Clough and S. W. Shalaby, Eds. Washington, DC: American Chemical Society, 1996, ch. 11.

[100] D. S. Hey, "Use of GafChromic film to diagnose laser generated proton beams," *Rev. Sci. Instrum.*, vol. 79, p. 053501, 2008.

[101] F. Nürnberg, "Radiochromic film imaging spectroscopy of laser-accelerated proton beams," *Rev. Sci. Instrum.*, vol. 80, p. 033301, 2009.

[102] G. G. Cartwright, E. K. Shirk, and P. B. Price, "A nuclear-track-recording polymer of unique sensitivity and resolution." *Nucl. Instrum. Meth.*, vol. 153, p. 457, 1978.

[103] K. Hara, M. Koh, T. Matsukawa, T. Tanii, and I. Ohdomari, "Single-ion detection using nuclear track detector CR-39 plastic," *Rev. Sci. Instrum.*, vol. 70, p. 4536, 1999.

[104] S. Kar *et al.*, "Analysis of latent tracks for MeV protons in CR-39," *J. App. Phys.*, vol. 101, p. 044510, 2007.

[105] W. R. Leo, *Techniques for Nuclear and Particle Physics Experiments*, 2nd ed. Berlin, Germany: Springer-Verlag, 1994.

[106] Y. V. Rao, A. Davis, and M. P. Hagan, "CR-39 plastic track detector experiment for measurement of charge composition of primary cosmic rays," in *Origin of Cosmic Rays*, G. Setti, G. Spada, and A. W. Wolfendale, Eds. International Astronomical Union, 1981.

[107] P. Hariharan, *Optical Interferometry.* San Diego, California, USA: Academic Press Inc., 1985.

[108] J. Sheffield, D. Froula, S. H. Glenzer, and N. C. L. Jr., *Plasma Scattering of Electromagnetic Radiation, Second Edition: Theory and Measurement Techniques.* London, England: Academic Press, 2011.

[109] G. S. Settles, *Schlieren and Shadowgraph Techniques : Visualizing Phenomena in Transparent Media.* Berlin, Germany: Springer, 2001.

[110] M. Takeda, H. Ina, and S. Kobayashi, "Fourier-transform method of fringe-pattern analysis for computer-based topography and interferometry," *J. Opt. Soc. Am.*, vol. 72, p. 156, 1982.

[111] D. Haberberger, "Optical ray tracing program written in Matlab based upon ABCD matrix propagation of a Gaussian laser beam." 2008.

[112] P. B. Corkum and D. Keith, "Controlled switching of 10-micrometer radiation using semiconducotr etalons," *J. Opt. Soc. Am. B*, vol. 2, p. 1873, 1985.

[113] A. Pak, "Phase retrival and Abel inversion programs written in Matlab," 2009.

[114] C. Gong, "Image recording and intelligent pit counting program written in matlab," 2009.

[115] M. Tatarakis *et al.*, "Propagation instabilities of high-intensity laser-produced electron beams," *Phys. Rev. Lett.*, vol. 90, p. 175001, 2003.

[116] M. S. Wei *et al.*, "Observations of the filamentation of high-intensity laser-produced electron beams," *Phys. Rev. E*, vol. 70, p. 056412, 2004.

[117] Y. Sentoku *et al.*, "Three-dimensional particle-in-cell simulations of energetic electron generation and transport with relativistic laser pulses in overdense plasmas," *Phys. Rev. E*, vol. 65, p. 046408, 2002.

[118] D. J. Bradley, B. Liddy, and W. E. Sleat, "Direct linear measurement of ultrashort light pulses with a picosecond streak camera," *Opt. Comm.*, vol. 2, p. 391, 1971.

[119] K. Bockasten, "Transformation of observed radiances into radial distribution of the emission of a plasma," *J. Opt. Soc. Am.*, vol. 51, p. 943, 1961.

[120] M. Kalal and K. A. Nugent, "Abel inversion using fast fourier transforms," *App. Opt.*, vol. 27, p. 1956, 1988.

[121] A. F. P. Houwing *et al.*, "Abel inversion of axially-symmetric shock wave flows," *Shock Waves*, vol. 14, p. 21, 2005.

[122] D. Haberberger and A. Pak, "Matlab program for simulating interferograms from a 3d plasma profile," 2009.